THEORETICAL DESCRIPTION OF CHARGE-TRANSPORT AND CHARGE-GENERATION PARAMETERS IN SINGLE-COMPONENT AND BIMOLECULAR CHARGE-TRANSFER ORGANIC SEMICONDUCTORS

A Dissertation
Presented to
The Academic Faculty

by

Alexandr Fonari

In Partial Fulfillment
of the Requirements for the Degree
Doctor of Philosophy in the
School of Chemistry and Biochemistry

Georgia Institute of Technology
December 2015

THEORETICAL DESCRIPTION OF CHARGE-TRANSPORT AND CHARGE-GENERATION PARAMETERS IN SINGLE-COMPONENT AND BIMOLECULAR CHARGE-TRANSFER ORGANIC SEMICONDUCTORS

Approved by:

Dr. Jean-Luc Brédas, Co-Advisor
School of Chemistry and Biochemistry
Georgia Institute of Technology

Dr. Veaceslav Coropceanu, Co-Advisor
School of Chemistry and Biochemistry
Georgia Institute of Technology

Dr. C. David Sherrill
School of Chemistry and Biochemistry
Georgia Institute of Technology

Dr. Kenneth R. Brown
School of Chemistry and Biochemistry
Georgia Institute of Technology

Dr. Joseph W. Perry
School of Chemistry and Biochemistry
Georgia Institute of Technology

Dr. Zhigang Jiang
School of Physics
Georgia Institute of Technology

Date Approved: July 29, 2015

ACKNOWLEDGEMENTS

TABLE OF CONTENTS

LIST OF TABLES

LIST OF FIGURES

Page

SUMMARY

The rapid growth of organic materials for electronic applications, such as field-effect transistors and solar cells, is driving the development of theoretical and computational models to describe and predict their intrinsic performance. Since, unlike conventional semiconductors, organic materials are weakly bound by inter-molecular forces, charge-transport models are built to take into account both static electronic properties and dynamic properties, latter arising from the interactions between lattice vibrations and charge carriers.

In this dissertation, we employ a number of computational methods, including *Ab Initio*, Density Functional Theory, and Molecular Dynamics simulations to investigate key microscopic parameters that govern charge-transport and charge-generation in single-component and bimolecular charge-transfer organic semiconductors.

First, static (electronic couplings, bandwidths, effective masses) and dynamic (electron-phonon couplings) transport properties of single-component organic semiconductors are discussed. In particular, we evaluate microscopic charge-transport parameters in a series of nonlinear acenes with extended π-conjugated cores. Our studies suggest that high charge-carrier mobilities are expected in these materials, since large electronic couplings are obtained and the formation of self-localized polarons due to local and nonlocal electron-phonon couplings is unlikely. Next, we evaluate charge detrapping due to interaction with intra-molecular crystal vibrations in order to explain changes in

experimentally measured electric conductivity generated by pulse excitations in the IR region of a photoresistor based on pentacene/C60 thin film. Here, we directly relate the nonlocal electron-phonon coupling constants with variations in photoconductivity.

In terms of charge photogeneration from an excited manifold, we evaluate the modulation of the state couplings between singlet and triplet excited states due to crystal vibrations, in order to understand the effect of lattice vibrations on singlet fission in tetracene crystal. We find that the state coupling between localized singlet and correlated triplet states is much more strongly affected by the dynamical disorder due to lattice vibrations than the coupling between the charge-transfer singlet and triplet states.

Next, the impact of Hartree-Fock exchange in the description of transport properties in crystalline organic semiconductors is discussed. Depending on the nature of the electronic coupling, transfer integrals and bandwidths can show a significant increase as a function of the amount of the Hartree-Fock exchange included in the functional. Similar trend is observed for the lattice relaxation energy. It is also shown that the ratio between electronic coupling and lattice relaxation energy is practically independent of the amount of the Hartree-Fock exchange, making this quantity a good candidate for incorporation into tight-binding transport models. We also demonstrate that it is possible to find an amount of the Hartree-Fock exchange that recovers (quasi-particle) band structure obtained from a highly accurate G_0W_0 approach. Finally, a microscopic understanding of a phase transition in charge-carrier mobility from temperature independent to thermally activated in stilbene-tetrafluoro-tetracyanoquinodimethane crystal is provided.

CHAPTER 1

INTRODUCTION

1.1 Overview

Organic materials based on π-conjugated backbones have been incorporated as the active layer in various electronic devices such as organic light-emitting diodes (OLEDs), organic photovoltaic devices (OPVs), such as solar cells, and organic field-effect transistors (OFETs) [1-3]. In addition, these weakly bounded molecular materials exhibit significant plasticity, making them ideal candidates for application in flexible and wearable electronics.
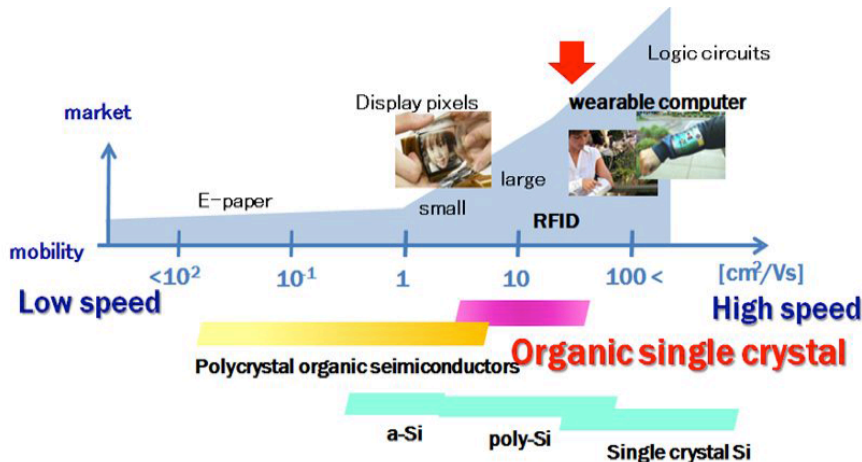
Figure 1.1 Examples of market application and comparison of transport properties of semiconductor materials. Taken from Ref. [4].

Irrespective of the nature of the application, high charge-carrier mobility, *i.e.* the ability of the material to transport easily charge carriers under an external electric field, is a desired characteristic for a semiconductor. For instance it was estimated that a mobility of

at least 5 cm^2/Vs is required for a proper functioning of an OLED [5]. To date, the highest hole mobility at room temperature, 20–40 cm^2/(Vs), was achieved for an OFET based on the rubrene single crystal [6].
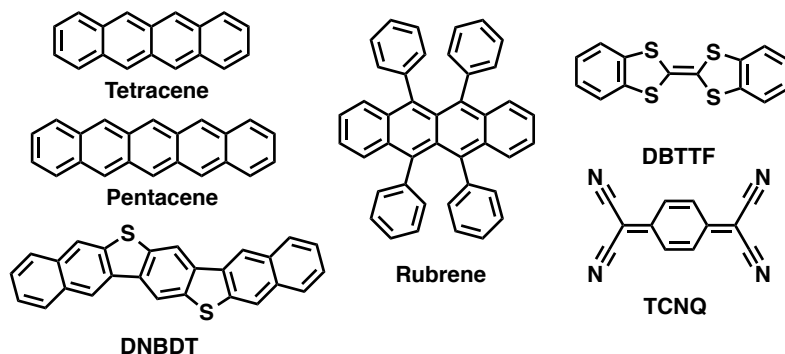
Figure 1.2 Examples of organic semiconductors (DNBDT = dinaphtho-benzo-dithiophene, DBTTF = dibenzotetra-thiafulvalene, TCNQ = 7,7,8,8-tetra-cyanoquinodimethane).

Although mobility is a macroscopic property, it is related to the molecular and crystal structure and microscopic charge-transport characteristics such as electronic couplings and electron-phonon couplings [7]. The large variety of molecular systems that could exhibit promising charge-transport properties emphasizes the importance of the design and engineering of the new materials based on a fundamental understanding of the desired characteristics. In particular, research efforts have been devoted towards unveiling the structure-property relationships between molecular structure, packing motif in crystal or thin film and extent of wavefunction overlap (electronic coupling) between weakly bounded molecules. As is discussed below, achieving a large electronic coupling is particularly important for charge transport in organic electronic devices. Many of the reported OFETs with high charge-carrier mobilities (>5 cm^2/Vs) are based on oligoacenes and their derivatives [8]. However, oligoacenes longer than five rings are not

stable due to their small ionization potentials [9,10] and possible development of a diradical character [11]. To overcome these issues it was proposed to incorporate thiophene units between the benzene moieties in order to extend the aromatic core. Recently a hole mobility of 10 cm^2/(Vs) was reported for a single-crystal FET based on dinaphtho-benzo-dithiophene (DNBDT) (Figure 1.2) [12]. Another approach is to employ two-dimensional acenes that represent various fragments of graphene. Molecules of this class have large, planar π-surfaces that could provide increased intermolecular overlap of orbitals related to large electronic couplings. In particular, the packing of these kinds of molecules is dictated by multiple interactions, which can effectively increase the dimensionality of the electronic structure, leading to enhanced transport properties [13]. A variety of two-dimensional polycylic aromatic hydrocarbons have been synthesized and characterized [14,15]. Thus it is of interest to evaluate the electronic structure and charge-transport parameters of these nonlinear acenes and also provide a theoretical guidance to design similar materials with extended conjugated core without penalty in stability.

While interest in organic molecular semiconductors has largely focused on systems based on a single molecule (like pentacene or rubrene), there is now an increasing push towards understanding the semiconducting properties of bimolecular charge-transfer (CT) organic crystals, where one component acts as an electron donor (D) and the other as an acceptor (A) [16-18]. Hasegawa and co-workers [19] used (BEDT-TTF)(F$_2$TCNQ) (BEDT = bis(ethylene-dithio)tetrathiafulvalene, F$_2$TCNQ = 2,5-difluorotetracyanoquinodimethane) as an active layer for the fabrication of ambipolar single crystal FETs. Recently, Zhang *et*

al. developed a mixed-stack annulene-TCNQ crystal; OFET devices based on this compound exhibit ambipolar behavior with hole mobility of 0.04 cm^2/(Vs) and electron mobility of 0.03 cm^2/(Vs) [20]. Large hole mobilities of 0.3 cm^2/(Vs) and 0.5 cm^2/(Vs) were also found in coronene-TCNQ [21] and (coronene tetracarboxylate)-(methyl viologen) [22] crystals, respectively. It was found that the performance of devices based on organic D-A systems can be enhanced when D-A materials are also used as source/drain electrodes. For instance, organic FETs based on DBTTF-TCNQ (DBTTF = dibenzotetra-thiafulvalene, TCNQ = 7,7,8,8-tetra-cyanoquinodimethane) mixed-stack single crystals as channel and TTF-TCNQ films as source and drain electrodes overperform similar devices with Au or Ag electrodes; mobilities as large as 1 cm^2/(Vs) have been found for both electrons and holes in DBTTF-TCNQ (Figure 1.1) [23,24]. Indeed, hole and electron bandwidths and electronic couplings comparable to, or larger than those found in rubrene were computed for several CT crystals (Figure 1.3) [17]. Thus, it is of interest to evaluate the charge-transport properties of promising CT crystals and also provide a theoretical understanding of the nature of the electronic coupling in these materials.
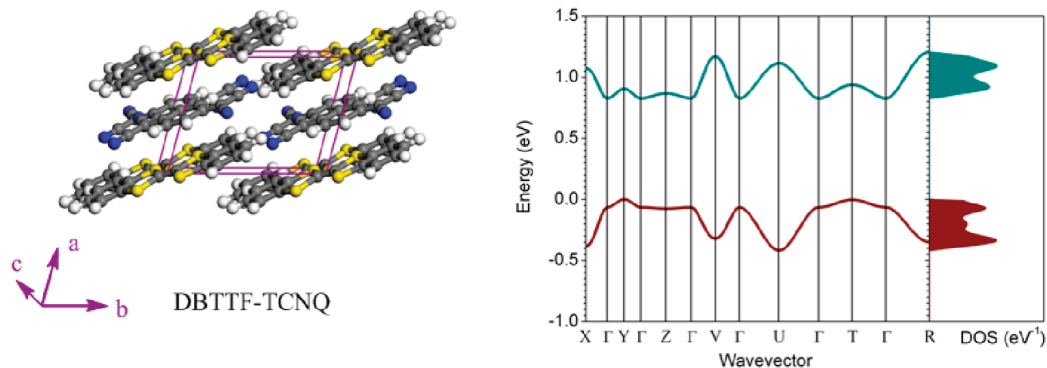
Figure 1.3 Left: Crystal packing of DBTTF-TCNQ crystal. Right: Electronic band structure and density of states of DBTTF-TCNQ crystal [17]. The points of high symmetry in the first Brillouin zone are labeled as follows: Γ = (0, 0, 0); X = (0.5, 0, 0); Y = (0, 0.5, 0); Z = (0, 0, 0.5); V = (0.5, 0.5, 0); U = (0.5, 0, 0.5); T = (0, 0.5, 0.5), and R = (0.5, 0.5, 0.5), all in crystallographic coordinates. Taken from Ref. [17].

It is well known that the 'soft' character of organic semiconductors strongly influences their electronic functionality [25,26]. Electronic coupling is determined by the overlap of the molecular orbitals and, therefore, is highly sensitive to minor changes in molecular and inter-molecular geometries. Hence, the electronic and transport properties of organic materials are largely determined by the interplay between the electronic and nuclear dynamics of the molecules, *i.e.*, electron-phonon (electron-vibrational) coupling. Vibrational motions have been also postulated to affect the interaction between different molecular electronic states by modulating inter- and intra-molecular couplings, by donating or accepting extra energy quanta [27,28], and by suppressing [29] or promoting [30] quantum interference phenomena. In particular, in the case of charge transport in organic systems, in the temperature-activated regime, lattice vibrations can facilitate de-trapping charges from *shallow* traps, *i.e.*, from localized states to extended band-states. While in the band-like regime, phonons can play a key role in de-trapping charges from the *deep* traps, pinned greatly below the Fermi level due to defects. In the band-like

5

regime, charge is delocalized over several molecules, mobility is defined as: $\mu = q\tau/m$ (see below). In the case of rubrene crystal, transition between activated and band-like regimes is observed at around 170 K (Figure 1.4) [7].
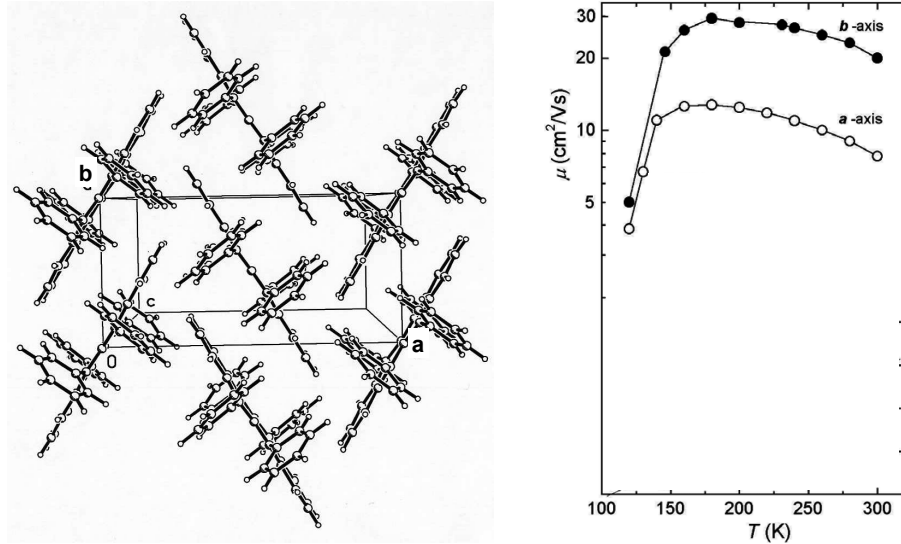
Figure 1.4 Left: Crystal packing of rubrene crystal. Right: Dependence of hole mobility on temperature in rubrene single-crystal FET. Taken from Ref. [6].

Thus, it is of interest to assert the impact that electron-phonon coupling has on macroscopic characteristics, such as electric current and charge-carrier mobility in single-component and bimolecular CT materials. We also note that lattice vibrations can be observed using spectroscopic techniques such as infra-red (IR) and Raman measurements. It also important to relate the nature of the lattice vibrations with the modulation of the key microscopic parameters that govern charge transport such as electronic coupling and site energy (see below).

Besides charge transport phenomena, charge generation from an excited manifold presents interest from both scientific and industrial standpoints. The performance of organic photovoltaic devices (OPVs) critically depends on the density of charge carriers (holes and electrons) that are created by means of photo-excitation. The device efficiency could potentially be improved by means of singlet fission (SF), whereby the dissociation of a singlet excited state could lead to the formation of two triplet excitations of lower energy on neighboring chromophores, and in the case of weak correlation, free pairs of electrons or holes could be created. SF offers the possibility of overcoming the theoretical Shockley-Queisser limit from 31% to greater than 45% [31]. High fission rates are required for OPV applications, since the fission process always competes with fluorescence and other fast transitions [32]. Several organic materials have been reported to exhibit high fission rates: tetracene (Tc), rubrene (Rb), 6,13-di(2-thienyl)tetracene (DTT), 6,13-di-tri-cyclohexylsilylethynyl-hexacene (Hc), pentacene (Pc), 6,13-bis(triisopropyl-silylethynyl) pentacene (TIPS-P), 6,13-diphenylpentacene (DPP), 6,13-di-biphenyl-4-yl-pentacene (DBP), 6,13-di(2-thienyl)pentacene (DTP) and 6,13-di-benzothiophenepentacene (DBTP) (Figure 1.5).
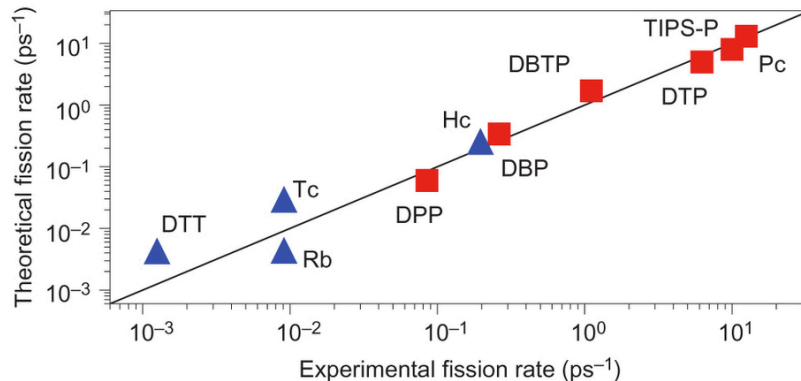
Figure 1.5 Theoretical and experimental fission rates for a series of organic crystals (see text for the notations). Taken from Ref. [33].

Materials that are capable of fission have already been incorporated in solar cells [34]. For instance, for pentacene/fullerene-based solar cells, an external quantum efficiency of exceeding 100% has been recently reported [33]. Similarly to charge transport, the singlet fission process is expected to be strongly affected by the lattice vibrations. Recent experimental [35] and theoretical [36,37] studies suggest that certain lattice vibrations can facilitate triplet formation, thus would be useful to understand how lattice vibrations can affect the SF microscopic characteristics.

Although a comprehensive understanding of the charge-transport [charge-generation] mechanism in the single-crystal organic molecular semiconductors still remains an open question [38], it is becoming clear that besides pure electronic [excitonic] interactions, electron-vibration [exciton-phonon] interactions play an important role in organic semiconductors. Thus, besides understanding the basic parameters that govern charge transport, it is also important to relate those to the spectroscopic observables (IR/Raman

spectra) in order to get a complete and correct picture of the underlying physics of charge transport and generation.

1.2 Microscopic parameters that govern charge transport in molecular organic semiconductors

In the pure electronic picture, large transfer integrals (electronic couplings) between π-conjugated molecules are necessary for high charge-carrier mobilities [7]. There are two main theoretical approaches to derive the electronic couplings. The first is based on a molecular (localized) representation whereby the electronic coupling (or transfer integral, t) between any two molecules can be evaluated from the quantum-mechanical solutions obtained on dimers (or complexes) consisting of these two molecules (φ_A, φ_B) within Hartree-Fock (HF) or Density Functional Theory (DFT) approximations (see Chapter 2). In the molecular-localized basis set, site energies and transfer integrals are obtained as diagonal and off-diagonal elements of the Fock matrix built using fragment orbital approach [39]:

$$\epsilon_{ii} = \langle \varphi_i | F | \varphi_i \rangle \qquad\qquad t_{ij} = \langle \varphi_i | F | \varphi_j \rangle, \qquad\qquad (1.2)$$

where the adiabatic states (φ_i and φ_j) are the monomer highest occupied molecular orbital (HOMO) or lowest occupied molecular orbital (LUMO) related to hole or electron transport, respectively. Alternatively, a momentum (delocalized) representation can be used, with the electronic couplings obtained from band-structure calculations performed on the corresponding crystal using periodic boundary conditions (see Chapter 2). Similar to the role played by transfer integrals in the molecular picture, the widths of the valence [conduction] bands and the hole [electron] effective masses represent key charge-

transport parameters for periodic systems. In particular, within the Drude model [40], the mobility (μ) is defined as: $\mu = q\tau/m$, where τ is time between scattering events and m represents the effective mass of the charge carrier. Valence [conduction] bandwidths are readily available from density of states or band-structure calculations. The inverse effective mass tensor in a three-dimensional crystal ($1/m_{ij}$) is defined as [40]:

$$\frac{1}{m_{ij}} = \frac{1}{\hbar^2} \frac{\partial^2 E}{\partial k_i \partial k_j},$$

(1.3)

where subscripts i and j denote the Cartesian coordinates in reciprocal space, E is the band energy, $\hbar$ is the Planck constant, and k is the electron wavevector. Subsequent diagonalization of $1/m_{ij}$ provides the principal components and their orientations. The inverse effective mass tensor can be calculated by means of the centered difference method. Hole [electron] effective masses are defined at the top [bottom] of the valence [conduction] band. Although the actual charge-transport mechanism in organic molecular semiconductors remains a matter of debate, recent angle-resolved ultraviolet photoelectron spectroscopy measurements performed on rubrene and pentacene crystals point to a clear energy dispersion of the highest occupied electronic levels, indicating that the concept of electronic bands is valid for these systems [41-43]. We note that, when appropriately chosen, a simple tight-binding Hamiltonian can be used to relate the results obtained in the molecular picture to those in the momentum representation [7]. In particular, in order to relate the localized and delocalized representations a tight-binding Hamiltonian is defined as:

$$H = \sum_m \varepsilon_m a_m^+ a_m + \sum_{m \neq n} t_{mn} a_m^+ a_n,$$

(1.4)

where a_m^+ and a_m denote the creation and annihilation operators, respectively, for a hole [electron] at site m; ε_m is the site energy, and t_{mn} is the electronic coupling (transfer integral) between sites m and n. Once the values of site energies and electronic couplings between neighboring molecules are known, it is possible to recover the electronic band-structure of the crystal. For instance, in the pentacene crystal, four hole couplings can accurately describe the valence band (Figure 1.6). We also note that within the one-dimensional tight-binding approximation, the effective mass (m) and bandwidth (W) can be related to electronic coupling (t) as:

$$m = \frac{\hbar^2}{2td^2} \qquad\qquad W = 4t, \qquad\qquad (1.5)$$

where d is the intermolecular distance.
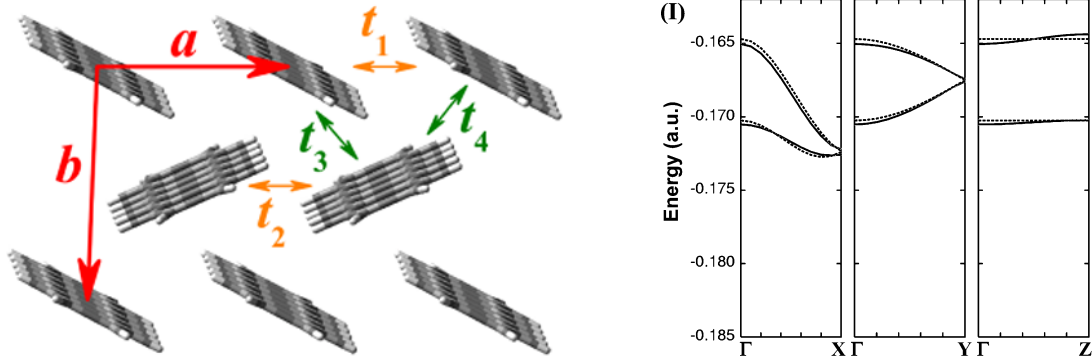
Figure 1.6 Left: Crystal structure and molecular pairs leading to the largest transfer integrals in the pentacene crystal. Right: Valence bands of pentacene crystal obtained within Density Functional Theory (solid lines) and tight-binding DFT approximation (dashed lines). Taken from Refs. [44,45].

In addition to the purely electronic interactions, as already underlined earlier, the charge-transport properties in molecular solids also depend on the interactions between charge carriers and lattice vibrations (hole-phonon or electron-phonon coupling). These

couplings can be divided into two types, *i.e.* local (Holstein-type) and nonlocal (Peierls-type) [46]. The Holstein electron-phonon interaction originates from the modulation of the site energies by the vibrations. The Peierls-type electron-phonon couplings are associated with the dependence of the transfer integrals on the distances between adjacent molecules and their relative orientations [46]. Both local and nonlocal coupling constants can be computed by expanding the electronic couplings into Taylor series of the phonon eigenvectors:

$$\varepsilon_m = \varepsilon_m^{(0)} + \sum_j v_{jm} Q_j + \cdots; \quad v_{jm} = \frac{\partial \varepsilon_m}{\partial Q_j} \tag{1.6a}$$

$$t_{mn} = t_{mn}^{(0)} + \sum_j v_{jmn} Q_j + \cdots; \quad v_{jmn} = \frac{\partial t_{mn}}{\partial Q_j} \tag{1.6b}$$

Here, $\varepsilon_m^{(0)}$ and $t_{mn}^{(0)}$ represent the site energy and electronic coupling at the crystal equilibrium geometry; Q_j is the normal-mode coordinate of mode j, with frequency ω_j; v_j is the linear nonlocal electron-phonon coupling constant. The local electron-phonon coupling is related to the polaron binding energy: $E_{pol,m} = \sum_j v_{jm}^2 / 2\hbar\omega_j$. In the context of electron-transfer theory, $E_{pol,m}$ is roughly equal to half the reorganization energy (λ) [7]. Since the intermolecular polarization contributions to λ is expected to be small [47], only the intra-molecular contributions to λ are usually taken into account. Intra-molecular contributions to the reorganization energy can be calculated using adiabatic energy surfaces and normal-mode approaches [48].

Similarly to the local electron-phonon coupling, nonlocal electron-phonon coupling is related to the lattice relaxation energy: $L_{mn} = \sum_j v_{jmn}^2 / 2\hbar\omega_j$. In practice, coupling constants can be calculated by distorting the crystal along all normal-mode coordinates

with positive and negative steps and then computing numerically the related derivatives of the transfer integrals for each vibrational mode.

Once the nonlocal constants (v_{jmn}) are known, it is possible to evaluate the temperature dependence of the variance (σ^2) in electronic couplings [49]:

$$\sigma^2 = \langle ((\langle t_{mn} \rangle - t_{mn})^2 \rangle = \langle t_{mn}^2 \rangle - \langle t_{mn} \rangle^2, \qquad (1.7)$$

where $\langle t_{mn} \rangle = t_{mn}^{(0)}$. It follows that:

$$\langle t_{mn}^2 \rangle = \left(t_{mn}^{(0)} \right)^2 + \left(\sum_j v_{jmn} Q_j \right)^2. \qquad (1.8)$$

By combining Equations 1.7 and 1.8 it is possible to show that:

$$\sigma^2 = \left(\sum_j v_{jmn} Q_j \right)^2. \qquad (1.9)$$

At the equilibrium temperature, T, the average of both kinetic and potential energies does not depend on frequency of atomic motions, and is equal to $k_b T / 2$. Thus, the classical mean-square fluctuation of normal modes is:

$$\left\langle Q_j^2 \right\rangle_{CM} = \frac{k_B T}{\hbar \omega_j}. \qquad (1.10)$$

Using Equations 1.8 and 1.9, it is possible to correlate the variance (σ^2) of the transfer integral in the classical picture with lattice relaxation energy (L):

$$\sigma^2 = 2 L k_b T. \qquad (1.11)$$

In practice, $\langle ... \rangle$ represents the average over geometrical configurations resulting from thermal motion. The variance (σ^2) is computed by calculating the electronic couplings using dimer geometries extracted from snapshots of a molecular dynamics run at a finite temperature.

1.3 Thesis objectives and outline

Advances in the field of organic electronics are integrally connected with the discovery of potential candidates with exceptional charge-transport characteristics either by synthesizing novel material or by revisiting already existing materials. Besides molecular structure, interactions in the solid state are of particular importance in van Der Waals-bound molecular materials. This thesis has several aims. The first is to describe the electronic and charge-transport properties of several promising single-component and bimolecular CT organic semiconductors and provide computational guidance for the design of novel materials with remarkable stability and charge-transport characteristics. A second aim is to realize the nature and impact of the lattice vibrations on electronic device characteristics by combining theoretical spectroscopy with microscopic theory of charge transport and charge generation.

In Chapter 2, we review the computational techniques employed in this work. First, we introduce the underlying formalism of quantum mechanics, and describe Hartree-Fock, Density Functional Theory (DFT), and GW approaches. Since we use different types of density functionals throughout this work, we briefly describe each density functional type employed. Second, we describe methods that allow computation of the lattice vibrations and spectroscopic observables in periodic systems within DFT. Finally, we briefly describe basic concepts related to the molecular dynamics (MD) simulations since this technique is only employed in Chapter 4 of this work.

In Chapter 3, several nonlinear acenes based on fused oligoacenes are investigated in terms of optical (absorption spectra) and electronic charge-transport characteristics (electronic couplings, bandwidths and effective masses). We then evaluate polaron binding energies and lattice relation energies in order to estimate the local and nonlocal electron-phonon coupling strengths, respectively. We also propose a simple interpretation of the photo-physical properties of these systems within the framework of Clar's aromatic sextet model. Finally, we examine the influence of the packing polymorphism on the electronic structure and charge-transport properties in nonlinear acenes.

In Chapter 4, we evaluate the strength of interactions between lattice vibrations and charge carriers in these nonlinear acenes. In particular, we evaluate the local and nonlocal electron-phonon couplings. We conclude that the formation of polarons due to local and nonlocal electron-phonon coupling is unlikely in these systems, suggesting band-like transport regime at room temperature. In the second part of this Chapter, we provide a computational insight into a novel experiment that monitors the variation of electrical current due to the IR excitation of the lattice vibrations. We accomplish this by evaluating the nonlocal electron-phonon couplings for the IR-excited modes and the phonon-assisted charge hopping rates using Miller-Abrahams theory.

In Chapter 5, we present a study to identify the low-frequency intermolecular vibrational modes that are essential to the singlet fission process in the tetracene crystal. Good agreement obtained between the simulated and experimental IR and Raman spectra allows us to identify and understand the effect that different intermolecular modes have

on the SF characteristics. We assess how intermolecular modes with different displacement patterns affect state couplings within direct two-electron and charge-transfer SF pathways.

In Chapter 6, we first evaluate the electronic structure and charge-transport characteristics of several bimolecular CT systems. Our calculations show that for several systems, values obtained for both hole and electron effective masses are smaller than the effective masses in pentacene and rubrene crystals, suggesting that these systems could be good candidates for ambipolar FETs. In the second part of the Chapter, we confirm the superexchange mechanism of the electronic coupling in mixed-stack CT system DBTTF-TCNQ. We show that in the pentacene crystal, the band gap decreases and the effective masses increase linearly with an increase in the amount of exact Hartree-Fock exchange included in the functional. In contrast, in the charge-transfer crystals, while the band gap increases linearly, the effective masses vary only slightly with an increase in percentage of Hartree-Fock exchange. Finally we show that, for a particular percentage of Hartree-Fock exchange included in the functional, band gaps and valence and conduction bandwidths obtained using the G_0W_0 method, are recovered.

In Chapter 7, we first simulate the Raman spectrum of a bimolecular CT crystal: anthracene-PMDA (PMDA = pyromellitic dianhydride). Good agreement obtained between simulated and experimental Raman spectra allows us to assign experimentally measured peaks, in the low and medium frequency region, to the calculated lattice vibrations. We also evaluate how frequencies and Raman intensities change with

different amounts of Hartree-Fock exchange included in the functional. Then, we compute nonlocal electron-phonon couplings and discuss how different lattice vibrations affect the modulation of transfer integrals. In the second part of this Chapter, we provide a computational insight into charge-carrier mobility transition observed in the CT crystal stilbene-F_4TCNQ. We calculate the lattice vibrations in this crystal and evaluate modulation of the electronic couplings with respect to several lattice vibrations that can be relevant to the transition.

In Chapter 8, we provide overall conclusions, further considerations and research directions for the future work.

1.4 References

[1]   Cao, W.; Xue, J. *Energy & Environmental Science* **2014**, *7*, 2123.

[2]   Dimitrakopoulos, C. D.; Mascaro, D. J. *IBM Journal of Research and Development* **2001**, *45*, 11.

[3]   Kelley, T. W.; Baude, P. F.; Gerlach, C.; Ender, D. E.; Muyres, D.; Haase, M. A.; Vogel, D. E.; Theiss, S. D. *Chemistry of Materials* **2004**, *16*, 4413.

[4]   Takeya, J. *SPIE Proceedings* **2014**, *9185*, 91850I.

[5]   Sirringhaus, H. *Advanced Materials* **2014**, *26*, 1319.

[6]   Podzorov, V.; Menard, E.; Borissov, A.; Kiryukhin, V.; Rogers, J. A.; Gershenson, M. E. *Physical Review Letters* **2004**, *93*, 086602.

[7]   Coropceanu, V.; Cornil, J.; da Silva Filho, D. A.; Olivier, Y.; Silbey, R.; Bredas, J. L. *Chemical Reviews* **2007**, *107*, 926.

[8]   Anthony, J. E. *Angewandte Chemie International Edition* **2008**, *47*, 452.

[9]   Würthner, F.; Schmidt, R. *ChemPhysChem* **2006**, *7*, 793.

[10]   Purushothaman, B.; Bruzek, M.; Parkin, S. R.; Miller, A.-F.; Anthony, J. E. *Angewandte Chemie International Edition* **2011**, *50*, 7013.

[11]   Bendikov, M.; Duong, H. M.; Starkey, K.; Houk, K. N.; Carter, E. A.; Wudl, F. *Journal of the American Chemical Society* **2004**, *126*, 7416.

[12]   Junshi, S.; Takafumi, U.; Toshihiro, O.; Chikahiko, M.; Masakazu, Y.; Jun, T. *Applied Physics Express* **2013**, *6*, 076503.

[13]   Wu, J.; Pisula, W.; Müllen, K. *Chemical Reviews* **2007**, *107*, 718.

[14]   Watson, M. D.; Fechtenkötter, A.; Müllen, K. *Chemical Reviews* **2001**, *101*, 1267.

[15]   Berresheim, A. J.; Müller, M.; Müllen, K. *Chemical Reviews* **1999**, *99*, 1747.

[16]   Tatsuo, H.; Jun, T. *Science and Technology of Advanced Materials* **2009**, *10*, 024314.

[17]   Zhu, L.; Yi, Y.; Li, Y.; Kim, E.-G.; Coropceanu, V.; Bredas, J. L. *Journal of the American Chemical Society* **2012**, *134*, 2340.

[18]   Goetz, K. P.; Vermeulen, D.; Payne, M. E.; Kloc, C.; McNeil, L. E.; Jurchescu, O. D. *Journal of Materials Chemistry C* **2014**, *2*, 3065.

[19]   Hasegawa, T.; Mattenberger, K.; Takeya, J.; Batlogg, B. *Physical Review B* **2004**, *69*, 245115.

[20]   Zhang, J.; Geng, H.; Virk, T. S.; Zhao, Y.; Tan, J.; Di, C.-a.; Xu, W.; Singh, K.; Hu, W.; Shuai, Z.; Liu, Y.; Zhu, D. *Advanced Materials* **2012**, *24*, 2603.

[21]   Chi, X.; Besnard, C.; Thorsmølle, V. K.; Butko, V. Y.; Taylor, A. J.; Siegrist, T.; Ramirez, A. P. *Chemistry of Materials* **2004**, *16*, 5751.

[22]   Sagade, A. A.; Venkata Rao, K.; George, S. J.; Datta, A.; Kulkarni, G. U. *Chemical Communications* **2013**, *49*, 5847.

[23]   Sakai, M.; Sakuma, H.; Ito, Y.; Saito, A.; Nakamura, M.; Kudo, K. *Physical Review B: Condensed Matter* **2007**, *76*, 045111.

[24]   Takahashi, Y.; Hasegawa, T.; Abe, Y.; Tokura, Y.; Saito, G. *Applied Physics Letters* **2006**, *88*, 073504.

[25]   Bredas, J. L.; Street, G. B. *Accounts of Chemical Research* **1985**, *18*, 309.

[26]   Galperin, M.; Ratner, M. A.; Nitzan, A.; Troisi, A. *Science* **2008**, *319*, 1056.

[27]   Gane, S.; Georganakis, D.; Maniati, K.; Vamvakias, M.; Ragoussis, N.; Skoulakis, E. M. C.; Turin, L. *PLoS ONE* **2013**, *8*, e55780.

[28]   Falke, S. M.; Rozzi, C. A.; Brida, D.; Maiuri, M.; Amato, M.; Sommer, E.; De Sio, A.; Rubio, A.; Cerullo, G.; Molinari, E.; Lienau, C. *Science* **2014**, *344*, 1001.

[29]   Ballmann, S.; Härtle, R.; Coto, P. B.; Elbing, M.; Mayor, M.; Bryce, M. R.; Thoss, M.; Weber, H. B. *Physical Review Letters* **2012**, *109*, 056801.

[30]   Chin, A. W.; Prior, J.; Rosenbach, R.; Caycedo-Soler, F.; Huelga, S. F.; Plenio, M. B. *Nature Physics* **2013**, *9*, 113.

[31]   Hanna, M. C.; Nozik, A. J. *Journal of Applied Physics* **2006**, *100*.

[32]   Smith, M. B.; Michl, J. *Chemical Reviews* **2010**, *110*, 6891.

[33]   Congreve, D. N.; Lee, J.; Thompson, N. J.; Hontz, E.; Yost, S. R.; Reusswig, P. D.; Bahlke, M. E.; Reineke, S.; Van Voorhis, T.; Baldo, M. A. *Science* **2013**, *340*, 334.

[34]   Smith, M. B.; Michl, J. *Annual Review of Physical Chemistry* **2013**, *64*, 361.

[35]   Grumstrup, E. M.; Johnson, J. C.; Damrauer, N. H. *Physical Review Letters* **2010**, *105*, 257403.

[36]   Zimmerman, P. M.; Bell, F.; Casanova, D.; Head-Gordon, M. *Journal of the American Chemical Society* **2011**, *133*, 19944.

[37]   Zimmerman, P. M.; Zhang, Z.; Musgrave, C. B. *Nature Chemistry* **2010**, *2*, 648.

[38]   Vukmirović, N.; Bruder, C.; Stojanović, V. M. *Physical Review Letters* **2012**, *109*, 126407.

[39]   Valeev, E. F.; Coropceanu, V.; da Silva Filho, D. A.; Salman, S.; Bredas, J. L. *Journal of the American Chemical Society* **2006**, *128*, 9882.

[40]   Ashcroft, N.; Mermin, D. *Solid State Physics*; Thomson Learning, 1976.

[41]   Machida, S.-i.; Nakayama, Y.; Duhm, S.; Xin, Q.; Funakoshi, A.; Ogawa, N.; Kera, S.; Ueno, N.; Ishii, H. *Physical Review Letters* **2010**, *104*, 156401.

[42]   Hatch, R. C.; Huber, D. L.; Höchst, H. *Physical Review Letters* **2010**, *104*, 047601.

[43]   Koch, N.; Vollmer, A.; Salzmann, I.; Nickel, B.; Weiss, H.; Rabe, J. P. *Physical Review Letters* **2006**, *96*, 156803.

[44]   Li, Y.; Coropceanu, V.; Bredas, J. L. *The Journal of Physical Chemistry Letters* **2012**, *3*, 3325.

[45]   Troisi, A.; Orlandi, G. *The Journal of Physical Chemistry B* **2005**, *109*, 1849.

[46]   Bredas, J. L.; Calbert, J. P.; da Silva Filho, D. A.; Cornil, J. *Proceedings of the National Academy of Sciences* **2002**, *99*, 5804.

[47]   Norton, J. E.; Brédas, J.-L. *Journal of the American Chemical Society* **2008**, *130*, 12377.

[48]   Malagoli, M.; Coropceanu, V.; da Silva Filho, D. A.; Brédas, J. L. *The Journal of Chemical Physics* **2004**, *120*, 7490.

[49]   Coropceanu, V.; Sánchez-Carrera, R. S.; Paramonov, P.; Day, G. M.; Brédas, J.-L. *Journal of Physical Chemistry C* **2009**, *113*, 4679.

CHAPTER 2

COMPUTATIONAL METHODOLOGY

2.1 Introduction

Formally, all the knowledge and properties of interest about a quantum system can be obtained from a many-body quantum mechanical wavefunction (Ψ). In this Chapter, we first introduce the fundamental concepts and main approximations necessary to make such a many-body problem tractable. Next, we describe the formalism that allows the calculation of spectroscopic observables, such as IR and Raman spectra. Finally, we briefly discuss the main ideas behind molecular dynamics (MD) simulations. Although the field of quantum-chemical and solid-state computations is enormous, we focus here on the methods and approximations successfully employed in Chapters 3-7 of this dissertation.

2.2 Hartree-Fock approximation

The many-body wavefunction (Ψ) for a stationary system that contains N electrons at r_i positions and M nuclei at positions R_A can be obtained from the time-independent Schrodinger equation:

$$H\Psi = E\Psi \tag{2.1}$$

where the Hamiltonian (H) describing nucleus-nucleus, electron-electron, and nucleus-electron interactions is defined as (in atomic units, $\hbar = e = m_e = 1$):

$$H = -\frac{1}{2\mathcal{M}_A}\sum_A^M \nabla_A^2 - \frac{1}{2}\sum_i^N \nabla_i^2 - \sum_i^N \sum_A^M \frac{Z}{|r_i-R_A|} + \frac{1}{2}\sum_{i \neq j}\frac{1}{|r_i-r_j|} + \frac{1}{2}\sum_{A \neq B}\frac{Z_A * Z_B}{|R_A-R_A|} \tag{2.2}$$

The first two terms describe the system kinetic energy, obtained as the second-order derivative with respect to nuclei and electrons coordinates, respectively; the third term describes the attractive interactions between electrons and nuclei; the fourth term describes the electron-electron interactions; and the last term is the Coulomb repulsion between nuclei. For a system that contains more than two particles, the problem becomes intractable with current methods. Therefore, several approximations need to be introduced. Since the mass of the lightest nucleus is at least 1000 times heavier than the mass of an electron, it can be assumed that electrons move in a constant field created by nuclei at rest (Born-Oppenheimer approximation). Within this approximation, the kinetic energy term for nuclei becomes zero and the nuclear repulsion energy becomes a constant for a certain geometry. This approximation fails when the electron and nuclear motions are strongly coupled. Even taking into account the Born-Oppenheimer approximation, Equation (2.2) remains intractable for systems with two or more electrons due to the electron-electron interaction term. In a further simplification of the physical picture of a system, the electrons are treated in a mean-field (Hartree) approximation, and the many-electron wavefunction (Ψ) is written as a product of N one-electron wavefunctions (ψ_i):

$$\Psi(r_1, r_2, \dots, r_N) = \psi_1(r_1)\psi_2(r_2) \dots \psi_N(r_N) \tag{2.3}$$

The product on the right side of the equation is incompatible with Pauli exclusion principle. In order to comply with Pauli exclusion principle, which requires Ψ to be anti-symmetric in the case of interchange of two electrons, Fock proposed to replace Equation (2.3) with a Slater determinant of one-electron wavefunctions:

$$\Psi(r_1, r_2, \dots, r_N) = \frac{1}{\sqrt{N!}} \begin{pmatrix} \psi_1(r_1) & \cdots & \psi_N(r_1) \\ \vdots & \ddots & \vdots \\ \psi_1(r_N) & \cdots & \psi_N(r_N) \end{pmatrix}. \tag{2.4}$$

Using the Hartree-Fock (HF) approximation, the multi-electron Equation (2.2) can be replaced by a system of one-electron Schrodinger equations:

$$-\frac{\hbar^2}{2m}\nabla_i^2\,\psi_i(\mathrm{r}) + V_{nuc}(r)\,\psi_i(\mathrm{r}) + V_{elec}(r)\,\psi_i(\mathrm{r}) -$$

$$\sum_j \int \frac{dr}{|r-r'|}\psi_j^*(\mathrm{r}')\psi_i(\mathrm{r}')\psi_j(\mathrm{r})\psi_i^*(\mathrm{r}) = \varepsilon_i\psi_i(\mathrm{r}). \tag{2.5}$$

Here, kinetic energy term is applied only on one-electron wavefunctions. $V_{nuc}(r)$ is the attractive potential due to nuclei and $V_{elec}(r)$ is the potential due to charge density (ρ) of all electrons in the system (even the electron itself). The last integral operator describes electron exchange explicitly. Thus, Equation (2.5) represents non-linear integral eigenvalue problem with orthogonal eigenfunctions (one-electron wavefunctions, ψ_i) and eigenvalues (ε_i) that can be solved in a self-consistent way [1]. Although the HF approximation includes electron exchange interactions explicitly, it does not account for the instantaneous correlation of the electron motions (electron correlation), which proves to be important for a correct description, see below.

2.3 Density functional theory

The main concept behind Density Functional Theory (DFT) is to employ the ground-state electron density (ρ) to completely describe the system, in contrast to the multi-electron wavefunction in the HF approach. In their seminal work, Hohenberg and Kohn [2] showed that the total ground-state energy of a system including electron exchange and correlation interactions in a static external potential (due to nuclei) is a unique functional of electron density ($E[\rho(r)]$):

$$E[\rho(r)] = \int V_{nuc}(r)\rho(r)dr + \frac{1}{2}\iint \frac{\rho(r)\rho(r\prime)}{|r-r\prime|}drdr' + T[\rho(r)] + E_{xc}[\rho(r)] \tag{2.6}$$

for a given external potential due to nuclei. The first two terms are similar to those present in the HF approximation: classical Coulomb attractive electron-nuclei and repulsive electron-electron interactions. $T[\rho(r)]$ is the kinetic energy functional for a system of non-interacting electrons with charge density $\rho(r)$. Later, it was shown that it is possible to replace the many-electron problem with a set of single-particle electron-density equations [3]. In this case, the kinetic energy functional can be expressed in terms of Kohn-Sham single particle orbitals (ψ_i):

$$T = \sum_{i=1}^{N} \frac{\hbar^2}{2m} \int \psi_i^*(r)(-\nabla^2)\psi_i(r) \, dr. \tag{2.7}$$

Unfortunately, the exact form of the remaining term in Equation (2.6), exchange-correlation functional ($E_{xc}[\rho(r)]$), is unknown. Several expressions for $E_{xc}[\rho(r)]$ have been proposed (see below). Once $E_{xc}[\rho(r)]$ is defined, it is possible to form a set of equations for non-interacting particles in the presence of an external potential:

$$\left\{-\frac{\hbar^2}{2m}\nabla^2 + V(r)\right\}\psi_i(r) = \varepsilon_i\psi_i(r) \tag{2.8}$$

In the local density approximation (LDA), the exchange-correlation functional at r depends only on the electron density at that point:

$$E_{xc}\big(\rho(r)\big) = \int \epsilon_{xc}\big(\rho(r)\big)\rho(r)dr \tag{2.9}$$

where $\epsilon_{xc}[\rho(r)]$ is the exchange-correlation energy per particle of an homogeneous electron gas. The Perdew and Zunger (PZ functional) [4] parameterization scheme of $\epsilon_{xc}[\rho(r)]$ is commonly employed. Currently, LDA is mostly used for testing and development purposes.

In the generalized gradient approximation (GGA), the exchange-correlation functional depends not only on the electron density but also on its gradient:

$$E_{xc}(\rho(r)) = \int \epsilon_{xc}(\rho(r), \nabla\rho(r)) \, \rho(r) dr \qquad (2.10)$$

The Perdew, Burke, Ernzerhof (PBE) [5,6] parameterization scheme of $\epsilon_{xc}[\rho(r)]$ is often employed. Here, we omit a discussion of meta-GGA functionals, which incorporate the Laplacian of the density in the $E_{xc}[\rho(r)]$ term and kindly refer the reader to recent reviews on this topic [7,8]. To date, GGA functionals are widely used in finite and periodic calculations of both inorganic and organic crystals. Due to the missing exact exchange in these GGA parameterizations, functionals based on GGA have several drawbacks, in particular an inability to correctly describe ground-state charge transfer and underestimation of the band gap. In some cases, for small band-gap materials, wrong occupation numbers are obtained for frontier (valence/conduction) bands, thus leading to the prediction of the metallic character of the system [9,10]. In order to alleviate these and other issues, electron exchange and correlation interactions should be taken into account explicitly. We employed the PBE functional as a starting point for *ab initio* GW calculations (see below) in Chapter 6.

In order to account for electron exchange interactions explicitly, a component of the exact exchange from HF approximation:

$$E_x^{HF} = -\frac{1}{2}\sum_{i,j} \iint \frac{dr}{|r-r'|} \psi_j^*(r')\psi_i(r')\psi_j(r)\psi_i^*(r) \qquad (2.11)$$

is introduced in the exchange-correlation functional ($E_{xc}[\rho(r)]$). Functionals that include exact exchange are referred to as standard hybrid functionals. These functionals usually include a linear combination of $E_x^{HF}[\rho(r)]$ and the remainder $E_{xc}[\rho(r)]$ coming from GGA parameterization. The most widely used hybrid functional is one parameterized by Becke, Lee, Yang and Parr (B3LYP) [11,12], which contains 20% of the exact HF

exchange. Another commonly used parameterization scheme is based on the addition of
the HF exchange to the PBE functional (PBE0). PBE0, proposed by Adamo and Barone,
is defined as:

$$E_{xc}^{PBE0} = \frac{1}{4}E_x^{HF} + \frac{3}{4}E_x^{PBE} + E_c^{PBE}, \qquad (2.12)$$

and incorporates 25% of HF exchange [13]. Using standard hybrid functionals, good
agreement between theory and experiment has been reported for band gaps, excitation
energies, IR and Raman spectra for a wide range of organic and inorganic systems.
Although incorporation of the exact exchange into the functional improves the
description of the band gaps and bandwidths of semiconductors, standard hybrid
functionals still fail to describe correctly systems with significant ground and excited-
state charge transfer.

It was recently realized that it is useful to split the Coulomb potential within the exchange
functional into short- and long-range terms (SR and LR) in order to obtain a better
description of charge-transfer systems [14]. Functionals with such Coulomb potential are
referred to as range-separated functionals. One of the commonly used schemes based on
the PBE functional was reported by Heyd, Scuseria and Ernzerhof (HSE) [15]:

$$E_{xc}^{HSE}(\mu) = \frac{1}{4}E_x^{HF,SR}(\mu) + \frac{3}{4}E_x^{PBE,SR}(\mu) + E_x^{PBE,LR}(\mu) + E_c^{PBE} \qquad (2.13)$$

Here the decomposition of the Coulomb operator in the short and long ranges (SR, LR) is
obtained using the error function:

$$\frac{1}{r} = \frac{erfc(\mu r)}{r} + \frac{\mathrm{erf}(\mu r)}{r} \qquad (2.14)$$

In the short range ($\mu \to 0$), $E_{xc}[\rho(r)]$ recovers the PBE0 form, with α giving the amount
of %HF exchange. In the long range ($\mu \to \infty$), $E_{xc}[\rho(r)]$ recovers the PBE form. Another

option is to have the GGA functional in the short range and exclusively HF exchange in the long range. One of the widely used schemes parameterized in this way was proposed by Chai and Head-Gordon (wB97) [16]:

$$E_{xc}^{wB97}(\mu) = E_x^{B97,SR}(\mu) + E_x^{HF,LR}(\mu) + E_c^{B97}. \qquad (2.15)$$

It was shown that range-separated functionals with full HF exchange in the long range, recovers the asymptotic behavior of the exchange/correlation potentials for finite systems [17]. This turned out to be important to correctly describe ground and excited states of organic molecules (finite systems) [18].

It is also possible to employ a functional with hybrid contributions both in short and long ranges. CAM-B3LYP based on B3LYP was the first functional that was parameterized in this way by Yanai and co-workers [19]:

$$E_{xc}(\mu) = \alpha E_x^{HF,SR}(\mu) + (1 - \alpha)E_x^{PBE,SR}(\mu) + \beta E_x^{HF,LR} + (1 - \beta)E_x^{PBE,LR}(\mu) + E_c^{PBE}. \quad (2.16)$$

Indeed, in order to correctly describe charge transfer in the ground and excited states of organic periodic systems, hybrid functionals in both short and long range should be employed. In particularly, inclusion of the HF exchange in the short range improves the local charge-transfer description, whereas HF exchange in the long range is important for the reliable prediction of the fundamental gaps (see Chapters 3, 6) [20]. Although both standard and range-separated hybrids show much better agreement with experimental data for both static and dynamic properties in inorganic and organic systems, it is of interest to understand how changing the amount of the HF exchange (α and β) and range separated parameter (μ) affects the performance of a functional.

2.3.1 Non-empirical tuning of density functionals

Janak's theorem states that the energy of the highest occupied molecular orbital (HOMO) or energy of the valence band should be mathematically equal to the vertical ionization potential (energy difference of neutral and cation states at neutral geometry) of the system [21]. Since the exact analytical form of the exchange-correlation functional is unknown, parameterizations employed in actual calculations can exhibit significant error. Thus, it was proposed to minimize this error ($J(\alpha, \mu)$) by changing the amount of the HF exchange included in the functional (α and β) or range-separation parameter (μ) [22]:

$$J(\alpha, \beta, \mu) = -\varepsilon_{HOMO}^{\alpha, \beta, \mu} - \left(E_{gs}(\alpha, \beta, \mu, N) - E_{cat}(\alpha, \beta, \mu, N-1) \right). \quad (2.17)$$

By applying this non-empirical "tuning" procedure, excellent agreement was obtained between calculations and experiment for ground and excited states for a variety of systems. For a comprehensive review of non-empirical tuning methods and achievements refer to Ref. [17]. In particular it was shown, that for a series of oligoacenes (from naphthalene to hexacene), the first excited-state energies obtained from the optimally-tuned CAM-B3LYP functional are in excellent agreement with experimental data (Figure 2.1) [23]. Another major issue that is solved by the introduction of the range-separated parameter in a hybrid functional is the description of the symmetric radical cation systems. Livshits and Baer showed that by applying a range-separated functional, it is possible to obtain essentially the exact potential energy surface in the dissociation limit for the H_2^+ radical-cation system [24]. In Chapter 3 we employ the optimally tuned wB97 functional in order to describe the excited states of a series of extended nonlinear acenes.
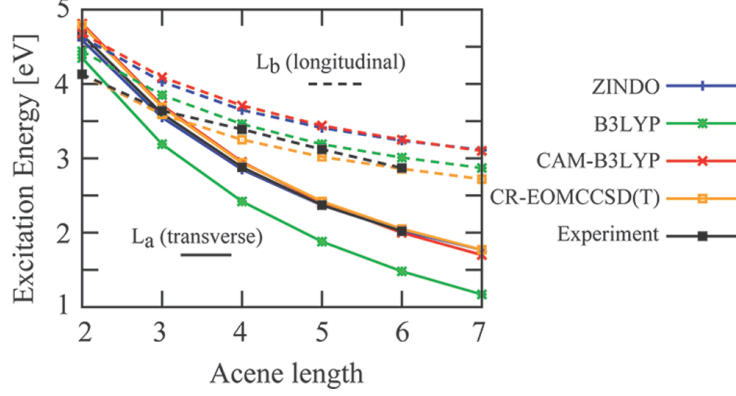
Figure 2.1 Transition energies of the first two excited states (S$_1$≡L$_a$, S$_2$≡L$_b$) for a series of oligoacenes obtained using different methods and compared to experimental values. "CR-EOMCCSD(T)" mutli-determinant wavefunction method is the benchmark. Taken from Ref. [23].

2.4 GW approximation

Another approach that is employed to accurately predict electronic energy levels, such as ionization energy and electronic affinity, in finite and periodic systems is GW. The idea of GW method is to map a many-body problem onto a single quasi-particle framework through perturbation [25]. In particular, Hedin proposed to describe the electron-hole pair (quasiparticle) interaction using one-electron Green function (*G*), and interaction between quasiparticles using screened Coulomb interaction energy *W* [26]. Hybersten and Louie introduced the generalized plasmon-pole (GPP) model [27] that allowed routine evaluations of the GW quasiparticle band structures and fundamental gaps in both inorganic and organic systems. Practically, starting from the expression for the DFT energy functional Equation (2.6), the exchange and correlation term is replaced with the nonlocal self-energy operator (Σ):

$$\left\{-\frac{\hbar^2}{2m}\nabla^2 + V_{nuc}(r) + V_{elec}(r) + \Sigma(\varepsilon_i^{QP})\right\}\psi_i^{QP}(r) = \varepsilon_i^{QP}\psi_i(r). \tag{2.18}$$

In the GW approximation, the self-energy operator is expressed using the one-electron Green's function (G) and screened Coulomb interaction (W): $\Sigma = iGW$. Since for a GW calculation, both energies and wavefunctions have to be updated self-consistently, which is computationally demanding task, one can perform one-shot calculation (G_0W_0). In this case only energies are updated once. By applying the G_0W_0 approach, an excellent description for the fundamental gaps of a series of inorganic semiconductors has been reported (Figure 2.2) [28]. Technically, the quasiparticle energies are calculated starting from a converged ground-state wavefunction obtained at the DFT level (using LDA, GGA, or even a hybrid functional). We (see Chapters 6,7) and other groups [29,30] have now successfully applied the G_0W_0 approach to calculate the electronic properties of several organic semiconductors.
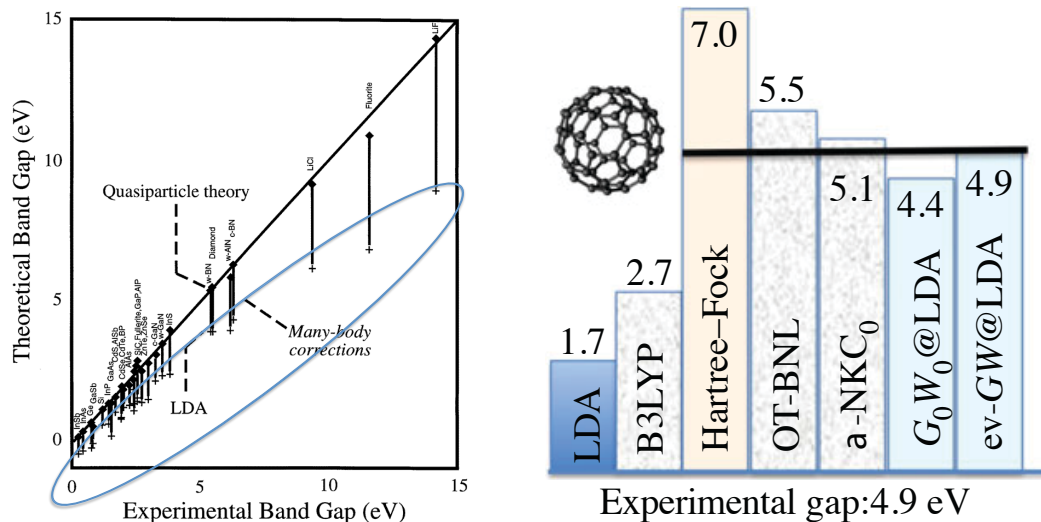
Figure 2.2 Left: Linear fit of the experimental and theoretical band gaps calculated using GW and LDA (stressed with blue oval) approaches. Plot courtesy of E. Shirley and S. G. Louie. Right: Fundamental gap of fullerene calculated using different approximations: LDA, B3LYP (standard hybrid functional), Hartree-Fock, OT-BNL (tuned range-separated functional), a-NKC$_0$ (non-Koopmans-corrected density functional [31], not discussed here), one-shot G_0W_0 starting from converged LDA wavefunctions (G_0W_0@LDA), self-consistent GW in eigenvalues starting from converged LDA wavefunctions (ev-GW@LDA). Taken from Ref. [32].

Recently, several groups were able to calculate quasiparticle energies self-consistently in eigenvalues (ev-GW) for several finite systems (Figure 2.2) [32,33]. As seen from the figure, tuned range-separated functionals cannot reproduce the fundamental gaps in strongly correlated systems, such as C60. For these systems, ev-GW calculations result in excellent agreement with experimental data. Application of the ev-GW in order to evaluate the electronic structure of organic semiconductors is in our future plans.

2.5 Basis sets

Until now, we have not defined the one-electron wavefunctions ψ_i. For a finite system, one-electron wavefunctions (molecular orbitals) can be expressed as a linear combination of atomic orbitals (ϕ_μ), also refereed to as a *basis set*. Thus, molecular orbital ψ_i can be written as:

$$\psi_i = \sum_{\mu=1}^{n} c_{\mu i} \phi_\mu, \tag{2.19}$$

where the $c_{\mu i}$ coefficients should be determined. The problem of the calculating one-electron wavefunctions then reduces to the problem of calculating the set of optimal expansion coefficients. Optimal values of the coefficients are obtained by self-consistently solving the one-electron Equation (2.5) in the case of HF, or Equation (2.8) in the case of DFT. To date, the most widely used basis sets are based on Gaussian-shaped functions generated by Pople and co-workers (3-21G, 6-31G, *etc.*) [34] and Dunning and co-workers (cc-pVDZ, aug-cc-pVDZ, *etc.*) [35]. A wide variety of Gaussian basis sets are available at the EMSL basis set exchange website (https://bse.pnl.gov/bse/portal). We employ the Pople basis sets throughout this work.

In a perfect periodic molecular system, the nuclei are arranged in a regular repeating fashion in the static picture. Thus, the external potential acting on electrons should also be a periodic function ($V_{nuc}(r) = V_{nuc}(r + a)$), the period ($a$) being related to the unit-cell dimensions of crystal. By employing Bloch's theorem it is possible to express the wavefunction of an infinite periodic system (polymer, surface or crystal) in terms of wavefunctions described at reciprocal space vectors of a lattice. By applying Bloch's theorem, it is possible to reduce the infinite number of wavefunctions, that are required to describe an infinite system, to just the number of electrons present in the unit cell. To accomplish this, the one-electron wavefunction can be written as:

$$\psi(r + a) = \exp(ika)\,\phi(r), \tag{2.20}$$

where $\exp(ikr)$ is a phase factor, k is the wavevector in reciprocal space, r is the coordinate in real space; $\phi(r)$ is a strictly periodic function: $\phi(a + r) = \phi(r)$. Thus, each wavefunction $\psi_{nk}\rangle$ depends on the energy level n and wavevector k. Similarly to finite systems, one-electron wavefunctions can be expressed using a basis set. In the case of a plane-wave expansion, the one-electron wavefunction can be expressed using a finite set of plane waves (Fourier series):

$$\phi_i(r) = \sum_G c_{i,G} \exp(iGr), \tag{2.21}$$

where G is the reciprocal lattice vector. Plugging Equation (2.21) into Equation (2.20) we obtain:

$$\psi = \sum_G c_{i,k+G} \exp(i(G + k)r). \tag{2.22}$$

Similarly to the finite-system case, optimal coefficients $c_{i,k+G}$ have to be obtained. We note that, unlike in the finite-system case, these coefficients depend also on the k-point, thus the energy and wavefunctions of the system need to be converged against, not only

the basis set size, but also the size of the *k*-point mesh. Electronic band structure of the system is just a collection of band energies at different *k*-points in the reciprocal space. For a more detailed description of the theory underlying electronic structure of solids refer to Ref. [36]. We employ calculations with periodic boundary conditions throughout this work.

2.6 Evaluation of the lattice vibrations

Besides the purely electronic properties of a system with fixed nuclei coordinates, the 'soft' character of the van der Waals bound molecular crystals can lead to strong interactions between charge carriers and lattice vibrations in crystals and thin films, thus affecting charge generation and transport in these materials [37,38]. In order to obtain lattice vibrations (phonons), one expands the total energy of a periodic system about atomic displacements:

$$E = E_0 + \sum_{k,a} \frac{\partial E}{\partial u_{k,a}} u_{k,a} + \frac{1}{2} \sum_{k,a} u_{k,a} \Phi_{\alpha,\alpha\prime}^{k,k\prime} u_{k\prime,a\prime} + \cdots, \qquad (2.23)$$

where $u_{k,a}$ is the vector of atomic displacement a for atom k and $\Phi_{\alpha,\alpha\prime}^{k,k\prime}$ is the matrix of force constants (Hessian matrix):

$$\Phi_{\alpha,\alpha\prime}^{k,k\prime} = \frac{\partial^2 E}{\partial u_{k,a} \, \partial u_{k\prime,a\prime}}. \qquad (2.24)$$

At equilibrium, E_0 is the ground-state energy of the relaxed structure, and forces $\left(-\frac{\partial E}{u_{k,a}}\right)$ are all zero. In the harmonic approximation, terms beyond the 2nd derivatives are neglected. In the case when periodic boundary conditions are applied, one is looking for the Fourier transform of the force matrix, called the *dynamical matrix*:

$$D_{\alpha,\alpha\prime}^{k,k\prime}(q) = \frac{1}{\sqrt{M_k M_{k\prime}}} \sum_\alpha \Phi_{\alpha,\alpha\prime}^{k,k\prime}(a) e^{-iq \cdot R_a}. \qquad (2.25)$$

In the case of the Γ-point (center of the Brillouin zone), *i.e.*, when wavevector $q = 0$, the dynamical matrix is equal to the Hessian matrix multiplied by a normalization factor $1/\sqrt{M_k M_{k'}}$. By diagonalization of the dynamical matrix $D_{\alpha,\alpha'}^{k,k'}(q)$, the lattice modes (eigenvectors) and mode frequencies (eigenvalues) are obtained. In this work, we evaluate phonons only at the Γ-point. Recently, it was shown that phonons beyond Γ-point could be important for local and nonlocal electron-phonon couplings in pentacene crystal [39], a throughout investigation of the influence of phonon modes spanning the entire Brillouin zone on transport properties in organic semiconductors is one of our future considerations (Chapter 8). The 2nd-order derivative of energy with respect to atomic displacements is equal to the 1st-derivative of the force with respect to atomic displacements. These force derivatives can be computed and are related to the ground-state electron density by the Hellmann-Feynman relation [40]. This method is implemented in CRYSTAL [41], Quantum-ESPRESSO [42] and VASP [43]. We employ this method in Chapters 4-7.

2.7 Simulations of Infra-red (IR) and off-resonance Raman spectra

In order to simulate the IR and Raman spectra of a periodic system, the knowledge of the lattice vibrations at the Γ-point is necessary. Porezag and Pederson showed that, within DFT, the IR intensity of a lattice vibration *i* can be written as [44]:

$$I_i^{IR} = \frac{N\pi}{3c} \left| \frac{d\mu}{dQ_i} \right|^2,$$
(2.26)

where N is the particle density, c is the speed of light, and μ is the dipole moment. Thus, the IR intensity solely depends on the 2nd derivative of the dipole moment with respect to a normal mode Q_i. Since, besides the phonons, only the electric dipole is required, which

can be calculated based on the ground-state density, the IR intensity can be computed using LDA, GGA, or hybrid functionals. Calculation of the IR intensities has been implemented in several software packages and successfully applied for a wide range of both finite and periodic systems [45]. We successfully calculated the IR intensities of several organic crystalline semiconductors using this approach (Chapters 4 and 5).

In the same report [44], Porezag and Pederson showed that the off-resonance Raman intensities can be evaluated using the derivatives of the polarizability (α) and hyperpolarizability (β) with respect to normal modes (Q_i):

$$I_i^{Ram} = 45 \left(\frac{d\alpha}{dQ_i}\right)^2 + 7 \left(\frac{d\beta}{dQ_i}\right)^2 = 45\alpha_i'^2 + 7\beta_i'^2. \tag{2.27}$$

Since the Raman intensity is a scalar quantity and both the polarizability and hyperpolarizability are tensor quantities, scalar averages of α and β are defined as:

$$\alpha' = \frac{1}{3}(\alpha'_{xx} + \alpha'_{yy} + \alpha'_{zz}) \quad \text{and} \quad \beta'^2 = \frac{1}{2}[\left(\alpha'_{xx} - \alpha'_{yy}\right)^2 + (\alpha'_{xx} -$$

$$\alpha'_{zz})^2 + \left(\alpha'_{yy} - \alpha'_{zz}\right)^2 + 6(\alpha'_{xy}{}^2 + \alpha'_{xz}{}^2 + \alpha'_{yz}{}^2)]. \tag{2.28}$$

Within periodic boundary conditions calculations, the polarizability is related to the static macroscopic dielectric tensor (ε) by the Clausius-Mossotti correction [36]. Unfortunately, the calculation of the macroscopic dielectric tensor is more complicated than that of the dipole moments, depending on the chosen functional, GGA or hybrid, different ways to obtain ε have been proposed. Nevertheless, several groups have reported good agreement between the calculated and measured Raman spectra [46]. We obtained a good agreement with the measured Raman spectra of several organic crystals (Chapters 5, 7).

2.8 Molecular dynamics simulations

In the molecular dynamics (MD) simulations, the atoms are approximated as spheres connected by harmonic springs (emulating chemical bonds to other atoms). The potential energy surface of a system is evaluated using a set of force fields. The force field (FF) for each atom type represents a parameterized function generated on the basis of experimental data and/or high-level quantum-mechanical calculations. Various force fields have been developed for biological and organic systems. In particular, throughout this work, we employ the COMPASS force field [47]. It has been parameterized and validated against condensed-phase properties of molecular systems and thus should provide accurate prediction of structural, vibrational and physical properties for a broad range of organic materials.

The potential energy surface (E_{tot}) of a system is described as a sum of bonded (E_{bond}) and non-bonded ($E_{non\text{-}bonded}$) interactions included in the FF. Bonded energy is calculated as a sum of several energies related to covalent interactions: bond stretching (E_R), bond angle bending (E_θ), dihedral angle torsion (E_ϕ) and inversion term (E_ω). Non-bonded energy is calculated as a sum of the long-range electrostatic interaction (E_{el}) and van der Waals interactions (E_{vdW}). All these interactions are defined with a FF.

A molecular dynamics run starts by defining a set of initial velocities; then, the system is followed along a trajectory that is generated by calculating forces and new velocities at each step (using classical equations of motion). In order to enforce a specific environment (bath) for a calculation (for instance: constant finite temperature, constant number of

particles, and constant volume, which would correspond to the canonical ensemble (NVT)) different integrators are employed. The role of the integrator is to keep parameters required as close to constant as possible at every step of the trajectory. Since we are interested in charge-transport parameters at a finite temperature we employ the NVT ensemble with Andersen thermostat in this work [48].

2.9 References

[1]   Szabo, A.; Ostlund, N. *Modern Quantum Chemistry: Introduction to Advanced Electronic Structure Theory (Dover Books on Chemistry)*; Dover Publications, 1996.

[2]   Hohenberg, P.; Kohn, W. *Physical Review* **1964**, *136*, B864.

[3]   Kohn, W.; Sham, L. J. *Physical Review* **1965**, *140*, A1133.

[4]   Perdew, J. P.; Zunger, A. *Physical Review B* **1981**, *23*, 5048.

[5]   Perdew, J. P.; Burke, K.; Ernzerhof, M. *Physical Review Letters* **1996**, *77*, 3865.

[6]   Perdew, J. P.; Burke, K.; Ernzerhof, M. *Physical Review Letters* **1997**, *78*, 1396.

[7]   Hao, P.; Sun, J.; Xiao, B.; Ruzsinszky, A.; Csonka, G. I.; Tao, J.; Glindmeyer, S.; Perdew, J. P. *Journal of Chemical Theory and Computation* **2012**, *9*, 355.

[8]   Toulouse, J.; Adamo, C. *Chemical Physics Letters* **2002**, *362*, 72.

[9]   Xiao, H.; Tahir-Kheli, J.; Goddard, W. A. *The Journal of Physical Chemistry Letters* **2011**, *2*, 212.

[10]   Giovannetti, G.; Kumar, S.; Stroppa, A.; van den Brink, J.; Picozzi, S. *Physical Review Letters* **2009**, *103*, 266401.

[11]   Becke, A. D. *Physical Review A: Atomic, Molecular, and Optical Physics* **1988**, *38*, 3098.

[12]   Lee, C.; Yang, W.; Parr, R. G. *Physical Review B: Condensed Matter* **1988**, *37*, 785.

[13]   Adamo, C.; Barone, V. *The Journal of Chemical Physics* **1999**, *110*, 6158.

[14]   Toulouse, J.; Colonna, F.; Savin, A. *Physical Review A* **2004**, *70*, 062505.

[15]   Heyd, J.; Scuseria, G. E.; Ernzerhof, M. *The Journal of Chemical Physics* **2003**, *118*, 8207.

[16]   Chai, J.-D.; Head-Gordon, M. *The Journal of Chemical Physics* **2008**, *128*, 084106.

[17]   Baer, R.; Livshits, E.; Salzner, U. *Annual Review of Physical Chemistry* **2010**, *61*, 85.

[18]   Körzdörfer, T.; Bredas, J.-L. *Accounts of Chemical Research* **2014**, *47*, 3284.

[19]   Yanai, T.; Tew, D. P.; Handy, N. C. *Chemical Physics Letters* **2004**, *393*, 51.

[20]   Refaely-Abramson, S.; Sharifzadeh, S.; Govind, N.; Autschbach, J.; Neaton, J. B.; Baer, R.; Kronik, L. *Physical Review Letters* **2012**, *109*, 226405.

[21]   Janak, J. F. *Physical Review B* **1978**, *18*, 7165.

[22]   Stein, T.; Eisenberg, H.; Kronik, L.; Baer, R. *Physical Review Letters* **2010**, *105*, 266802.

[23]   Lopata, K.; Reslan, R.; Kowalska, M.; Neuhauser, D.; Govind, N.; Kowalski, K. *Journal of Chemical Theory and Computation* **2011**, *7*, 3686.

[24]   Livshits, E.; Baer, R. *The Journal of Physical Chemistry A* **2008**, *112*, 12789.

[25]   Onida, G.; Reining, L.; Rubio, A. *Reviews of Modern Physics* **2002**, *74*, 601.

[26]   Hedin, L. *Physical Review* **1965**, *139*, A796.

[27]   Hybertsen, M. S.; Louie, S. G. *Physical Review B* **1986**, *34*, 5390.

[28]   Jain, M.; Chelikowsky, J. R.; Louie, S. G. *Physical Review Letters* **2011**, *107*, 216806.

[29]   Tiago, M. L.; Northrup, J. E.; Louie, S. G. *Physical Review B* **2003**, *67*, 115212.

[30]   Sharifzadeh, S.; Biller, A.; Kronik, L.; Neaton, J. B. *Physical Review B* **2012**, *85*, 125307.

[31]   Dabo, I.; Ferretti, A.; Park, C.-H.; Poilvert, N.; Li, Y.; Cococcioni, M.; Marzari, N. *Physical Chemistry Chemical Physics* **2013**, *15*, 685.

[32]   Faber, C.; Boulanger, P.; Attaccalite, C.; Duchemin, I.; Blase, X. *Philosophical Transactions of the Royal Society of London A: Mathematical, Physical and Engineering Sciences* **2014**, *372*.

[33]   Körzdörfer, T.; Marom, N. *Physical Review B* **2012**, *86*, 041110.

[34]   Hehre, W. J.; Ditchfield, R.; Pople, J. A. *The Journal of Chemical Physics* **1972**, *56*, 2257.

[35]   Dunning, T. H. *The Journal of Chemical Physics* **1989**, *90*, 1007.

[36]   Ashcroft, N.; Mermin, D. *Solid State Physics*; Thomson Learning, 1976.

[37]   Coropceanu, V.; Cornil, J.; da Silva Filho, D. A.; Olivier, Y.; Silbey, R.; Bredas, J. L. *Chemical Reviews* **2007**, *107*, 926.

[38]   Sánchez-Carrera, R. S.; Paramonov, P.; Day, G. M.; Coropceanu, V.; Bredas, J. L. *Journal of the American Chemical Society* **2010**, *132*, 14437.

[39]   Yi, Y.; Coropceanu, V.; Brédas, J.-L. *The Journal of Chemical Physics* **2012**, *137*, 164303.

[40]   Feynman, R. P. *Physical Review* **1939**, *56*, 340.

[41]   Dovesi, R.; Orlando, R.; Civalleri, B.; Roetti, C.; Saunders, V. R.; Zicovich-Wilson, C. M. *Zeitschrift für Kristallographie - Crystalline Materials* **2005**, *220*, 571.

[42]   Giannozzi, P.; Baroni, S.; Bonini, N.; Calandra, M.; Car, R.; Cavazzoni, C.; Ceresoli, D.; Chiarotti, G. L.; Cococcioni, M.; Dabo, I.; Corso, A. D.; Gironcoli, S. d.; Fabris, S.; Fratesi, G.; Gebauer, R.; Gerstmann, U.; Gougoussis, C.; Kokalj, A.; Lazzeri, M.; Martin-Samos, L.; Marzari, N.; Mauri, F.; Mazzarello, R.; Paolini, S.; Pasquarello, A.; Paulatto, L.; Sbraccia, C.; Scandolo, S.; Sclauzero, G.; Seitsonen, A. P.; Smogunov,

A.; Umari, P.; Wentzcovitch, R. M. *Journal of Physics: Condensed Matter* **2009**, *21*, 395502.

[43]   Kresse, G.; Furthmüller, J. *Computational Materials Science* **1996**, *6*, 15.

[44]   Porezag, D.; Pederson, M. R. *Physical Review B* **1996**, *54*, 7830.

[45]   Zvereva, E. E.; Shagidullin, A. R.; Katsyuba, S. A. *The Journal of Physical Chemistry A* **2010**, *115*, 63.

[46]   Giannozzi, P.; Baroni, S. *The Journal of Chemical Physics* **1994**, *100*, 8537.

[47]   Bunte, S. W.; Sun, H. *Journal of Physical Chemistry B* **2000**, *104*, 2477.

[48]   Andersen, H. C. *The Journal of Chemical Physics* **1980**, *72*, 2384.

CHAPTER 3

CHARGE-TRANSPORT PROPERTIES IN SINGLE-COMPONENT

ORGANIC SEMICONDUCTORS: THE CASE OF NONLINEAR

ACENES

3.1 Introduction

Polyaromatic hydrocarbon (PAH) materials with a nonlinear molecular structure have recently received much attention as, unlike their linear oligoacene counterparts, they have been shown to be much more stable and much less reactive with other molecular entities, such as fullerenes [1]. To date, the electronic structure and charge-transport characteristics of several two-dimensional TIPS-functionalized (TIPS = triisopropylsilyl) acenes have been reported. For example, the TIPS-functionalized dibenzo[*def*, *mno*]chrysene was recently prepared and employed as an electron donor in bulk heterojunction solar cells, with efficiencies of more than 2% [2]. It should be noted that most polycyclic aromatic hydrocarbons can be viewed as "pyrene derivatives", where the change in molecular structures relative to pyrene might bring a dramatic influence on the morphological and electronic properties [3]. PAH materials have been also reported to exhibit high OFET mobilities [4,5]. Single-crystal OFETs based on nonlinear acenes offer a unique platform to study the impact of polymorphism on charge transport, where the effect of subtle changes in molecular packing can be investigated without the complexity of the microstructure, which is always present in thin-film devices. Such information is critical in material design and crystal engineering. Single-crystal OFET

data also allow easier comparison with the results of electronic-structure calculations, to evaluate the intrinsic charge-transport processes in these materials.

In the first part of this Chapter, we report a comparative analysis of the effect of the molecular and crystal structure on the electronic and optical properties and charge-transport characteristics of a series of novel TIPS-functionalized PAHs (**1-8**, Figure 3.1), the aim being to connect fundamental principles of molecular design to crystal packing and charge transport. In the second part of this Chapter, we present a comparative study of electronic and charge-transport properties of two stable packing polymorphs of 7,14-bis((trimethylsilyl)ethynyl)dibenzo[*b,def*]-chrysene (**9**). We evaluate how changes in crystalline packing can affect the charge-transport characteristics of nonlinear acenes. This Chapter is based on the results published in the *The Journal of the American Chemical Society* [6], *Chemistry – A European Journal* [7], and *Chemistry of Materials* [8].
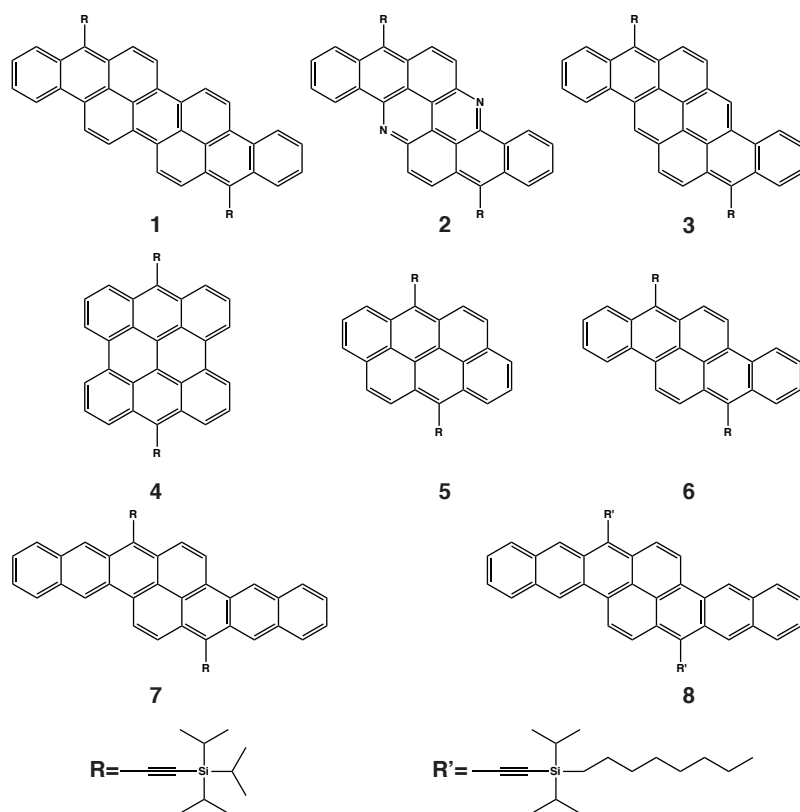
Figure 3.1 Molecular structures of TIPS-functionalized PAHs (**1-8**).

3.2 Computational Methodology

The molecular geometries and vibrational frequencies of the neutral and radical-ion states of **1-7** were derived using density functional theory (DFT). The DFT calculations were performed using the B3LYP functional and the long-range corrected ωB97 functional with the 6-31G** basis set [9]. In the case of the ωB97 functional, the ω value of each molecule was optimized by minimizing the difference between the HOMO eigenvalue of the ground state and the vertical ionization potential [10]. The optimized ω values are equal to 0.140, 0.148, 0.147, 0.152, 0.164, 0.153, and 0.141 bohr^{-1} for **1-7**, respectively. The TD-DFT approach was used for the evaluation of the energies of the lowest singlet excited states. To get a better insight into the nature of the S$_0$→S$_1$ transition, natural

transition orbital analyses were performed following time-dependent density functional theory (TD-DFT) calculations [11]. Since molecules **7** and **8** differ only in the length of the alkane chain, only the molecular electronic structure of **7** is reported here. Transfer integrals for selected dimers of **1-8** were calculated at the DFT level by using a fragment orbital approach in combination with a basis set orthogonalization procedure [12]. All molecular DFT calculations were performed using the Gaussian09 package [13]. The electronic band structure and density of states (DOS) of **6-9** were calculated using periodic boundary conditions at the B3LYP/6-21G level with the CRYSTAL09 package [14].

3.3 Results and discussion

3.3.1 Absorption spectra and excited states

The experimental UV-vis spectra, measured in solution, along with the results obtained from time-dependent density functional theory (TD-DFT) calculations are shown in Figure 3.2 and listed in Table 3.1. The first absorption bands of all compounds, except **4**, show a well-defined vibrational structure that can be attributed to the coupling with high-energy C=C stretching modes (about 0.15-0.20 eV). Relative to the parent unsubstituted hydrocarbons, the maximum absorption values of the present compounds exhibit a red shift about 0.3 eV for all compounds (0.25 eV for **1**, **2**, and **6**, 0.29 eV for **3**, and 0.33 eV for **5**) except **4** that exhibits a red shift of 0.12 eV. For the sake of comparison, we note that TIPS-functionalized linear acenes show a red shift relative to their parent aromatic hydrocarbons that decreases from 0.47 eV to 0.14 eV when going from anthracene to pentacene [15].
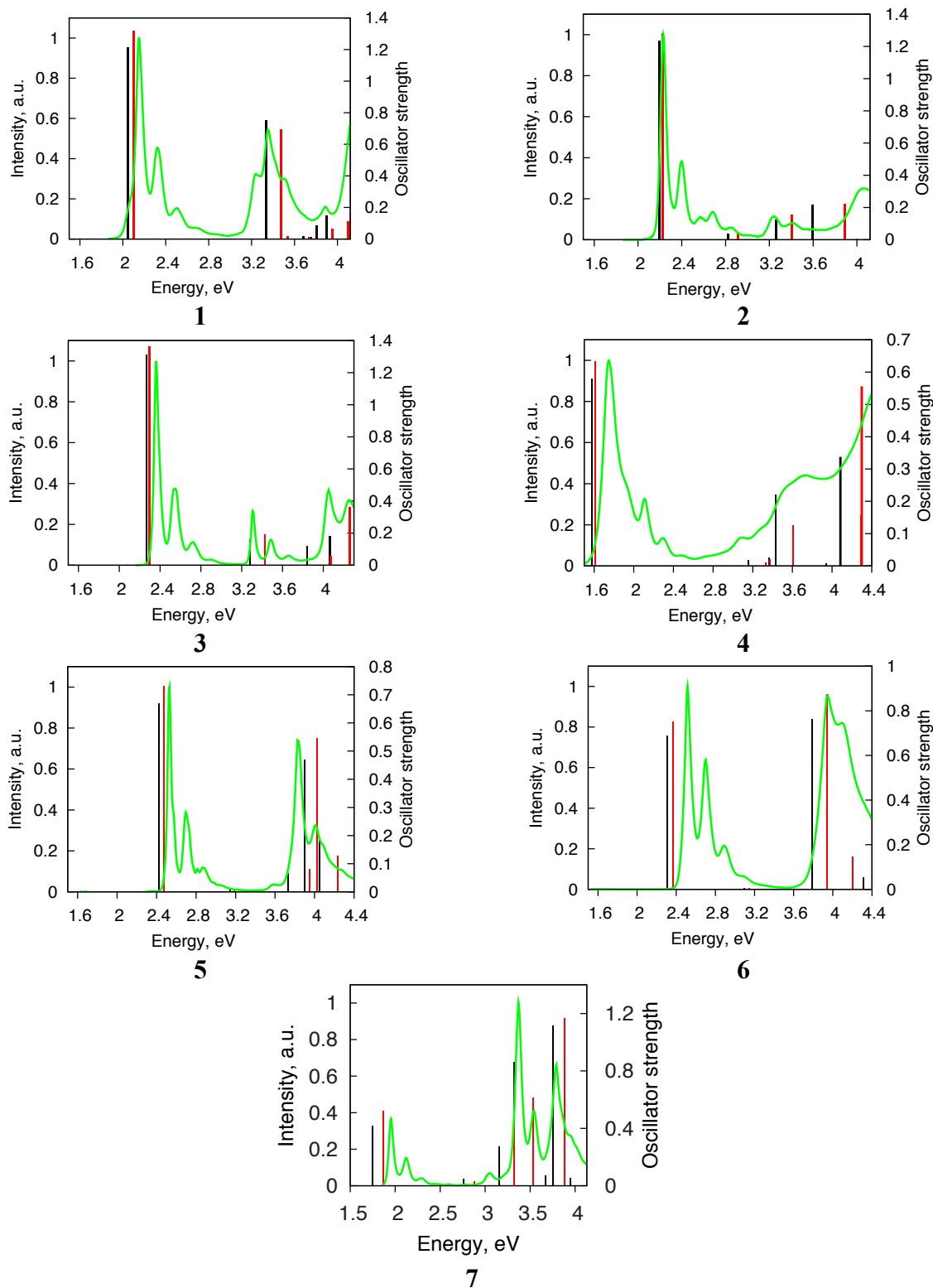
Figure 3.2 Experimental absorption spectrum (green line) of **1-7** with transitions energies and oscillator strengths for lowest-lying states obtained from B3LYP/6-31G** (black bars) and ωB97/6-31G** (red bars) calculations.

Table 3.1 Experimental and TD-DFT (eV) $S_0 \rightarrow S_1$ transition energies (E_{S1}) in **1-7**. The experimental data for the unsubstituted molecules are also provided.

Compound	E_{S1} [exp][a]	E_{S1} [B3LYP]	E_{S1} [ωB97]	E_{S1} [exp][b]
1	2.13	2.05	2.10	2.38[c]
2	2.23	2.20	2.23	2.48[d]
3	2.36	2.26	2.30	2.65[e]
4	1.75	1.58	1.61	1.87[f]
5	2.53	2.42	2.48	2.86[g]
6	2.52	2.30	2.37	2.78[h]
7	1.95	1.80	1.87	2.13[i]

[a] Measurement performed in chloroform solution. [b] The maximum absorption of parent unsubstituted molecules. [c] Iso-violanthrene, measurement performed in 1,2,4-trichlorobenzene [16]. [d] 8,16-Diazapyranthrene, measurement performed in 1,2,4-trichlorobenzene [17]. [e] Pyranthrene, measurement performed in 1,2,4-trichlorobenzene [17]. [f] Bisanthene, measurement performed in benzene [18]. [g] anthanthrene, measurement performed in benzene [18]. [h] Dibenzo[*def, mno*]chrysene, measurement performed in ethanol [19]. [i] Bistetracene, measurement performed in 1-methylnaphthalene [20].

In general, the electronic properties of two-dimensional acenes depend on both molecular size and molecular topology (edge structure) [21]. A simple interpretation of the photophysical properties of these systems can be obtained in the framework of Clar's aromatic sextet model [22]. According to Clar's sextet rule the system stability and the fundamental gap increases with the number of aromatic sextet rings present in the system (Figure 3.3).
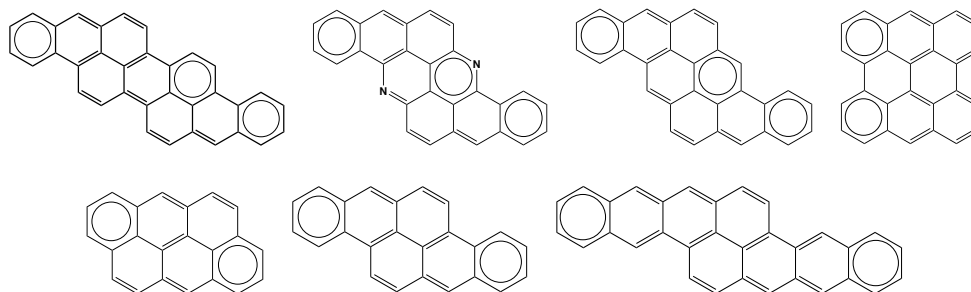
Figure 3.3 Clar structures of iso-violanthrene, pyranthrene, diazapyranthrene, bisanthene, anthanthrene, dibenzo[*def, mno*]chrysene, and bistetracene.

For instance, **5** and **6** (and their parent molecules) consist of six benzene rings and both have two sextets; therefore, they are expected to exhibit comparable optical gaps. With the extension of the π-conjugated system, the energy gaps (both fundamental and optical) are decreasing, from 2.48 eV for **5** (ωB97 value) to 1.87 eV for **7** and **8**. Indeed the cyclic voltammetry data and the DFT results confirm this prediction [6,7]. In addition, TD-DFT calculations reveal that the first optical band in all the present systems is described by a $S_0 \rightarrow S_1$ transition that is dominated by HOMO-to-LUMO excitation (this conclusion is also supported by the calculations of natural transition orbitals, see Figure 3.4). The TD-DFT results combined with Clar's sextet rule explain why **5**, **6**, and **7** show comparable absorption bands. Molecules **3** and **4** consist of eight benzene rings; however, compound **3** possesses three aromatic sextets while molecule **4** has two. As a result, the energy of the S_1 state of **3** is much larger than that of **4**. It is important to note that recent studies suggest that the low gap and high energy of the HOMO in bisanthene (as is the case for periacenes in general), the parent molecule of **4**, is related to the diradical character of the ground state of this molecule arising from localized electronic states at the zigzag edges [23]. Compared to compound **3**, the absorption maximum of **2** is red shifted by 0.13 eV [24]. Molecule **1** possesses three aromatic sextets and a similar edge structure as

molecule **3**; therefore, the slight redshift of the $S_0 \rightarrow S_1$ transition observed when going from **3** to **1** can be attributed to the increase in the molecular size of **1**. As seen from Figure 3.2, the TD-DFT calculations performed at the B3LYP/6-31G** and ωB97/6-31G** levels yield similar results and are in excellent agreement with the experimental data.

1 (λ=0.98)

2 (λ=0.98)

3 (λ=0.98)

4 (λ=1.0)

5 (λ=0.98)

6 (λ=0.99)
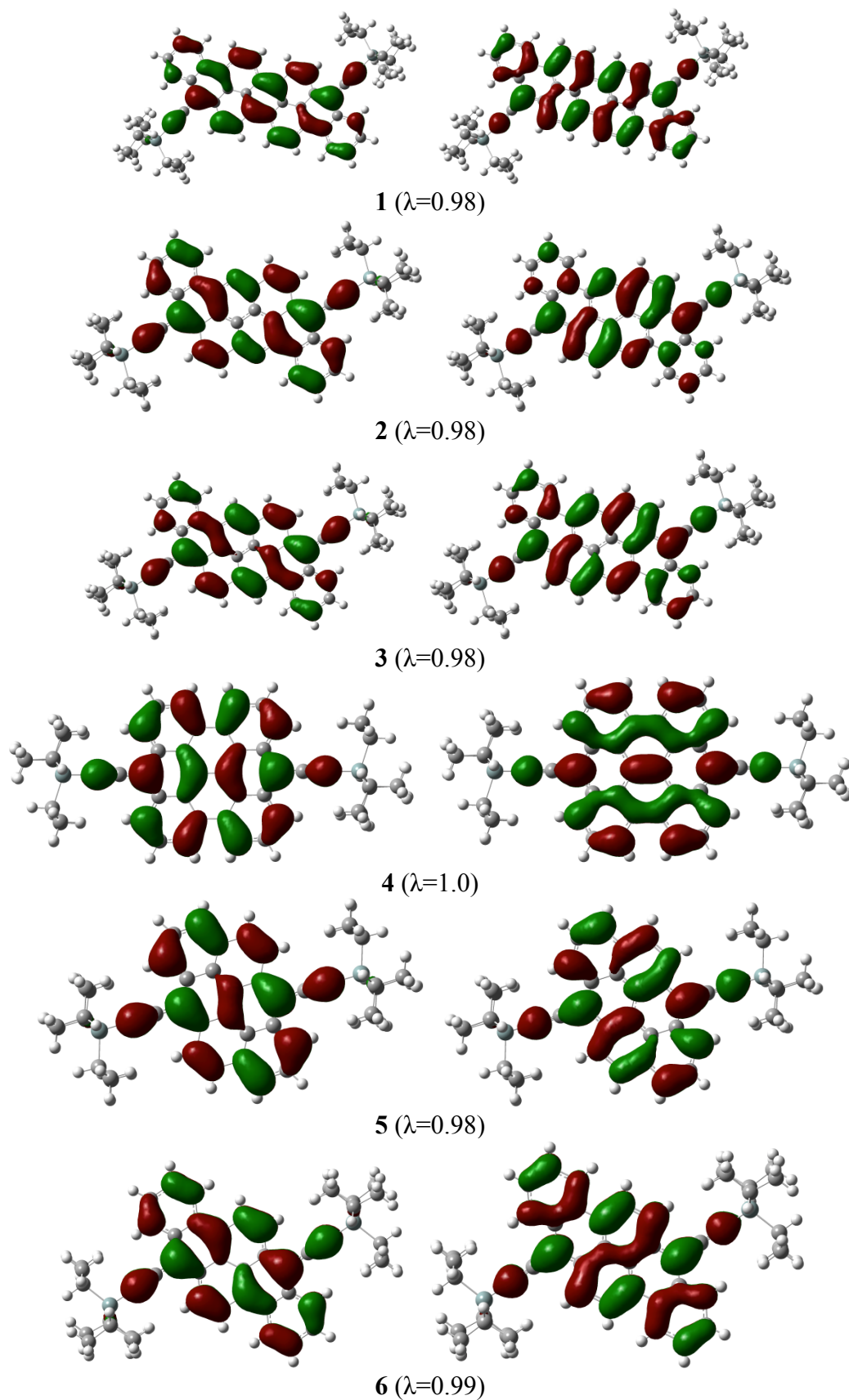
Figure 3.4 Natural transition orbitals related to the $S_0 \rightarrow S_1$ transition: hole (left) and electron (right) wavefunctions at the tuned ωB97 level. λ is the weight of contribution of an occupied-virtual pair to the excitation.

3.3.2 Molecular and crystal structures

First we discuss the crystal packing of the reported compounds, since it is important for overall charge transport [25]. Generally, unsubstituted linear acenes fall into the class of herringbone packing motifs due to the dominance of C–H…π interactions in the solid state [26]. However, it has been pointed out that TIPS groups promote linear polyacenes to crystallize in a π-stacked, more cofacial arrangement [27]. Compared to linear polyacenes, which usually have large aspect ratios between length and width, the PAH molecules typically have comparable length and width, which has critical implications for molecular packing in the solid state [28].

The packing motifs of the 1-8 crystals are shown in Figure 3.5. The crystals of 1-3 exhibit a similar 1-D slipped-stack motif with similar π–π distance (3.38 Å along the a-axis) and significant π-surface overlap. Stacks formed from π-stacked molecules are canted relative to each other. Fairly long zigzag edges provide sufficient volume for reorientational rotation of the PAH molecules, probably due to the space-filling requirement of the bulky TIPS groups. Replacement of the carbon atoms by nitrogen atoms, when going from 2 to 3, neither changes the intermolecular interactions nor the intermolecular packing within a π-stack. Crystals of 4 and 5 exhibit a 1-D π-stacking motif with the triisopropylsilyl groups of adjacent molecules arranged in a nearly 90° alternating fashion to each other, so as to minimize steric interactions along stacks [29]. This type of intermolecular organization is reminiscent of the disc-like PAHs with flexible aliphatic chains, which give rise to a one-dimensional columnar arrangement. Shorter aromatic cores compared to the other compounds, preclude slipped π–π stacks along the long axis which would

form a 2-D stacking motif, and result in a 1-D packing arrangement with large π-surface overlap. Crystal **6** adopts a 2-D "brickwork" arrangement with an intra-stack distance of about 3.41 Å; this distance is very similar to that of TIPS-pentacene [30]. Crystal of **7** exhibits a slipped one-dimensional (1-D) π-stacking motif, similar to that observed for **1-3**. The interplanar distance in **7** is about 3.37 Å. Such a large inter-stack separation distance suggests poor electronic coupling between two adjacent stacks. By changing the substituent to the larger alkyl groups, the π-stacking motif in **8** changed to an interacting 2-D packing arrangement with close intra-stack contacts of 3.35 Å. Due to the presence of two translationally inequivalent molecules (*i.e.*, molecules related by different inversion centers), the stacks in **8** are characterized by two alternating intermolecular center-to-center distances of 8.59 and 8.01 Å between adjacent molecules. The introduction of long alkyl groups tends to reduce the distance between the different stacks. This is consistent with the stronger intermolecular van der Waals interactions among the longer alkyl groups ("zipper effect"), which result in tighter packing in the solid state [31].

Table 3.2. Summary of crystallographic data for **1-8**.

Crystal	Space group	a, Å	b, Å	c, Å	α, °	β, °	γ, °
1	P2$_1$/c	19.889	7.574	30.451	90	106.66	90
2	C2/c	38.970	7.785	29.422	90	14.73	90
3	C2/c	39.179	7.771	29.568	90	114.89	90
4	P-1	13.717	16.357	21.392	72.45	76.76	73.14
5 [29]	P-1	13.892	15.174	35.456	88.91	79.71	84.14
6 [2]	P-1	8.032	8.431	16.362	88.66	81.82	61.98
7	P-1	8.984	9.737	13.510	75.34	70.34	90.05
8	P-1	11.763	12.892	18.753	97.59	106.39	95.69
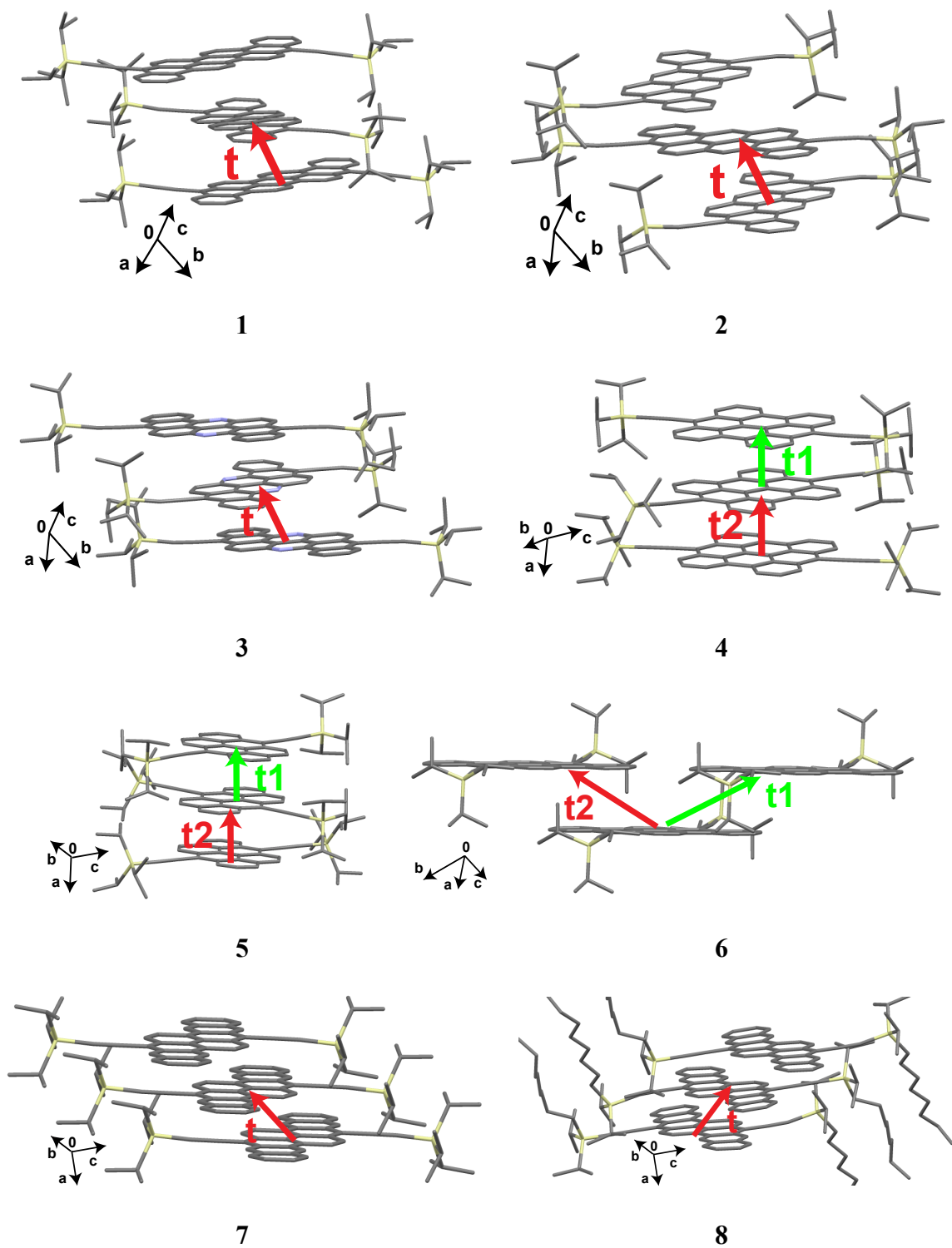
Figure 3.5 Crystal packing of **1**-**8**. Hydrogen atoms are omitted for clarity. The directions of large electronic couplings are marked with arrows.

3.3.3 Electronic structure and charge-transport characteristics

We turn now to a discussion of the electronic couplings, *i.e.*, the microscopic parameters that define the charge-transport properties [25]. The calculations of the electronic couplings (transfer integrals, t) are based on the experimental crystal geometries. The largest transfer integrals for both holes and electrons are found along the stacking directions for all systems, the related DFT estimates are listed in Table 3.3. The values of largest transfer integrals for holes range from 31 meV in **7** to 194 meV in **4.** All these values are comparable or larger than that (about 30 meV) estimated at a similar level of theory for TIPS-pentacene [32]. In contrast, the values of transfer integrals for electrons are in the range of 25-140 meV, which is smaller than the value of 180 meV estimated for TIPS-pentacene [32]. We note that in **4**, **5** and **8** there are two non-equivalent dimers along the stacking directions; this is in contrast to **1-3** where all dimers along a stacking direction are equivalent. The stacks in **4**, **5**, **7** and **8** are well separated by TIPS groups, which preclude electronic interactions between molecules located in different stacks. Indeed, inter-stack electronic couplings are found to be very small, on average around 3 meV and 1 meV for holes and electrons, respectively. Weak inter-stack couplings (in the range of 1-9 meV) are also found in **1-3**. Despite the 2-D stacking arrangement in the crystal of **6**, small hole [electron] couplings of 6 meV [2 meV] are found along the *b*-axis. Since the unit cells of systems **1-5** are too large to run periodic calculations, we used a one-dimensional tight-binding model (see Chapter 1) to estimate the effective masses of all systems along the stacking directions; the results are collected in Table 3.3.

Table 3.3 Distances between core centers (d, Å), DFT estimates of the electronic couplings (t, meV) and the related effective masses of **1-8** along the stacking directions within the tight-binding model.

Crystal	d, Å	hole		electron	
		t	m/m_0	t	m/m_0
1	3.79	75	3.54	86	3.08
2	3.89	75	3.36	133	1.89
3	3.89	123	2.05	140	1.80
4	3.46 (3.39)	-194 (143)	1.44	99 (85)	3.46
5	3.48 (3.48)	44 (40)	7.49	-105 (-90)	3.23
6	8.43	-78 (-6)	0.69	25 (2)	2.14
7	8.98	31	1.52	101	0.47
8	8.01 (8.59)	76 (-35)	1.00	47 (-69)	0.95

For crystals **6-8**, we evaluated the electronic band structures and effective masses using periodic boundary DFT calculations. In the case of **6**, the valence and conduction bandwidths are 0.40 and 0.12 eV, respectively. The corresponding transfer integrals for holes and electrons are estimated as 78 and 25 meV (Figure 3.6); in the framework of a one-dimensional tight-binding model, such transfer integrals would result in valence and conduction bandwidths of 0.31 and 0.10 eV, respectively, in good agreement with those from the periodic boundary conditions calculations. As a consequence of such relatively large transfer integrals, the effective masses along the stacking direction are small, 0.56 m_0 for holes and 0.99 m_0 for electrons.
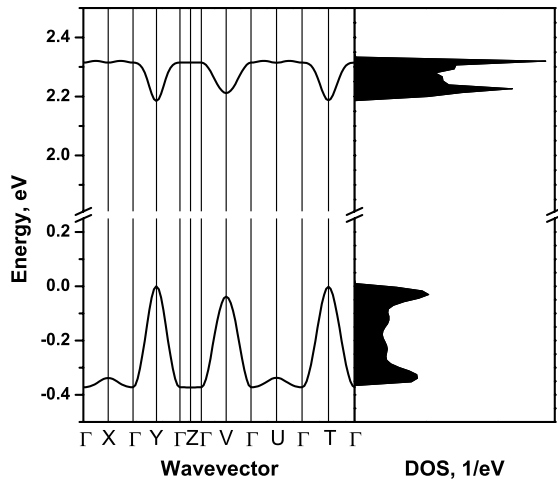
6
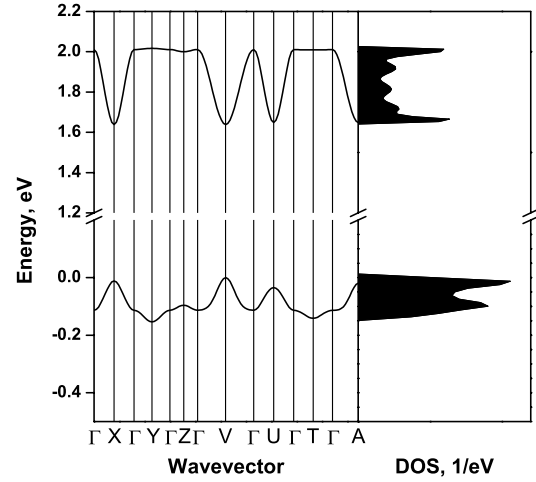
7
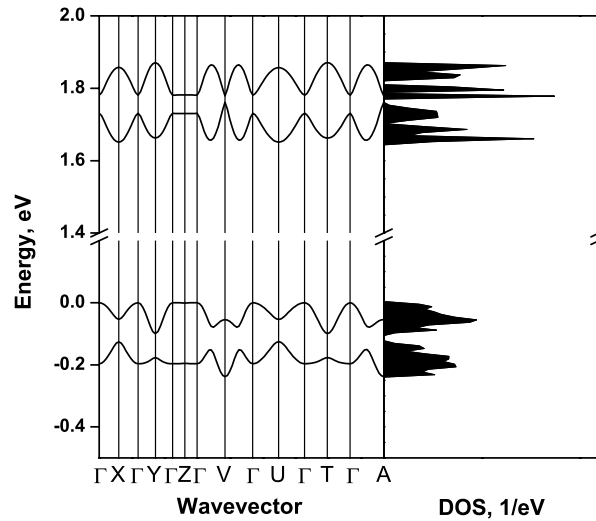
8

Figure 3.6 Calculated band structure and density of states (DOS) of **6-8**. The points of high symmetry in the first Brillouin zone are: Γ=(0, 0, 0), X=(0.5, 0, 0), Y=(0, 0.5, 0), Z=(0, 0, 0.5), V=(0.5, 0.5, 0), U=(0.5, 0, 0.5), T=(0, 0.5, 0.5), A=(0.5, 0.5, 0.5) all in crystallographic coordinates. The zero of energy corresponds to the top of the valence band.

A similar situation is found in the case of crystal **7**, for which the valence and conduction bandwidths are 0.17 and 0.4 eV, respectively. The corresponding transfer integrals for holes and electrons in the stacking direction are estimated as 31 and 101 meV; such

transfer integrals would result in valence and conduction bandwidths of 0.12 and 0.40 eV, respectively, in a 1-D tight-binding model. The effective masses along the stacking direction are small, 1.07 m_0 (where m_0 is the electron mass at rest) for holes and 0.53 m_0 for electrons. For the sake of comparison, we note that the effective masses for holes and electrons in pentacene are 1.60 m_0 and 1.45 m_0, respectively [33]. In crystal **8**, the valence and conduction bands consist of two sub-bands arising from the interaction of the HOMO and LUMO levels, respectively, of the two translationally inequivalent molecules present in the unit cell. The overall valence and conduction bandwidths are estimated to be 0.22 and 0.20 eV. As a result of two alternating intermolecular distances, the electronic couplings along the stacks are characterized by two transfer integrals, t_1 and t_2 (-35 and -76 meV for holes, and -69 and-47 meV for electrons). The band-structure calculations yield 1.05 m_0 and 0.97 m_0, respectively, for the hole and electron effective masses along the stacking direction. A tight-binding model (with two sites per unit cell) can be employed to rationalize the band structure for this system as well [34]. According to this model, the bandwidths in **8** are given by $2(|t_1| + |t_2|)$. The tight-binding estimates of 0.22 and 0.23 eV for the widths of the valence and conduction bands compare well with the above values derived from band-structure calculations. According to the same tight-binding model, the effective masses for charge carriers can be estimated as $m_{1D-eff} = \hbar^2/2t_{eff}d_{av}^2$, where $t_{eff} = 2|t_1 t_2|/2(|t_1| + |t_2|)$ and d_{av} is the average intermolecular distance along the stack [34]. The model yields nearly equal values for the effective transfer integrals for holes and electrons (48 meV *vs.* 55 meV), explaining why both types of carriers in **8** possess comparable effective masses. We note that the tight-binding calculations predict for the effective mass of holes in **8** a value that is ~30%

smaller than in the case of **7**, in contrast with the band-structure calculations showing that the effective masses for holes in both crystals are almost equal.

Table 3.4 Hole and electron effective masses of **6-8** in the units of the electron mass at rest (m_0) at the band extrema. The step-size for the numerical differentiations was set to 0.01 (1/Bohr).

		m/m_0	directions
6	holes at Y	0.56	$0.295a + 0.955b - 0.015c$
	(0, 0.5, 0)	5.96	$0.963a + 0.173b + 0.206c$
		35.23	$0.025a + 0.008b + c$
	electrons at Y	0.99	$0.196a + 0.978b - 0.074c$
	(0, 0.5, 0)	9.14	$0.958a + 0.287b + 0.003c$
		26.24	$0.073a + 0.030b + 0.997c$
7	holes at V	1.074	$a + 0.132b - 0.088c$
	(0.5, 0.5, 0)	4.511	$c - 0.424a + 0.370b$
		28.116	$b + 0.023a - 0.386c$
	electrons at X	0.530	$a - 0.010b - 0.016c$
	(0.5, 0, 0)	9.412	$c - 0.469a - 0.014b$
		Inf.	$b + 0.112a - 0.199c$
8	holes at Γ	1.054	$b + 0.488a + 0.001c$
	(0, 0, 0)	5.259	$a - 0.337b - 0.018c$
		110.134	$c + 0.508a + 0.222b$
	electrons at X	0.969	$b + 0.860a - 0.001c$
	(0.5, 0, 0)	22.400	$a - 0.720b - 0.075c$
		280.434	$c + 0.572a + 0.170b$

3.3.4 Impact of packing polymorphism on electronic structure and electronic charge-transport characteristics in nonlinear acenes

It was found that 7,14-bis((trimethylsilyl)ethynyl)dibenzo[*b,def*]-chrysene (**9**, see Figure 3.7) can exhibit two packing motifs: the low-temperature (**9LT**) polymorph forms within the 25–60 °C temperature range, whereas the high-temperature (**9HT**) polymorph forms within the 130–170 °C temperature range.
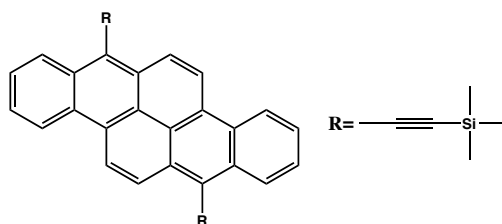
Figure 3.7 Molecular structure of **9**.

The crystal packing motifs of these polymorphs are shown in Figure 3.8. Two observed polymorphs of **9** crystallize in significantly different unit cells with very different degrees of co-facial packing. The **9LT** polymorph exhibits a 1-D slipped stacked packing where the intra-stack distance between aromatic carbon–carbon atoms is short at ~3.35 Å, with a high degree of spatial intermolecular π–π overlap between adjacent PAH units. The crystal packing of the **9HT** polymorph exhibits a 2-D brickwork motif with a slightly larger unit-cell volume compared to the **9LT** polymorph. Even closer C-C contacts of ~3.33 Å are observed; however, this is compensated by a slightly lower degree of π–π spatial overlap between adjacent PAH rings, presumably due to steric interactions of nearby (trimethylsilyl)ethynyl-capping groups.

9LT   **9HT**
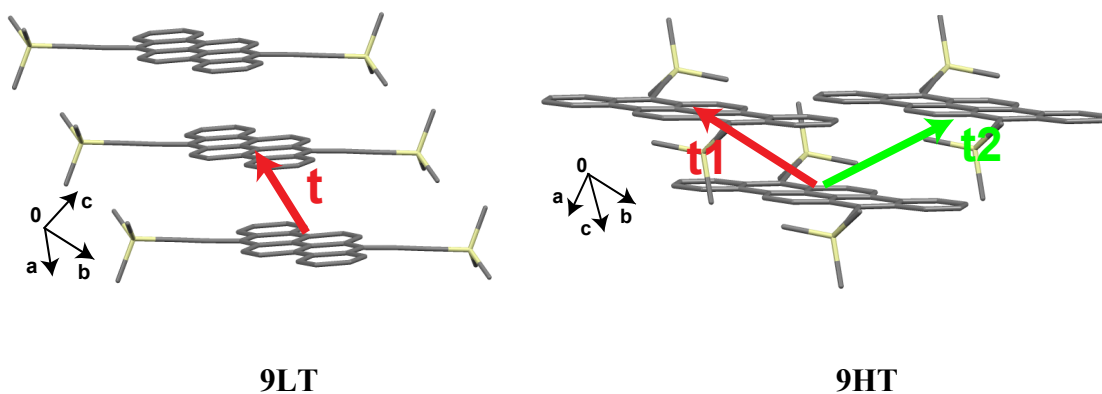
Figure 3.8 Crystal packing of **9**. Hydrogen atoms are omitted for clarity. Directions of large electronic couplings are marked with arrows.

In order to get a better understanding of the intrinsic charge-transport properties of the crystalline polymorphs, we investigated their electronic couplings and related electronic band structures using DFT (see Figures 3.8 and 3.9). In the **9LT** polymorph, the largest transfer integrals were found along the 1-D slipped stack, with the corresponding values for holes and electrons estimated as 76 and 5.5 meV. In the framework of a one-dimensional tight-binding model (where we recall that the bandwidths correspond to four times the transfer integrals), such transfer integrals would result in valence and conduction bandwidths of 0.3 and 0.02 eV, respectively. These values are in good agreement with those obtained directly from the periodic-boundary condition calculations (0.35 and 0.05 eV, respectively; see Figure 3.9). As a result of a relatively large hole electronic coupling, the effective hole mass along the stacking direction is small, 0.85 m_0. The other components of the effective mass tensor are large (>3 m_0), which suggests a 1-D character for hole transport. The smallest electron effective mass is calculated to be 4.04 m_0 (Table 3.5).
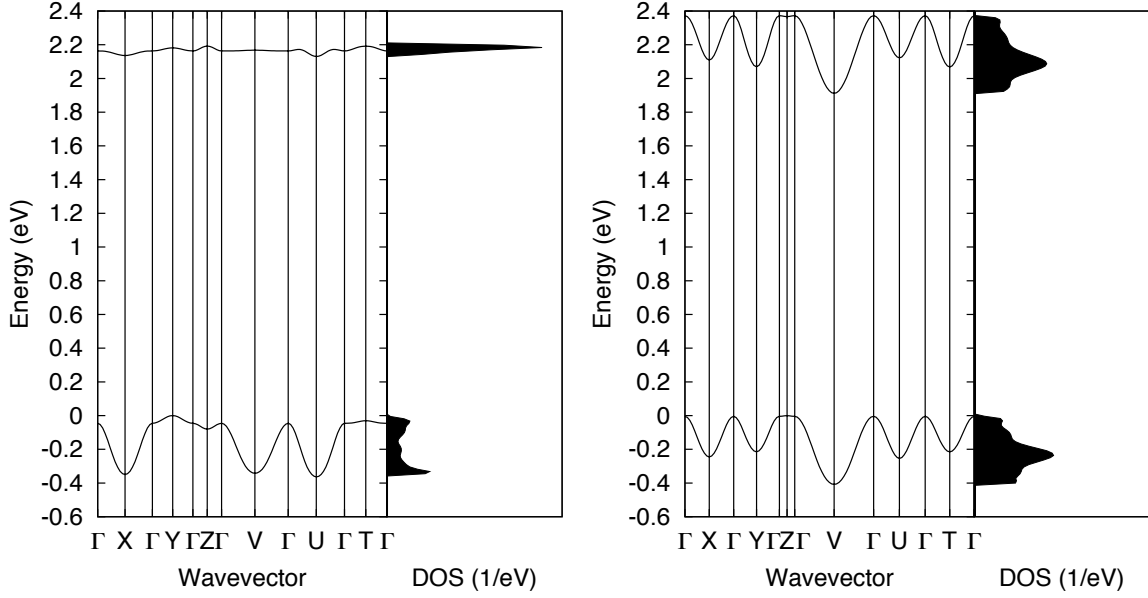
Figure 3.9 Calculated band structure and density of states (DOS) of **9LT** (left) and **9HT** (right). The points of high symmetry in the first Brillouin zone are: $\Gamma=(0, 0, 0)$, $X=(0.5, 0, 0)$, $Y=(0, 0.5, 0)$, $Z=(0, 0, 0.5)$, $V=(0.5, 0.5, 0)$, $U=(0.5, 0, 0.5)$, $T=(0, 0.5, 0.5)$ all in crystallographic coordinates. The zero of energy corresponds to the top of the valence band.

In the **9HT** polymorph, as a result of a 2-D brickwork packing motif, there are two large transfer integrals: 53 and 50 meV for holes, and 52 and 66 meV for electrons. The valence and conduction bandwidths estimated from band-structure calculations are about 0.40 and 0.44 eV. For this polymorph, two small effective masses are found along the stacking directions: 1.03 m_0 and 2.54 m_0 for holes and 1.34 m_0 and 3.0 m_0 for electrons, which is indicative of an intrinsic 2-D transport. For the sake of comparison, we note that the two smallest components of the hole effective mass in rubrene are 0.78 m_0 and 1.95 m_0, respectively [35].

Table 3.5 Hole and electron effective masses of **9** in the units of the electron mass at rest (m_0) at the band extrema. The step-size for numerical differentiations was set to 0.01 (1/Bohr).

		m/m_0	directions
9HT polymorph	holes at Z	1.030	$a - 0.990b + 0.010c$
	(0, 0, 0.5)	2.539	$a + 0.915b - 0.008c$
		10.687	$c + 0.146a + 0.252b$
	electrons at V	1.366	$b - 0.798a - 0.013c$
	(0.5, 0.5, 0.0)	2.986	$a + 0.837b + 0.072c$
		60.143	$c - 0.488a - 0.257b$
9LT polymorph	holes at Y	0.845	$a - 0.061b + 0.092c$
	(0, 0.5, 0)	3.241	$c + 0.965b - 0.843a$
		5.554	$b + 0.312a - 0.561c$
	electrons at U	4.039	$a - 0.380c + 0.234c$
	(0.5, 0, 0.5)	7.187	$b + 0.551a - 0.182c$
		74.189	$c - 0.968a + 0.140b$

3.4 Conclusions

We have described the electronic band structures, excitation energies. and microscopic charge-transfer parameters of several nonlinear annulated acenes that show attractive properties, such as significant electronic couplings, small effective masses and low-energy band gaps. High carrier mobilities have been measured in field-effect transistors based on single-crystals of the several systems reported here. In particular, average hole mobilities of 0.06, 0.05, 0.3, 3.90, 0.03 and 2.1 cm^2/Vs have been measured for compounds **4**, **6**, **7**, **8**, **9LT** and **9HT**, respectively. The OFET measurements and electronic-structure calculations demonstrate that these acenes exhibit excellent intrinsic charge transport properties. The experimental studies indicates that this annellation mode with an additional Clar sextet significantly increases the stability of this class of extended conjugated semiconductors and opens new opportunities to explore these materials in

mainstream applications such as bulk heterojunction solar cells and large-area, roll-to-roll solution-processable transistors.

We also evaluated the charge-transport properties of two crystal polymorphs of a nonlinear acene. The electronic-structure calculations point to a single large hole electronic coupling in the **9LT** polymorph and two large hole electronic couplings in the **9HT** polymorph. The higher mobility of the **9HT** polymorph is likely related to the better crystal quality and the availability of alternative pathways for charge carriers encountering defects or trap states. Further studies on comprehensive synthesis and structure-property relationships of even larger conjugated cores are now in progress, in collaboration with experimental groups from University of Massachusetts, Amherst, Wake Forest University, and CSIRO, Australia.

3.5 References

[1]   Cao, Y.; Liang, Y.; Zhang, L.; Osuna, S.; Hoyt, A.-L. M.; Briseno, A. L.; Houk, K. N. *Journal of the American Chemical Society* **2014**, *136*, 10743.

[2]   Winzenberg, K. N.; Kemppinen, P.; Fanchini, G.; Bown, M.; Collis, G. E.; Forsyth, C. M.; Hegedus, K.; Singh, T. B.; Watkins, S. E. *Chemistry of Materials* **2009**, *21*, 5701.

[3]   Figueira-Duarte, T. M.; Müllen, K. *Chemical Reviews* **2011**, *111*, 7260.

[4]   Shu, Y.; Collis, G. E.; Dunn, C. J.; Kemppinen, P.; Winzenberg, K. N.; Williamson, R. M.; Bilic, A.; Singh, T. B.; Bown, M.; McNeill, C. R.; Thomsen, L. *Journal of Materials Chemistry C* **2013**, *1*, 6299.

[5]   Burke, K. B.; Shu, Y.; Kemppinen, P.; Singh, B.; Bown, M.; Liaw, I. I.; Williamson, R. M.; Thomsen, L.; Dastoor, P.; Belcher, W.; Forsyth, C.; Winzenberg, K. N.; Collis, G. E. *Crystal Growth & Design* **2011**, *12*, 725.

[6]   Zhang, L.; Fonari, A.; Liu, Y.; Hoyt, A.-L. M.; Lee, H.; Granger, D.; Parkin, S.; Russell, T. P.; Anthony, J. E.; Brédas, J.-L.; Coropceanu, V.; Briseno, A. L. *Journal of the American Chemical Society* **2014**, *136*, 9248.

[7]   Zhang, L.; Fonari, A.; Zhang, Y.; Zhao, G.; Coropceanu, V.; Hu, W.; Parkin, S.; Brédas, J.-L.; Briseno, A. L. *Chemistry – A European Journal* **2013**, *19*, 17907.

[8]   Stevens, L. A.; Goetz, K. P.; Fonari, A.; Shu, Y.; Williamson, R. M.; Brédas, J.-L.; Coropceanu, V.; Jurchescu, O. D.; Collis, G. E. *Chemistry of Materials* **2015**, *27*, 112.

[9]   Chai, J.-D.; Head-Gordon, M. *The Journal of Chemical Physics* **2008**, *128*, 084106.

[10]   Stein, T.; Eisenberg, H.; Kronik, L.; Baer, R. *Physical Review Letters* **2010**, *105*, 266802.

[11]   Martin, R. L. *The Journal of Chemical Physics* **2003**, *118*, 4775.

[12]   Valeev, E. F.; Coropceanu, V.; da Silva Filho, D. A.; Salman, S.; Bredas, J. L. *Journal of the American Chemical Society* **2006**, *128*, 9882.

[13]   Frisch, M. J.; Trucks, G. W.; Schlegel, H. B.; Scuseria, G. E.; Robb, M. A.; Cheeseman, J. R.; Scalmani, G.; Barone, V.; Mennucci, B.; Petersson, G. A.; Nakatsuji, H.; Caricato, M.; Li, X.; Hratchian, H. P.; Izmaylov, A. F.; Bloino, J.; Zheng, G.; Sonnenberg, J. L.; Hada, M.; Ehara, M.; Toyota, K.; Fukuda, R.; Hasegawa, J.; Ishida, M.; Nakajima, T.; Honda, Y.; Kitao, O.; Nakai, H.; Vreven, T.; Montgomery, J. A.; Peralta, J. E.; Ogliaro, F.; Bearpark, M.; Heyd, J. J.; Brothers, E.; Kudin, K. N.; Staroverov, V. N.; Kobayashi, R.; Normand, J.; Raghavachari, K.; Rendell, A.; Burant, J. C.; Iyengar, S. S.; Tomasi, J.; Cossi, M.; Rega, N.; Millam, J. M.; Klene, M.; Knox, J. E.; Cross, J. B.; Bakken, V.; Adamo, C.; Jaramillo, J.; Gomperts, R.; Stratmann, R. E.; Yazyev, O.; Austin, A. J.; Cammi, R.; Pomelli, C.; Ochterski, J. W.; Martin, R. L.; Morokuma, K.; Zakrzewski, V. G.; Voth, G. A.; Salvador, P.; Dannenberg, J. J.; Dapprich, S.; Daniels, A. D.; Farkas; Foresman, J. B.; Ortiz, J. V.; Cioslowski, J.; Fox, D. J. Wallingford CT, 2009.

[14]   Dovesi, R.; Orlando, R.; Civalleri, B.; Roetti, C.; Saunders, V. R.; Zicovich-Wilson, C. M. *Zeitschrift für Kristallographie - Crystalline Materials* **2005**, *220*, 571.

[15]   Anthony, J. E. *Chemical Reviews* **2006**, *106*, 5028.

[16]   Iwashima, S.; Ueda, T.; Honda, H.; Tsujioka, T.; Ohno, M.; Aoki, J.; Kan, T. *Journal of the Chemical Society, Perkin Transactions 1* **1984**, 2177.

[17]   Aoki, J. *Bulletin of the Chemical Society of Japan* **1968**, *41*, 1017.

[18]   Birks, J. B. *Photophysics of Aromatic Molecules*; Wiley-Interscience: London, 1970.

[19]   Harvey, R. G.; Pataki, J.; Cortez, C.; Di Raddo, P.; Yang, C. X. *The Journal of Organic Chemistry* **1991**, *56*, 1210.

[20]   Clar, E. *Journal of the Chemical Society (Resumed)* **1949**, 2013.

[21]   Geim, A. K.; Novoselov, K. S. *Nat Mater* **2007**, *6*, 183.

[22]   Clar, E. *The Aromatic Sextet*; Wiley: London, 1972.

[23]   Jiang, D.; Sumpter, B. G.; Dai, S. *The Journal of Chemical Physics* **2007**, *127*, 124703.

[24]   Liang, Z.; Tang, Q.; Mao, R.; Liu, D.; Xu, J.; Miao, Q. *Advanced Materials* **2011**, *23*, 5514.

[25]   Coropceanu, V.; Cornil, J.; da Silva Filho, D. A.; Olivier, Y.; Silbey, R.; Bredas, J. L. *Chemical Reviews* **2007**, *107*, 926.

[26]   Gavezzotti, A.; Desiraju, G. R. *Acta Crystallographica Section B* **1988**, *44*, 427.

[27]   Anthony, J. E.; Eaton, D. L.; Parkin, S. R. *Organic Letters* **2001**, *4*, 15.

[28]   Tan, L.; Zhang, L.; Jiang, X.; Yang, X.; Wang, L.; Wang, Z.; Li, L.; Hu, W.; Shuai, Z.; Li, L.; Zhu, D. *Advanced Functional Materials* **2009**, *19*, 272.

[29]   Zhang, L.; Walker, B.; Liu, F.; Colella, N. S.; Mannsfeld, S. C. B.; Watkins, J. J.; Nguyen, T.-Q.; Briseno, A. L. *Journal of Materials Chemistry* **2012**, *22*, 4266.

[30]   Subramanian, S.; Park, S. K.; Parkin, S. R.; Podzorov, V.; Jackson, T. N.; Anthony, J. E. *Journal of the American Chemical Society* **2008**, *130*, 2706.

[31]   Inokuchi, H.; Saito, G.; Wu, P.; Seki, K.; Tang, T. B.; Mori, T.; Imaeda, K.; Enoki, T.; Higuchi, Y.; Inaka, K.; Yasuoka, N. *Chemistry Letters* **1986**, *15*, 1263.

[32]   Troisi, A.; Orlandi, G.; Anthony, J. E. *Chemistry of Materials* **2005**, *17*, 5024.

[33]   Sánchez-Carrera, R. S.; Paramonov, P.; Day, G. M.; Coropceanu, V.; Bredas, J. L. *Journal of the American Chemical Society* **2010**, *132*, 14437.

[34]   Salman, S.; Delgado, M. C. R.; Coropceanu, V.; Brédas, J.-L. *Chemistry of Materials* **2009**, *21*, 3593.

[35]   Li, Y.; Coropceanu, V.; Bredas, J. L. *The Journal of Physical Chemistry Letters* **2012**, *3*, 3325.

CHAPTER 4

IMPACT OF LATTICE VIBRATIONS ON THE CHARGE-TRANSPORT CHARACTERISTICS OF SINGLE-COMPONENT ORGANIC SEMICONDUCTORS

4.1 Introduction

As was mentioned above the electronic and charge-transport properties of organic materials are largely determined by the interplay between the electronic and nuclear dynamics of the molecules, that is by vibronic coupling phenomena [1,2]. Vibrational motions influence the intermolecular electron tunneling probabilities [3-6] and govern a variety of non-equilibrium phenomena such as local heating [7], switching [2], hysteresis, and electronic decoherence [8,9]. Remarkable opportunities for organic electronics would arise from the possibility to control charge transport, and, thus, affect device performance by coherently driving nuclear motions along a pre-selected reaction coordinate trajectory.

Using the formalism that describes interactions between lattice vibrations and charge carriers (introduced in Chapter 1), in the first part of this Chapter, we evaluate the strengths of local and nonlocal electron-vibration couplings in a series of nonlinear acenes (Figure 4.1). We discuss how the extension of the aromatic core influences on the polaron binding energy arising from the local coupling mechanism in these acenes. Since molecules **6** and **9** have the same aromatic core and local electron-phonon coupling is expected to mainly depend on the intra-molecular vibrations, we discuss only molecule **6**

in this context. We then discuss how crystal-packing polymorphism affects nonlocal electron-phonon coupling taking two packing polymorphs of **9**, crystallized at low (**9LT**) and high temperatures (**9HT**), as a case study.
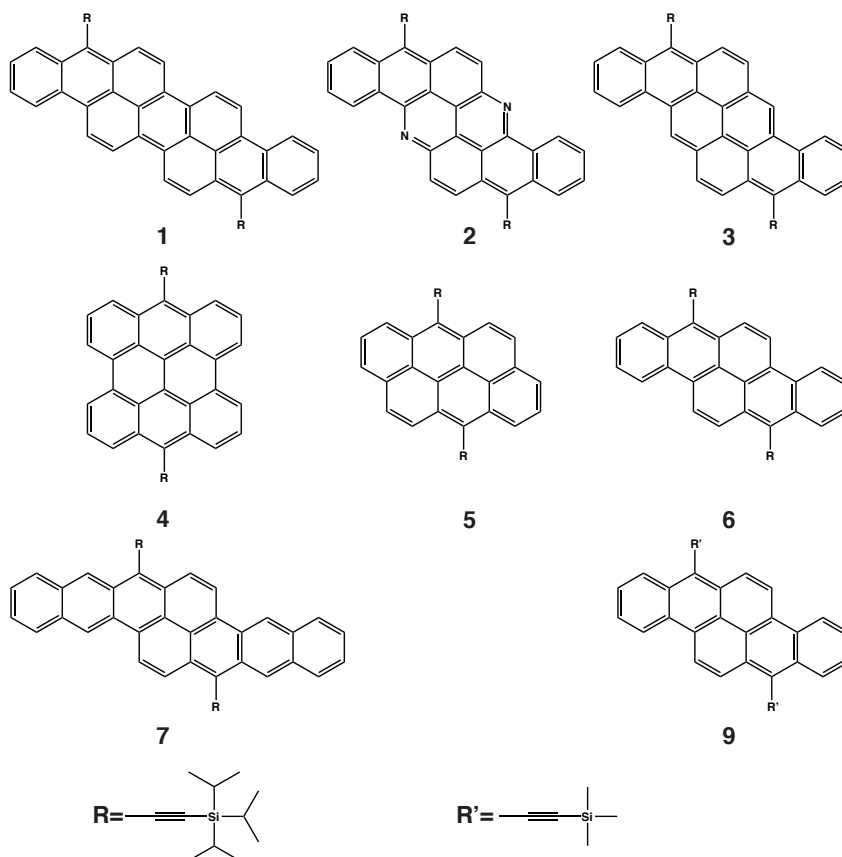
Figure 4.1 Molecular structures of TIPS-functionalized PAHs (**1**-**7**,**9**).

In the second part of this Chapter, we focus on pentacene crystal. By combining device characterization and ultrafast-spectroscopy methods, it was experimentally demonstrated that the performance of a pentacene/C60 bi-layer photoresistor can be controlled by selectively exciting specific vibrational modes of the molecules involved in charge transport. This experimental approach is based on the interferometric extension of the pump-push photocurrent (PPP) technique [10]. The left plot in Figure 4.2 presents the

vibration-associated PPP spectrum covering most of the IR fingerprint frequency range. In the 1150-1700 cm^{-1} region, we observe twelve PPP peaks at frequencies that match well the IR-active vibrational modes of pentacene and C_{60}. The right plot in Figure 4.2 compares the effect of vibrational excitation on the device photoconductivity for different vibrational modes, obtained by normalizing the PPP response to the number of photons absorbed by the vibrational mode.
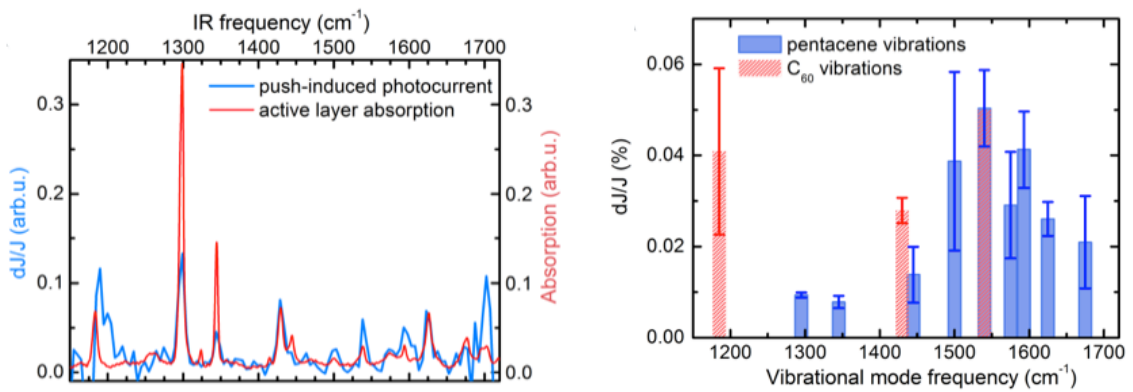
Figure 4.2 Left: The vibrational part of the PPP response. The signal amplitude is normalized to the spectral density of the IR push source. The spectrum is obtained using two different push spectra that are scaled to match the amplitude of the 1430 cm^{-1} mode that is present in both spectra. For comparison, the absorption spectrum of the pentacene/C60 layer is presented in red. Right: The influence of different vibrations on device photocurrent, estimated by normalizing the amplitude of the PPP signal to the absorbed IR light. The error bars are based on the reproducibility of the PPP measurements. Taken from Ref. [11].

Thus, in the second part of the Chapter, we provide a computational model to understand the results obtained using this novel electro-optical technique. In particular, we show that the results from this experimental approach can be rationalized within the phonon-assisted Miller-Abrahams (MA) theory of charge transport [12]. We simulate the IR spectrum of the pentacene thin-film and evaluate nonlocal electron-phonon couplings arising form the IR-active lattice vibrations. This Chapter is based on results published in

The Journal of American Chemical Society [13], *Chemistry – A European Journal* [14], *Chemistry of Materials* [15] and *Nature Communications* [11].

4.2 Computational Methodology

The DFT calculations on nonlinear acenes were performed using the B3LYP functional with the 6-31G basis set. The thermal fluctuations of the transfer integrals of **6** and two polymorphs of **9** were derived by combining molecular dynamics (MD) simulations and quantum-chemical calculations. To prevent artificial symmetry effects, the supercells were initially created via a 3x3x3 replication of the unit cells. The MD simulations were carried out with the Discover module of the Materials Studio package using the COMPASS force field [16]. The system was equilibrated for 150 ps using an Andersen thermostat in the NVT ensemble at 298 K and a time step of 1 fs. After equilibration, a simulation of 150 ps was run and 5000 frames were extracted by taking a snapshot every 30 fs along the trajectory. The transfer integrals for the molecular pairs taken from the MD simulation snapshots were evaluated using a fragment orbital approach in combination with a basis set orthogonalization procedure [17] at the B3LYP/6-31G level.

Geometry optimizations of the crystal structure of the triclinic pentacene polymorph proposed by Campbell [18] were performed at the PBE0/6-31G level of theory. During the optimization, the unit-cell parameters were kept fixed at the experimental values. A uniform 8x6x4 Monkhorst-Pack *k*-point grid was employed. The Γ-point phonons (lattice vibrations) within the harmonic approximation and the IR intensities were obtained via a coupled perturbed Hartree-Fock (CPHF) approach. These calculations were carried out

with the CRYSTAL14 package [19,20]. Since there are two independent molecules in the unit cell of the pentacene crystal, all molecular vibration modes are two-fold (quasi)degenerate. All lattice vibrations in the region of interest can be visualized on the Internet [http://afonari.com/pentacene-vibrations/]. Transfer integrals (electronic couplings) for holes were calculated using a fragment orbital approach based on the unperturbed highest occupied molecular orbitals (HOMOs) of the individual neutral molecules extracted from the optimized crystal geometry [21]. The nonlocal hole-phonon coupling constants (v) come from the modulation of the transfer integrals by lattice vibrations. The coupling constants can be computed by expanding the electronic couplings into Taylor series of the phonon eigenvectors: $t = t_0 + \sum_j v_j Q_j$. Here, t_0 is the electronic coupling at the crystal equilibrium geometry; Q_j is the normal-mode coordinate of mode j; v_j is the linear nonlocal electron-phonon coupling constant. In practice, the coupling constants are calculated by distorting the crystal along all normal-mode coordinates with positive and negative steps and then computing numerically the related derivatives of the transfer integrals for each vibrational mode. All the calculations for the isolated neutral and positively charged molecules were performed at the PBE0/6-31G level of theory using the Gaussian package [22]. The normal modes of the neutral (Q_n) and cation (Q_c) states are related to each other via a multidimensional rotation (Duschinsky) matrix [23]. The Duschinsky matrix was computed with the DUSHIN code [24]. Since it is a common practice to scale calculated frequencies by a constant factor (see also Chapter 7), here, the calculated frequencies for both isolated molecule and crystal were scaled by 0.95 [25].

4.3 Results and discussion

4.3.1 Local electron-vibration interactions in nonlinear acenes

First, we investigate the local electron-vibration and hole-vibration couplings in **1-7**. The strength of these couplings is expressed by the polaron binding energy (E_{pol}). In the context of electron-transfer theory, E_{pol} is roughly equal to half the reorganization energy λ [26], in which the reorganization energy is defined as the sum of 1) intra-molecular contributions – the geometry relaxation energies upon going from the neutral to the charged-state (cation/anion) geometry and vice versa; and 2) intermolecular contributions – energy that arises from the polarization of the surrounding molecules. As the polarization contribution is expected to be small [27], we concentrate here only on the intra-molecular contribution (Table 4.1). Calculations based on both adiabatic energy surfaces and normal-mode approaches [28] yield similar results.

Table 4.1 Polaron binding energies E_{pol} (in meV) in molecules **1-7**.

	1	**2**	**3**	**4**	**5**	**6**	**7**
Hole	77	92	83	68	83	84	64
Electron	104	107	112	91	111	118	88

For all molecules, E_{pol} is lower for holes than for electrons. The lowest value of the polaron binding energy is found in **7** for both hole and electron. The value of 64 meV for the hole E_{pol} is intermediate between the values of 48 and 72 meV derived for pentacene [29] and TIPS-pentacene [30], respectively. The largest value of 92 meV is found in **2**; the substitution of a CH group with a nitrogen atom when going from **3** to **2** results in an increase by about 10 meV in E_{pol}. The electron E_{pol} values range from 88 meV in **7** to 118 meV in **6**. In pentacene [29] and TIPS-pentacene [30] the respective values are 66 and

102 meV. We note that the ratio of the polaron binding energy over the electronic coupling (E_{pol}/t) for holes in all the systems considered here is smaller than in TIPS-pentacene. This leads to the conclusion that the local hole-phonon coupling affects hole mobility in **1-7** to a lesser extent than in TIPS-pentacene. An opposite effect is found for electrons.

4.3.2 Nonlocal electron-vibration interactions in nonlinear acenes

We note that, in addition to local electron-vibration coupling discussed here, there is a second electron-vibration mechanism referred to as the non-local coupling mechanism, which has also a strong impact on charge transport in organic molecular systems [26]. We recall that this mechanism is due to the dependence of the transfer integrals on the distances between adjacent molecules and their relative orientations. We note that a systematic investigation of the nonlocal coupling would require accurate knowledge of the phonon spectra and is beyond the scope of the present work. However, a good estimate of the overall strength of the nonlocal contribution can be derived by considering the variance of the transfer integrals due to thermal fluctuations, $\sigma^2 = \langle (\langle t \rangle - t)^2 \rangle$; here $\langle ... \rangle$ represents the average over the geometrical configurations resulting from thermal motion. We found one molecular dimer with large hole and electron couplings along the slipped-stack direction in **6** and **9LT**. In the case of **9HT**, there are two large couplings (Figure 4.3).
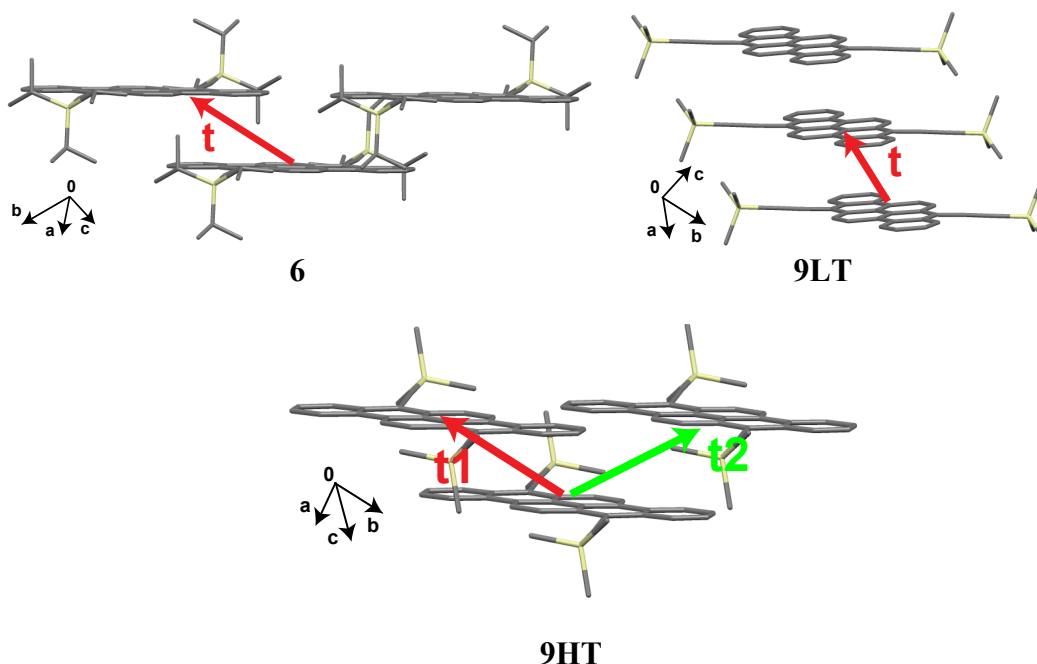
Figure 4.3 Crystal packing of **6** and **9**. Hydrogen atoms are omitted for clarity. The directions of large electronic couplings are marked with arrows.

Using a procedure that combines molecular dynamics simulations and quantum-chemical calculations [31], we computed the probability distribution of the transfer integrals in these crystals (Table 4.2). From this distribution, we then estimated σ and $\langle t \rangle$. We also evaluated the nonlocal hole-phonon (L_h) and electron-phonon (L_e) in the high-temperature limit.

Table 4.2 Values of nonlocal hole-phonon (L_h) and electron-phonon (L_e) [32,33], σ and $\langle t \rangle$ for dimers (all values are in meV). In the high-temperature limit, the nonlocal electron-phonon relaxation energy is defined as: $L = \sigma^2 / 2k_B T, T = 298K$.

	$\langle t_h \rangle$	σ_h	$\sigma_h / \langle t_h \rangle$	L_h	$\langle t_e \rangle$	σ_e	$\sigma_e / \langle t_e \rangle$	L_e
6	-87.2	28.3	0.3	15.6	18.2	35.4	1.94	24.4
9LT	-86.8	33.2	0.4	21.5	7.9	53.0	6.7	54.7
9HT t_1	-77.3	26.0	0.3	13.2	89.2	43.8	0.5	37.4
9HT t_2	-41.4	32.5	0.8	20.6	72.7	23.7	0.3	10.9
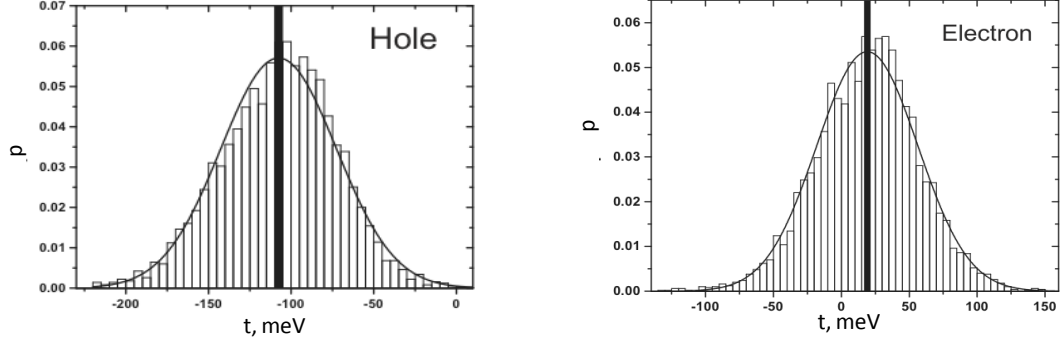
Figure 4.4 Normalized probability distributions of the largest transfer integral for holes and electrons in **6**. The lines represent Gaussian fits and the bold vertical bars correspond to the average transfer integral, $\langle t \rangle$.

For the largest hole coupling, the calculations show that the ratio $\sigma/\langle t \rangle$ is 0.3 for **6** and **9HT** and 0.4 for the **9LT** polymorph. These values are very similar to those obtained for pentacene and its derivatives, suggesting that the non-local coupling in the present systems has a similar impact on the carrier mobility as in other oligoacenes [34]. Also, these values are smaller than unity implying that the formation of self-localized polarons due to nonlocal coupling is not likely [35,36]. If the nonlocal coupling is treated as a perturbation (in the band-like transport regime), then it is possible to evaluate the hole mobility based on the 1D Boltzmann theory. The mobility is computed according to the Boltzmann theory in the relaxation-time approximation [36]:

$$\mu = \frac{\mu_0 t_\omega^3 \hbar\omega}{32\pi L T_\omega^2 I_0(t_\omega/T_\omega)} \times \int_{-1}^{1} \frac{1-x^2}{1+(2c-1)(2x^2-1)} e^{-xt_\omega/T_\omega} \, dx . \tag{4.1}$$

Here, it is assumed that the major contribution to L is arising from the low-energy intermolecular lattice vibrations; thus, we set $\hbar\omega = 50$ cm^{-1}. Also, we define $t_\omega = 2t/\hbar\omega$, $T_\omega = k_B T/\hbar\omega$ and $\mu_0 = ea^2/\hbar$, where t is electronic coupling obtained from dimer calculations, T is temperature, e is the elementary charge, a is the distance between the centers of mass of the monomers, and I_0 is the modified Bessel function of the first kind.

In these calculations, we assumed that the antisymmetric and symmetric electron-phonon couplings are equal, therefore, we also set c = 0.5 [36]. In the case of the **9LT** polymorph, for t_h = 86.8 meV, L_h = 21.5 meV, and d = 6.4 Å, room-temperature (T = 298K) hole mobility is estimated at 5.4 cm^2/Vs. In the case of the **9HT** polymorph, the room-temperature hole mobility along the direction with the largest coupling (t_h = 77.3 meV, L_h = 13.2 meV and d = 6.2 Å) is estimated at 6.8 cm^2/Vs. We note, however, that the applicability of the Boltzmann theory is strictly justified only when $\sigma/\langle t \rangle \ll 1$; transport models that can be applied for intermediate values of $\sigma/\langle t \rangle \sim 1$ still need to be developed in order to obtain more accurate values of the charge-carrier mobilities in these and similar systems. For this reason, we omit calculation of the electron mobilities for these systems, since the ratios of $\sigma/\langle t \rangle$ are around or larger than 1.

4.3.3 Nonlocal electron-vibration interactions in pentacene crystal

The experimental results described above of the current modulation upon an IR excitation of molecular vibrations in the pentacene/C60 photoresistor can be rationalized in the framework of the phonon-assisted Miller-Abrahams (MA) theory [12]. According to this model, carrier hopping from a trapping state to higher-energy (more conducting) states takes place via absorption of a phonon with energy Δ to compensate for the energy difference between the initial and final electronic states; the hopping rate k is defined by the electron-vibrational coupling constant (v) and the occupation number (n_Δ) of the absorbed phonon, *i.e.*, $k \sim v^2 n_\Delta$. In thermal equilibrium, the occupation number of a high-energy molecular vibration is very small, n_Δ = exp($-\Delta/k_B T$). For a comprehensive description of the pump-push photocurrent (PPP) response, the interaction with the IR

photons should be included into the MA model. However, at the conceptual level the effect can be understood by assuming that an IR excitation creates a non-equilibrium population of the molecular vibrational manifold; therefore, an increase in the hopping probability is expected. The mode-selective character of the PPP response is therefore defined by the electron-vibration coupling constants.

To achieve mechanistic insight into the observed phenomena we performed a theoretical analysis of the coupling between the different molecular vibrations and the charge carriers (holes) in pentacene. In molecular systems these couplings can be divided into two types, *i.e.*, local (Holstein-type) and nonlocal (Peierls-type) [37]. The Holstein electron-phonon interaction originates from the modulation of the site energies by the vibrations. Only totally symmetric molecular vibration modes can contribute to this interaction. For centrosymmetric molecules like pentacene, the symmetric modes are not IR-active. It was, however, shown that in one-dimensional (semi)conductors totally symmetric modes can gain IR activity when coupled via Holstein interaction to charge density oscillations or charge transfer states [38]. In the present case the involvement of totally symmetric modes can be excluded based on the combined consideration of the experimental and theoretical data. On the one hand, the calculations indicate that there are no intra-molecular pentacene modes with energies higher than 1600 cm^{-1} or in the range of 1220-1425 cm^{-1} that contribute to the Holstein coupling [28]; on the other hand, however, the experimental data show that at least four modes in these regions contribute to the PPP response. The Peierls-type electron-phonon couplings are associated with the dependence of the transfer integrals on the distances between adjacent molecules and

their relative orientations [37]; for this type of coupling, there are no symmetry restrictions.

Based on previous studies [39], we used a triclinic polymorph [18] to represent the pentacene layer structure in the calculations. Figure 4.5a shows the simulated IR spectra for a single pentacene molecule and for the crystal in comparison to the experimental IR absorption. The agreement between the experimental and calculated vibrational frequencies (with typical discrepancies <10 cm^{-1}) allows the assignment of the vibrational modes observed in the frequency-resolved PPP experiment. The 1300 and 1345 cm^{-1} features in the experimental spectrum are associated (Figure 4.5c) with in-plane ring stretching modes along the short axis of pentacene [40,41], while the IR peaks at 1540 cm^{-1} and 1630 cm^{-1} are associated with molecular deformations along the long axis of pentacene (Figure 4.5d).

The nonlocal hole-vibration couplings are defined as the derivatives of the charge transfer integrals with respect to the vibrational coordinates, $v_i=dt_i/dQ_j$, and can be computed numerically [42,43]. Both the transfer integrals and electron-vibration couplings have been derived in a one-electron approximation. Our results indicate that there are two main transfer integrals contributing to charge transfer in the pentacene crystal: $t_1=75$ meV and $t_2=32$ meV; both are associated with intermolecular interactions along the herringbone directions (Figure 4.5b). The other two transfer integrals oriented along the *a*-axis are substantially smaller and do not demonstrate substantial modulation by IR-active modes.
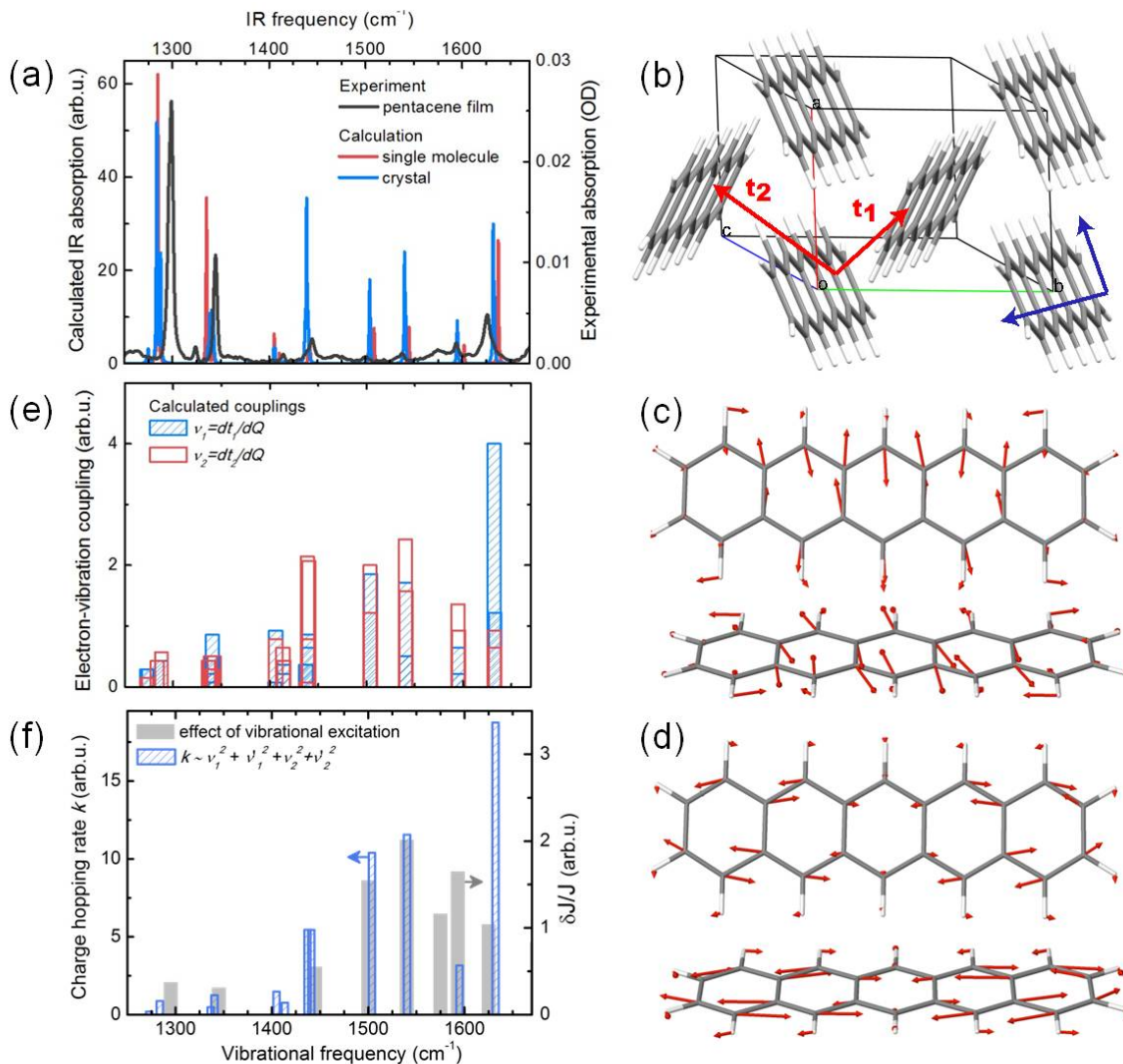
Figure 4.5 (a) Simulated IR spectrum for the pentacene molecule (red) and crystal (blue), superimposed on the experimental spectrum for comparison. (b) Molecular crystal structure and transfer integrals t_i addressed in the calculations. (c,d) Eigendisplacements for the modes with large transition dipoles at 1288 cm^{-1} and 1632 cm^{-1}. (e) Non-local electron-phonon coupling constants for two largest transfer integrals. (f) Calculated vibration-induced hopping rates for the different modes that were addressed experimentally, compared to the experimentally observed effect of vibrational excitation on the photocurrent, dJ/J. Taken from Ref. [11]

Table 4.3 Frequencies, IR intensities, and nonlocal hole-phonon couplings for pentacene.

Crystal				Neutral molecule		Charged molecule	
Freq., cm^{-1}	IR, km/mol	v_1, meV	v_2, meV	Freq., cm^{-1}	IR, km/mol	Freq., cm^{-1}	IR, km/mol
994.90	0.09	0.79	2.86	1113.81	7.96	1116.32	3.92
997.79	28.24	0.00	0.79	1133.71	4.91	1166.38	28.84
1001.41	2.51	0.14	0.21	1163.09	0.26	1176.69	198.32
1110.80	36.33	0.07	0.00	1186.55	3.62	1188.85	2.75
1113.74	16.09	0.07	0.14	1228.96	1.66	1235.58	131.09
1137.16	4.55	0.29	0.43	1268.43	0.01	1273.24	2.23
1138.36	5.14	0.07	0.93	1284.67	24.38	1288.99	41.72
1158.93	5.68	0.07	0.29	1335.15	13.96	1336.43	6.29
1164.37	36.81	0.07	0.07	1342.13	2.51	1380.13	653.83
1187.31	2.96	0.29	0.07	1405.31	2.50	1400.18	839.40
1190.04	41.10	0.07	0.07	1410.59	0.87	1415.26	148.93
1228.30	14.87	0.29	1.14	1440.56	0.86	1438.87	20.08
1230.19	1.28	0.50	1.00	1442.49	1.27	1444.38	6.94
1272.59	1.01	0.29	0.14	1508.64	2.99	1488.77	502.01
1274.71	4.63	0.29	0.14	1544.89	3.08	1530.31	292.10
1283.62	81.01	0.43	0.43	1601.88	1.56	1578.82	3.89
1287.69	36.16	0.43	0.57	1637.32	10.38	1598.20	20.13
1336.47	4.64	0.07	0.43				
1338.68	15.22	0.21	0.50				
1340.40	15.86	0.86	0.29				
1342.41	16.93	0.43	0.50				
1404.86	4.47	0.07	0.00				
1406.01	4.80	0.93	0.79				
1413.53	0.14	0.21	0.64				
1414.51	0.63	0.36	0.43				
1437.36	9.19	0.36	0.07				
1438.79	21.27	0.86	2.14				
1438.95	33.94	0.36	0.79				
1440.53	12.79	0.64	2.07				
1503.93	6.16	1.21	2.00				
1504.28	23.99	1.86	1.21				
1540.27	34.73	1.71	2.43				
1541.25	14.26	0.50	1.57				
1594.79	12.50	0.64	1.36				
1595.31	3.98	0.21	0.93				
1632.15	43.92	4.00	0.93				
1633.17	16.82	1.21	0.64				

The derived coupling constants of the IR-active modes are shown in Figure 4.5e. The couplings in the 1400–1650 cm^{-1} range are about 2 to 5 times larger than in the 1200–1400 cm^{-1} range. To link the variations in coupling and the probability to de-trap a charge with a vibrational excitation, we estimated the rates of vibration-induced charge hopping. In the case of two pathways, the rate is defined within perturbation theory as: $k_i \sim \left(v_{1,i}^2 + v_{2,i}^2 + v'^2_{1,i} + v'^2_{2,i} \right)$, where $v_{j,i}$ and $v'_{j,i}$ correspond to quasi-degenerate molecular vibrations of similar frequencies. Figure 4.5f presents these hopping rates together with the experimental observations. The theoretical results are fully consistent with the experimental data. In particular, they capture well the mode-selective character of the phenomena, with the modes below 1430 cm^{-1} calculated to have a much smaller impact on charge hopping than the higher-frequency ones. Based on the calculations, the intermolecular electronic couplings and charge transport in pentacene crystals are seen to be most sensitive to stretching deformations along the long molecular axis, while the stretching deformations along the short molecular axis are less important.

Table 4.4 Correspondence between the frequencies of the cation and neutral molecule based on the projections of the normal coordinates of the charged molecule onto the neutral-molecule normal coordinates. The largest coefficients in the Duschinsky matrices are also listed.

Cation freq., cm^{-1}	Neutral freq., cm^{-1}	%
1116.32	1113.81	98.8
1166.38	1133.71	73.8
	1163.09	22.3
1176.69	1133.71	21.5
	1163.09	76.7
1188.85	1186.55	98.1
1235.58	1228.96	96.7
1273.24	1268.43	93.8
1288.99	1284.67	95.6
1336.43	1342.13	96.1
1380.13	1335.15	18.5
	1405.31	52
	1544.89	10.1
1400.18	1335.15	68.5
	1410.59	11.5
1415.26	1405.31	26.6
	1410.59	56.8
1438.87	1410.59	88.6
1444.38	1442.49	97.2
1488.77	1508.64	77.9
1530.31	1544.89	77.8
1578.82	1601.88	88.5
	1637.32	10.1
1598.20	1601.88	10.2
	1637.32	88.9

We note that, while the vibrations of charged pentacene may differ from those of the neutral molecules [44], these differences should not be observed in the PPP data. Firstly, the shift in frequency for most individual modes is small [45,46] and, for most modes, below experimental frequency resolution ($\sim$10 cm^{-1}). This conclusion is also supported by DFT calculations (Table 4.3, Table 4.4). Secondly, the minor shifts of the vibrational levels lead to a highly efficient vibrational energy transfer [47] between neutral and charged molecules, which allows the vibrational excitation of neutral pentacene to be delivered to the charge trapping sites. Thirdly, according to Miller-Abrahams formalism, when a carrier hops from a radical to a neutral state, all vibrational modes coupled to these electronic states contribute to the transfer rate [12]. Therefore, it is not surprising that the lattice vibrations, i.e. those of the neutral pentacene, are observed in the detrapping dynamics. We note that this mechanism does not contradict the mode selective nature of the vibronic coupling.

4.4 Conclusions

In this Chapter, we first evaluated the strength of local and nonlocal electron-phonon and hole-phonon couplings in a series of nonlinear acenes. Our calculations show that the local coupling strength (related to E_{pol}) is decreasing with the increase of the conjugated aromatic core, in agreement with previous studies. Based on our calculations, the formation of self-localized polarons due to local and nonlocal coupling is also not likely, suggesting that these nonlinear acenes should exhibit band-like transport.

We also demonstrated that the variation of photoconductivity in a pentacene photoresistor can be related to the rates of phonon-assisted charge hopping within the microscopic Miller-Abrahams model. In agreement with experiment, the theoretical calculations demonstrate that different non-equilibrium geometries and atomic motions have different effects on the charge dynamics. Specifically, our results show that vibrations along the long axis of pentacene molecules lead to a stronger increase of hopping transport via charge de-trapping than vibrations along the short axis. The mode-selective 'vibrational control' of charge dynamics discussed here opens up a plethora of opportunities for basic research, including the development of higher-mobility organic semiconductors, and the utilization of vibronic phenomena for ultrafast switching of organic devices. In addition, the mode-selective and local nature of the experimental PPP method might be particularly useful for the identification of charge-transport mechanisms and pathways in (bio)molecular junctions [48].

4.5 References

[1]   Bredas, J. L.; Street, G. B. *Accounts of Chemical Research* **1985**, *18*, 309.

[2]   Galperin, M.; Ratner, M. A.; Nitzan, A.; Troisi, A. *Science* **2008**, *319*, 1056.

[3]   Asadi, K.; Kronemeijer, A. J.; Cramer, T.; Jan Anton Koster, L.; Blom, P. W. M.; de Leeuw, D. M. *Nature Communications* **2013**, *4*, 1710.

[4]   Eggeman, A. S.; Illig, S.; Troisi, A.; Sirringhaus, H.; Midgley, P. A. *Nature Materials* **2013**, *12*, 1045.

[5]   Lambe, J.; Jaklevic, R. C. *Physical Review* **1968**, *165*, 821.

[6]   Pascual, J. I.; Lorente, N.; Song, Z.; Conrad, H.; Rust, H. P. *Nature* **2003**, *423*, 525.

[7]   Ward, D. R.; Corley, D. A.; Tour, J. M.; Natelson, D. *Nature Nanotechnology* **2011**, *6*, 33.

[8]   Ballmann, S.; Härtle, R.; Coto, P. B.; Elbing, M.; Mayor, M.; Bryce, M. R.; Thoss, M.; Weber, H. B. *Physical Review Letters* **2012**, *109*, 056801.

[9]   Guedon, C. M.; Valkenier, H.; Markussen, T.; Thygesen, K. S.; Hummelen, J. C.; van der Molen, S. J. *Nat Nano* **2012**, *7*, 305.

[10]   Bakulin, A. A.; Rao, A.; Pavelyev, V. G.; van Loosdrecht, P. H. M.; Pshenichnikov, M. S.; Niedzialek, D.; Cornil, J.; Beljonne, D.; Friend, R. H. *Science* **2012**, *335*, 1340.

[11]   Bakulin, A. A.; Lovrinčić, R.; Xi, Y.; Selig, O.; Bakker, H. J.; Rezus, Y. L. A.; Nayak, P. K.; Fonari, A.; Coropceanu, V.; Bredas, J.-L.; Cahen, D. *arXiv:1503.00777* **2015**.

[12]   Miller, A.; Abrahams, E. *Physical Review* **1960**, *120*, 745.

[13]   Zhang, L.; Fonari, A.; Liu, Y.; Hoyt, A.-L. M.; Lee, H.; Granger, D.; Parkin, S.; Russell, T. P.; Anthony, J. E.; Brédas, J.-L.; Coropceanu, V.; Briseno, A. L. *Journal of the American Chemical Society* **2014**, *136*, 9248.

[14]   Zhang, L.; Fonari, A.; Zhang, Y.; Zhao, G.; Coropceanu, V.; Hu, W.; Parkin, S.; Brédas, J.-L.; Briseno, A. L. *Chemistry – A European Journal* **2013**, *19*, 17907.

[15]   Stevens, L. A.; Goetz, K. P.; Fonari, A.; Shu, Y.; Williamson, R. M.; Brédas, J.-L.; Coropceanu, V.; Jurchescu, O. D.; Collis, G. E. *Chemistry of Materials* **2015**, *27*, 112.

[16]   Bunte, S. W.; Sun, H. *Journal of Physical Chemistry B* **2000**, *104*, 2477.

[17]   Valeev, E. F.; Coropceanu, V.; da Silva Filho, D. A.; Salman, S.; Bredas, J. L. *Journal of the American Chemical Society* **2006**, *128*, 9882.

[18]   Campbell, R. B.; Robertson, J. M.; Trotter, J. *Acta Crystallographica* **1962**, *15*, 289.

[19]   Maschio, L.; Kirtman, B.; Orlando, R.; Rèrat, M. *The Journal of Chemical Physics* **2012**, *137*.

[20]   Dovesi, R.; Orlando, R.; Erba, A.; Zicovich-Wilson, C. M.; Civalleri, B.; Casassa, S.; Maschio, L.; Ferrabone, M.; De La Pierre, M.; D'Arco, P.; Noël, Y.; Causà, M.; Rérat, M.; Kirtman, B. *International Journal of Quantum Chemistry* **2014**, *114*, 1287.

[21]   Valeev, E. F.; Coropceanu, V.; da Silva Filho, D. A.; Salman, S.; Brédas, J.-L. *Journal of the American Chemical Society* **2006**, *128*, 9882.

[22]   Frisch, M. J.; Trucks, G. W.; Schlegel, H. B.; Scuseria, G. E.; Robb, M. A.; Cheeseman, J. R.; Scalmani, G.; Barone, V.; Mennucci, B.; Petersson, G. A.; Nakatsuji, H.; Caricato, M.; Li, X.; Hratchian, H. P.; Izmaylov, A. F.; Bloino, J.; Zheng, G.; Sonnenberg, J. L.; Hada, M.; Ehara, M.; Toyota, K.; Fukuda, R.; Hasegawa, J.; Ishida, M.; Nakajima, T.; Honda, Y.; Kitao, O.; Nakai, H.; Vreven, T.; Montgomery Jr., J. A.; Peralta, J. E.; Ogliaro, F.; Bearpark, M. J.; Heyd, J.; Brothers, E. N.; Kudin, K. N.; Staroverov, V. N.; Kobayashi, R.; Normand, J.; Raghavachari, K.; Rendell, A. P.; Burant, J. C.; Iyengar, S. S.; Tomasi, J.; Cossi, M.; Rega, N.; Millam, N. J.; Klene, M.; Knox, J. E.; Cross, J. B.; Bakken, V.; Adamo, C.; Jaramillo, J.; Gomperts, R.; Stratmann, R. E.; Yazyev, O.; Austin, A. J.; Cammi, R.; Pomelli, C.; Ochterski, J. W.; Martin, R. L.; Morokuma, K.; Zakrzewski, V. G.; Voth, G. A.; Salvador, P.; Dannenberg, J. J.;

Dapprich, S.; Daniels, A. D.; Farkas, Ö.; Foresman, J. B.; Ortiz, J. V.; Cioslowski, J.; Fox, D. J.; Gaussian, Inc.: Wallingford, CT, USA, 2009.

[23]   Duschinsky, F. *URSS Acta Physicochim* **1937**, *7*, 551.

[24]   Reimers, J. R. *The Journal of Chemical Physics* **2001**, *115*, 9103.

[25]   Langhoff, S. R. *The Journal of Physical Chemistry* **1996**, *100*, 2819.

[26]   Coropceanu, V.; Cornil, J.; da Silva Filho, D. A.; Olivier, Y.; Silbey, R.; Bredas, J. L. *Chemical Reviews* **2007**, *107*, 926.

[27]   Norton, J. E.; Brédas, J.-L. *Journal of the American Chemical Society* **2008**, *130*, 12377.

[28]   Malagoli, M.; Coropceanu, V.; da Silva Filho, D. A.; Brédas, J. L. *The Journal of Chemical Physics* **2004**, *120*, 7490.

[29]   Gruhn, N. E.; da Silva Filho, D. A.; Bill, T. G.; Malagoli, M.; Coropceanu, V.; Kahn, A.; Brédas, J.-L. *Journal of the American Chemical Society* **2002**, *124*, 7918.

[30]   Li, C.-H.; Huang, C.-H.; Kuo, M.-Y. *Physical Chemistry Chemical Physics* **2011**, *13*, 11148.

[31]   Delgado, M. C. R.; Pigg, K. R.; da Silva Filho, D. A.; Gruhn, N. E.; Sakamoto, Y.; Suzuki, T.; Osuna, R. M.; Casado, J.; Hernández, V.; Navarrete, J. T. L.; Martinelli, N. G.; Cornil, J.; Sánchez-Carrera, R. S.; Coropceanu, V.; Brédas, J.-L. *Journal of the American Chemical Society* **2009**, *131*, 1502.

[32]   Sánchez-Carrera, R. S.; Paramonov, P.; Day, G. M.; Coropceanu, V.; Bredas, J. L. *Journal of the American Chemical Society* **2010**, *132*, 14437.

[33]   Coropceanu, V.; Sánchez-Carrera, R. S.; Paramonov, P.; Day, G. M.; Brédas, J.-L. *Journal of Physical Chemistry C* **2009**, *113*, 4679.

[34]   Troisi, A.; Orlandi, G.; Anthony, J. E. *Chemistry of Materials* **2005**, *17*, 5024.

[35]   Fratini, S.; Ciuchi, S. *Physical Review Letters* **2009**, *103*, 266601.

[36]   Li, Y.; Yi, Y.; Coropceanu, V.; Bredas, J. L. *Physical Review B: Condensed Matter* **2012**, *85*, 245201.

[37]   Bredas, J. L.; Calbert, J. P.; da Silva Filho, D. A.; Cornil, J. *Proceedings of the National Academy of Sciences* **2002**, *99*, 5804.

[38]   Rice, M. J. *Physical Review Letters* **1976**, *37*, 36.

[39]   Bouchoms, I. P. M.; Schoonveld, W. A.; Vrijmoeth, J.; Klapwijk, T. M. *Synthetic Metals* **1999**, *104*, 175.

[40]   Hosoi, Y.; Okamura, K.; Kimura, Y.; Ishii, H.; Niwano, M. *Applied Surface Science* **2005**, *244*, 607.

[41]   Salzmann, I.; Opitz, R.; Rogaschewski, S.; Rabe, J. P.; Koch, N.; Nickel, B. *Physical Review B* **2007**, *75*, 174108.

[42]   Coropceanu, V.; Sánchez-Carrera, R. S.; Paramonov, P.; Day, G. M.; Brédas, J.-L. *The Journal of Physical Chemistry C* **2009**, *113*, 4679.

[43]   Sánchez-Carrera, R. S.; Paramonov, P.; Day, G. M.; Coropceanu, V.; Brédas, J.-L. *Journal of the American Chemical Society* **2010**, *132*, 14437.

[44]   Čápek, V.; Silinsh, E. A. *Chemical Physics* **1995**, *200*, 309.

[45]   Brinkmann, M.; Videva, V. S.; Bieber, A.; André, J. J.; Turek, P.; Zuppiroli, L.; Bugnon, P.; Schaer, M.; Nuesch, F.; Humphry-Baker, R. *The Journal of Physical Chemistry A* **2004**, *108*, 8170.

[46]   Cazayous, M.; Sacuto, A.; Horowitz, G.; Lang, P.; Zimmers, A.; Lobo, R. P. S. M. *Physical Review B* **2004**, *70*, 081309.

[47]   Woutersen, S.; Bakker, H. J. *Nature* **1999**, *402*, 507.

[48]	Giese, B.; Eckhardt, S.; Lauz, M. In *Encyclopedia of Radicals in Chemistry, Biology and Materials*; John Wiley & Sons, Ltd: 2012.

CHAPTER 5

IMPACT OF LATTICE VIBRATIONS ON SINGLET FISSION IN SINGLE-COMPONENT ORGANIC SEMICONDUCTORS

5.1 Introduction

The performance of organic photovoltaic devices is integrally connected to the number of charge carriers, *i.e.* holes and electrons, which can be photo-created. The device efficiency could potentially be improved in the case of singlet fission (SF), whereby a singlet excited state forms two triplet excitations of lower energy on neighboring chromophores [1,2]. SF offers the possibility of overcoming the theoretical Shockley-Queisser limit from ~31% to greater than 45% [3].

For SF to occur, the energy of the first singlet excited state should be approximately equal or slightly larger than twice the energy of the lowest triplet excited state ($E(S_1) \approx 2E(T_1)$) [4,5]. For example, in the case of pentacene, SF is energetically allowed [6], whereas in tetracene, the triplet state is positioned higher in energy than that of half-of-singlet energy, making SF process endergonic by ~0.2 eV [7]. These differences lead to two very different experimental rates for SF in crystalline pentacene (~100 fs) [8-12] and in crystalline tetracene (~90 ps) [13,14]. Although previous studies from Greyson *et al.* [15] and Yost *et al.* [16] have suggested that the energy-level alignment is an important component of SF, similarly to the charge-transport process, not only energy-level alignment but also state couplings play an important role in the SF mechanism.

There is an ongoing debate whether the first singlet bright state in oligoacene crystals is localized (*i.e.*, of Frenkel type) [17], has a charge-transfer nature [18,19], or is a mixture of both [20,21]. Depending on the nature of the singlet excitation manifold, the SF mechanism can be described by: either a direct two-electron transfer starting from one monomer with a localized singlet excitation and the other monomer in the ground state ($|S_1 S_0\rangle$) to go to two correlated-triplet states on each monomer ($|T_1 T_1\rangle$); or starting from a charge transfer (CT) state ($|D^+ A^-\rangle$) to the final $|T_1 T_1\rangle$ state. In both cases, SF occurs in one step.

Recently, several studies have focused on understanding and describing these pathways at a molecular level and a simple dimer model has been the center of such investigations [22-25]. The direct SF mechanism was shown to be related to the two-electron Coulomb integral [26]:

$$t_{2e} = \sqrt{\frac{3}{2}} \left(\left\langle L_i L_j \middle| \frac{e^2}{r} \middle| H_j L_i \right\rangle - \left\langle H_i H_j \middle| \frac{e^2}{r} \middle| L_j H_i \right\rangle \right), \qquad (5.1)$$

where H_i and L_j denote the frontier orbitals (HOMO and LUMO) of monomers i and j. In the case of the CT singlet excitation, the SF rate is related to the one-electron transfer integrals [2]:

$$t_{CT} = \left(\left\langle H_i \middle| F \middle| L_j \right\rangle \right), \qquad (5.2)$$

where F represents a Fock matrix built using localized frontier molecular orbitals of monomers and dimer [27]. In the case of a symmetric dimer $t_{CT} = t_{HL} = t_{LH}$. Previous studies have shown that the absolute values of t_{2e} couplings are about two orders of magnitude smaller than the one-electron coupling terms [28-30]. Classical Marcus equation [31] or related quantum-mechanical Bixon-Jortner (BJ) equations [32] can be

applied to evaluate the rates for the direct and CT pathways. Both Marcus and BJ equations have rates that quadratically depend on the electronic coupling, *i.e.*, $k \sim t^2$. Recently, Van Voorhis and collaborators obtained a good agreement between calculated and experimental fission rates by applying the BJ rate equation in the context of organic solar cells based on tetracene and pentacene derivatives [16,33].

It was shown previously that both direct and CT mechanisms are strongly affected by the molecular geometries and orientations in the crystal [1,28]. For example, perfectly stacked planar aromatic molecules (such as oligoacene and perylenediimide derivatives) have both t_{2e} and t_{CT} couplings close to zero. These become nonzero once the dimer is in a slipped-stacked configuration, which suggests that these configurations are much more prone to fast SF than perfectly cofacial arrangements [2,28]. However, the influence of crystal vibrations (phonons) on the SF characteristics is not well understood. Several attempts were made to describe intermolecular vibrations by using empirical translations and rotations of a monomer in a dimer-model calculation for tetracene and pentacene systems, which attributed the ultrafast transition from the first excited singlet state (S$_1$) to a multiexciton state ($|T_1 T_1\rangle$) in pentacene and tetracene as a result of conical intersections [22,34]; however, the generation and diagonalization of the dynamical matrix that is required to obtain vibrations (phonons) in a periodic system was not performed. Recent pulse-shaping experiments that selectively excite an electronic transition and several low-frequency phonons simultaneously in a polycrystalline tetracene film, demonstrated a 20% quantum yield enhancement for the triplet formation. These results indicate that

several low-energy Raman-active phonons (74 cm^{-1}, 123 cm^{-1} and 148 cm^{-1}) could facilitate SF in tetracene single crystals [35].

In this Chapter, we first describe the relation between t_{2e} and t_{CT} couplings using a tetracene dimer model. Then, we use periodic-boundary calculations to simulate the IR and Raman spectra of the tetracene single crystal. We describe phonons that correspond to peaks in the experimental IR and Raman spectra. Afterwards, we assess the importance of the IR and Raman-active modes on the t_{2e} and t_{CT} couplings in the context of SF. We show that modes with a particular displacement pattern could strongly facilitate the SF process. Finally, we evaluate the magnitude of the effect of thermal vibrations on the state couplings, in order to facilitate the discussion of how vibrations affect the SF process in non-ideal crystalline dimers.
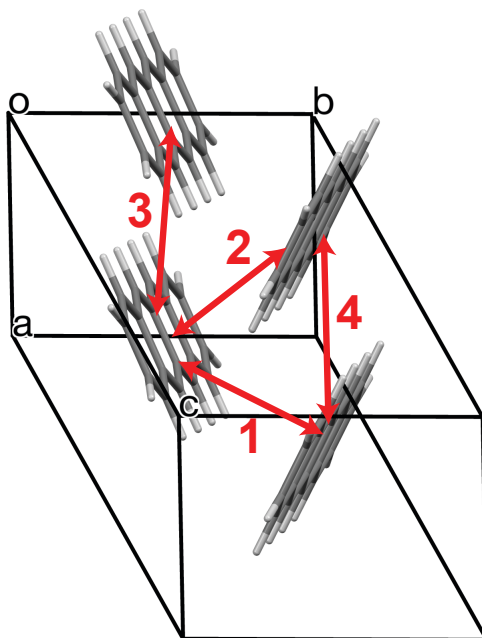
Figure 5.1 Molecular structure and molecular packing in the tetracene crystal. The largest state couplings are shown with arrows.

5.2 Computational methodology

The geometry of the tetracene crystal [36] was optimized by keeping the unit-cell parameters fixed at their experimental values. The Brillouin zone was sampled using a Γ-centered uniform k-point 8x6x4 grid. Structural relaxation, phonons at the Γ-point, and IR and Raman spectra were calculated at the B3LYP/6-31G level using the CRYSTAL14 package [37-39]. State couplings were evaluated at the B3LYP/6-31G level using the developmental version of the NWChem package [40]. The thermal fluctuations of the couplings were derived by combining molecular dynamics (MD) simulations and quantum-chemical calculations. To prevent artificial symmetry effects, supercells were initially created via a 6x6x6 replication of the unit cells. The MD simulations were carried out with GROMACS 4.5.4 [41,42], using the OPLS-AA force field [43]. The system was equilibrated for 2000 ps using a Nose-Hoover thermostat and Parrinello-Rahman barostat in the NPT ensemble at 298 K and with a time step of 0.5 fs. After equilibration, a simulation of 150 ps was run and 3000 frames were extracted by taking a snapshot every 30 fs along the trajectory. The average density of the crystal obtained from the MD simulations is ~1.32 g/cm^3, very close to the density reported from single-crystal X-ray diffraction experiment [36]. However, the fluctuations range from 1.29 to 1.35 g/cm^3 due to the thermal vibrations of the supercell, of the order of ~0.2 Å along the a-axis and 0.4 Å along the c-axis (Figure 5.1). State couplings for the molecular pairs taken from the MD simulation snapshots were evaluated at the B3LYP/6-31G level.

5.3 Results and discussion

We first discuss the state couplings (t_{2e}, t_{CT}) in a static picture. For completeness, we also examine the hole (t_{HH}) and electron (t_{LL}) couplings, which are important for charge transport [44]. Tetracene has two molecules in the asymmetric unit of its unit cell, both sitting on the inversion centers; thus, there are four non-equivalent couplings whose values are listed in Table 5.1. The values for hole and electron couplings reported here are in good agreement with those previously computed for tetracene [45]. We note significant hole and electron couplings along with large t_{2e} and t_{CT} couplings along the herringbone direction (pair 2). Conversely, another dimer in the herringbone configuration (pair 1) has a t_{2e} value of 0.044 meV, which is four times smaller than for pair 2. The transfer integrals are also slightly decreased compared to pair 2; this suggests that a connection exists between one-electron and two-electron electronic couplings. If it is assumed that the character of the S_1 excitation in the tetracene crystal has an equal mixture of localized and CT character, than the resulting coupling would be equal to the average between the two couplings, *ca.* 32 meV; this is in good agreement with the coupling estimated by Van Voorhis and collaborators, 20.7 meV, which resulted in a fission rate of 188 ps^{-1}, to be compared to an experimentally measured rate of 91 ps^{-1} [16].

In order to understand the effect of geometry changes on the SF characteristics, we introduce a model system based on a tetracene co-facial dimer. The progression of the hole and electron couplings of a dimer with the slip of one monomer along the long axis was thoroughly investigated previously [46]. Here, we can add that in the case of linear

oligoacenes only the values of t_{HH} and t_{LL} vary, whereas the t_{2e} and t_{CT} couplings are zero at all times for a long-axis displacement. In the case of a monomer displacement along the short axis, the picture is more interesting. For the sake of simplicity, we only discuss the absolute values of the couplings. We start with the perfectly co-facial configuration; in this case, t_{HH} and t_{LL} have their largest values. Both state couplings, t_{2e} and t_{CT}, are zero [1]. Once the displacement is applied, t_{HH} and t_{LL} start to decay; the hole coupling has two peaks at 0 and 3.2 Å, whereas the electron coupling slowly decays along the whole slip. Similarly, the t_{2e} and t_{CT} couplings have two peaks at 0.8 Å and 3.2 Å. From a 3.2-Å slip onward, all quantities are monotonically decaying. It can be seen that the t_{2e} coupling is decaying much faster compared to the t_{CT} coupling. This strong geometry dependence of t_{2e} was previously noted from model calculations on the perylenediimide (PDI) dimer [28]. These results suggest that the rate of the direct triplet formation is much more affected by the atomic motion compared to the indirect pathway. Model calculations of the tetracene dimer slipped along the short axis were also performed using a correlated restricted-active space approach [47]. The main difference is a much weaker geometry dependence of the non-adiabatic coupling compared to t_{2e}. A thorough comparison of correlated *vs.* adiabatic quantities that define SF is currently under way. It has been noted, that besides the slip-stack arrangement, translation motion that affects the distance between monomers in the herringbone configuration can be also favorable for SF [22,34].

Table 5.1 Largest couplings found in the tetracene crystal. All values are in meV.

pair	t_{HH}	t_{LL}	t_{HL}	t_{LH}	t_{CT}	t_{2e}
1	21.17	80.16	60.28	38.42	49.35	0.044
2	77.60	81.79	61.38	63.31	62.35	0.184
3	17.62	41.00	31.21	31.21	31.21	0.016
4	3.58	14.79	5.36	5.36	5.36	0.001
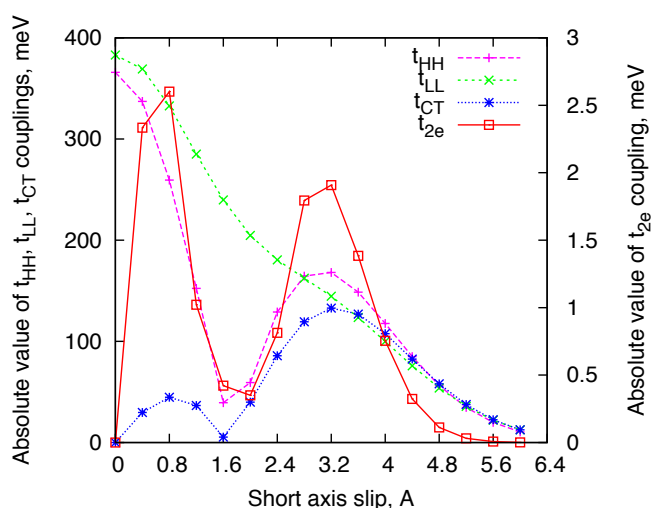
Figure 5.2 Absolute values of the electronic couplings and two-electron terms for a perfectly co-facial tetracene dimer separated by 3.5 Å and displaced in steps of 0.4 Å along the short molecular axis.

The calculated and experimental Raman spectra of the tetracene single crystal are plotted in Figure 5.3. We found six Raman-active phonons in the low-frequency region (0–150 cm^{-1}). There is good agreement between the calculated and experimental spectra, which allows the assignment of the computed phonons to the corresponding measured peaks in the tetracene single crystal (Table 5.2) [48]. The highest intensity peak obtained at 118 cm^{-1} is in excellent agreement with experiment. The shoulder at 130 cm^{-1} is related to the calculated peak at 138 cm^{-1}. The calculated phonon at 98 cm^{-1} is assigned to a weak

experimental peak at 93 cm^{-1}. The next two vibrations with significant Raman intensities at 69 cm^{-1} and 43 cm^{-1} are both shifted by less than ten wavenumbers compared to experiment. Finally, the shoulder at 51 cm^{-1} is also obtained in calculations. Our calculations also agree well with the Raman spectrum of a tetracene thin film obtained from ultrafast optical measurements (Table 5.2) [35]. In terms of relative intensities, both calculated and experimental spectra are in good agreement, with only two phonons at 43 cm^{-1} and 51 cm^{-1} having smaller intensities compared to the intensities of their experimental counterparts. Phonons in the 0–150 cm^{-1} range have a primarily inter-molecular character as confirmed here by considering their eigenvectors (Figure 5.4); this is in agreement with previous experimental assignments [48].

Table 5.2 Calculated and experimentally measured low frequency Raman-active phonons (cm^{-1}), calculated Raman intensities (arbitrary units), and nonlocal phonon coupling constants (meV).

Freq. calc.	Freq. exp. [a]	Freq. exp. [b]	Raman int. calc.	v_{CT}	v_{2e}
43	49	-	3.0	1.54	0.007
51	51	-	1.0	2.79	0.004
69	60	58	8.6	1.16	0.005
98	93	-	2.2	1.86	0.004
118	118	123	21.8	3.40	0.016
138	130	130	16.8	6.33	0.042

[a] Raman intensity measurement from tetracene single crystal [48]; [b] Raman intensity obtained from a Fourier transform of the negative change in transmission, measured on the tetracene thin film [35].

We also simulated the IR spectrum of the tetracene crystal in order to compare our results with the experimentally measured terahertz (THz) absorption spectrum [49]. The results of our calculations also agree well with the experimental IR spectrum of the tetracene crystal (Table 5.3). As can be seen from Figure 3, there are three sharp peaks in the

experimental spectrum at 74, 105, and 165 cm^{-1}, related to three calculated modes at 78, 112, and 166 cm^{-1}. Peaks and 74 cm^{-1} and 165 cm^{-1} have shoulders at 67 cm^{-1} and 171 cm^{-1}, respectively. From calculations, these shoulders correspond to modes with frequencies of 68 cm^{-1} and 173 cm^{-1}, respectively. There is a weak peak at 147 cm^{-1} in the experimental spectrum, which corresponds to the calculated 146 cm^{-1} mode. We omit discussion on how simulated and experimental intensities compare, since the latter have not been normalized to a horizontal baseline.
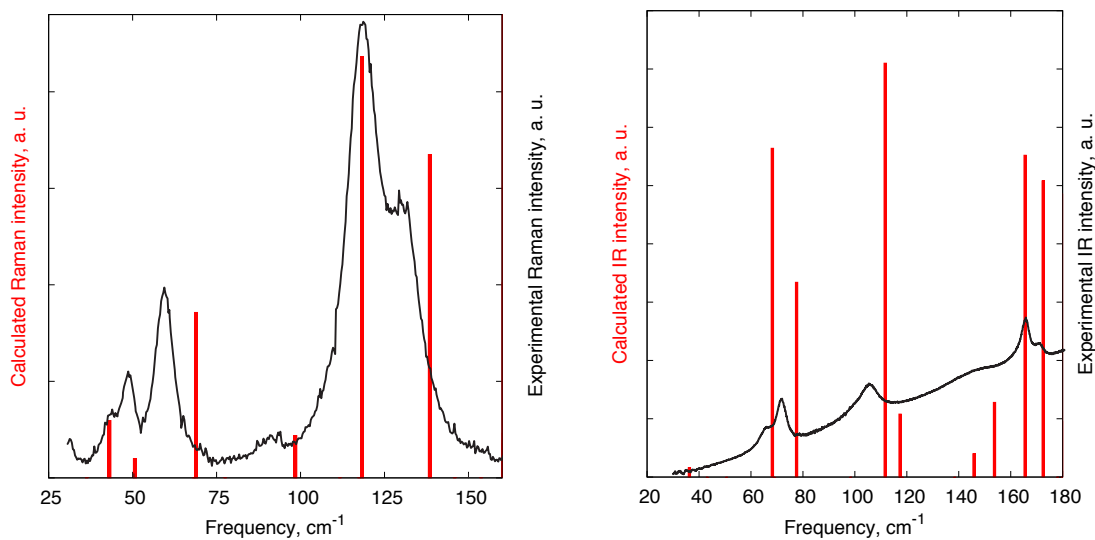
Figure 5.3 Calculated (bars) and experimental (solid lines) Raman (left) and IR (right) spectra of the tetracene single crystal.

Table 5.3 Calculated and experimentally measured low frequency IR-active phonons (cm^{-1}), calculated IR intensities (arbitrary units), and nonlocal phonon couplings (meV).

Freq. calc.	Freq. exp. [a]	IR int. calc.	v_{CT}	v_{2e}
36	-	0.1	2.53	0.017
68	67	2.8	1.51	0.013
78	74	1.7	0.99	0.010
112	105	3.6	7.53	0.035
117	-	0.5	9.41	0.060
146	147	0.2	0.46	0.009
154	-	0.6	2.62	0.015
166	165	2.8	0.21	0.018
173	171	2.5	4.15	0.019

[a] THz absorption spectrum measured for a tetracene single crystal [49].

112 cm^{-1} (IR) 117 cm^{-1} (IR)

118 cm^{-1} (Raman) 138 cm^{-1} (Raman)
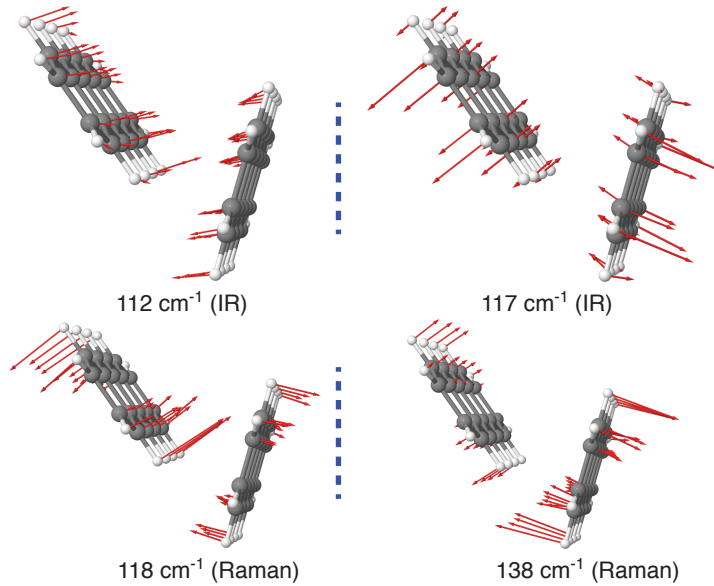
Figure 5.4 Eigenvectors of the low-energy intermolecular IR and Raman-active phonons.

In order to quantify the effect that crystal vibrations have on the modulation of the SF characteristics, we evaluated the nonlocal phonon coupling constants (v). Similarly to our previous studies on oligoacenes [45,50], we evaluate the nonlocal phonon coupling constant as the derivative of coupling for a molecular pair i over a vibrational mode j, for both t_{2e} and t_{CT} couplings:

$$v_{i,2e}^{j} = \frac{\partial t_{i,2e}}{\partial Q_j} \qquad (5.3a) \qquad \qquad v_{i,2e}^{j} = \frac{\partial t_{i,CT}}{\partial Q_j}, \qquad (5.3b)$$

where the derivatives are computed numerically. Since fission is thought to be a local process (unlike charge transport) [51], here we focus only on the pair with the largest state couplings, pair 2, and the subscript i is dropped. First, we discuss the coupling constants of Raman-active phonons. As shown in Figure 5.5 and Table 5.2, the largest v_{2e} and v_{CT} couplings occur for the 118 cm^{-1} and 138 cm^{-1} vibrations. Their eigenvectors are similar and are described by tilting of the molecules, which results in an increased π-stack overlap (Figure 5.4). We note that if a large enough displacement is applied to a herringbone tetracene dimer (this corresponds to an optical or thermal excitation of a phonon) along these two modes, the resulting geometry will be similar to the one obtained from a slip along the short axis (Figure 5.2) at *ca.* the position of the second peak (3.2 Å). In a recent study on a pentacene dimer using correlated methods, it was shown that a slipped-stack conformation obtained when starting from a herringbone configuration of a dimer is favorable for the SF process [34]. A slipped-stack conformation has also been found advantageous for SF in the thin-film of 1,3-biphenylisobenzofuran [2,12]. Our calculations are thus in agreement with ultrafast transient absorption experiments on tetracene thin films, which suggested that several

low-frequency phonons (74 cm^{-1}, 123 cm^{-1} and 148 cm^{-1}) are facilitating the SF process [35].

Besides Raman-active modes, several IR-active modes also strongly modulate the state couplings. The largest v_{2e} and v_{CT} couplings occur for the 112 cm^{-1} and 117 cm^{-1} vibrations (Figure 5.5, Table 5.3). The eigenvector of the vibration at 112 cm^{-1} can be described by a decrease in distance between two herringbone molecules. Similarly, the eigenvector of the 117 cm^{-1} mode is described by a decrease of the distance between the central rings of the tetracene monomers. Our results are in agreement with previous theoretical studies on tetracene and pentacene herringbone dimers, which also suggested that a decrease in the herringbone distance facilitates SF [22,34].
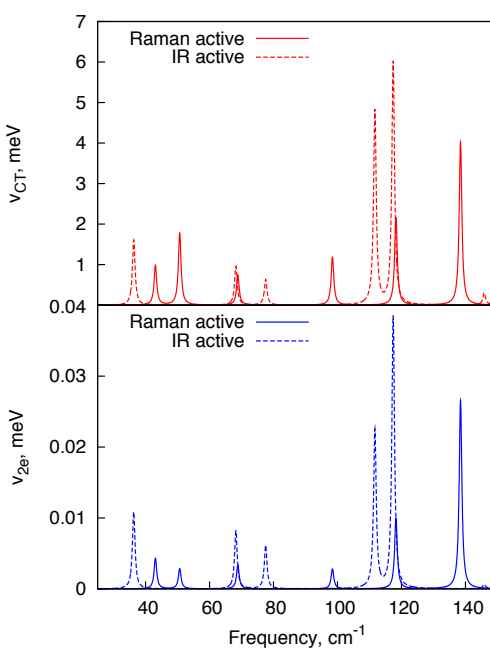
Figure 5.5 Phonon couplings in molecular pair 2 due to the low-energy lattice vibrations in the tetracene crystal. Lorentzian broadening of 5 cm^{-1} was applied.

In order to estimate the strength of the thermal disorder of the SF characteristics at room temperature in the tetracene crystal, following our previous work, we evaluated the nonlocal phonon couplings (L) and thermal fluctuations in the high-temperature limit (σ) of state couplings [45,50]:

$$L = \sum_j \frac{v_j^2}{2\hbar\omega_j} \qquad (5.4a) \qquad\qquad \sigma = \sqrt{2Lk_BT}, \hbar\omega \ll k_BT. \qquad (5.4b)$$

Since it was previously reported that only low-frequency phonons (up to 200 cm^{-1}) contribute to the nonlocal coupling (L) in tetracene and pentacene crystals [45,52], here, we are considering all crystalline vibrations up to 331 cm^{-1}. In terms of charge transport, in the high-temperature limit, the σ/t ratio is an indicator of the disorder in the system. Values of this ratio smaller than one ($\frac{\sigma}{t} \ll 1$) suggest that a band-transport regime (delocalized charge carriers) is valid [53]. For both holes and electrons, the σ/t ratio is around 0.3, in good agreement with previous results for the tetracene crystal [45]. This ratio for the t_{CT} coupling is slightly larger, around 0.4, but remains significantly lower than 1.0. For the t_{2e} coupling, the ratio σ_{2e}/t_{2e}, is around 1.2, suggesting that a phonon-assisted SF process is strongly affected by disorder at high temperature. This is in agreement with our earlier discussion pointing to a much stronger geometry dependence of the direct SF mechanism compared to the mediated pathway.

Another way to estimate the effect of the thermal molecular motions in the crystal on the modulation of the SF microscopic characteristics at room temperature is to compute the coupling distributions via a combination of molecular dynamics simulations and quantum-chemical calculations of the transfer integrals (Figure 5.6). From these distributions, we can estimate the variance of the electronic couplings due to thermal

fluctuations, $\sigma^2 = \langle (\langle t \rangle - t)^2 \rangle$; here $\langle ... \rangle$ represents the average over the geometrical configurations resulting from thermal motion. Consistent with the results obtained from the crystalline vibrations, the ratio σ/t for holes and electrons is ~0.3. This ratio for the CT terms is slightly larger (~0.4). The σ/t ratio for the two-electron term is around 10, suggesting an even stronger disorder influence compared to the values obtained from the lattice normal modes (quantum picture).
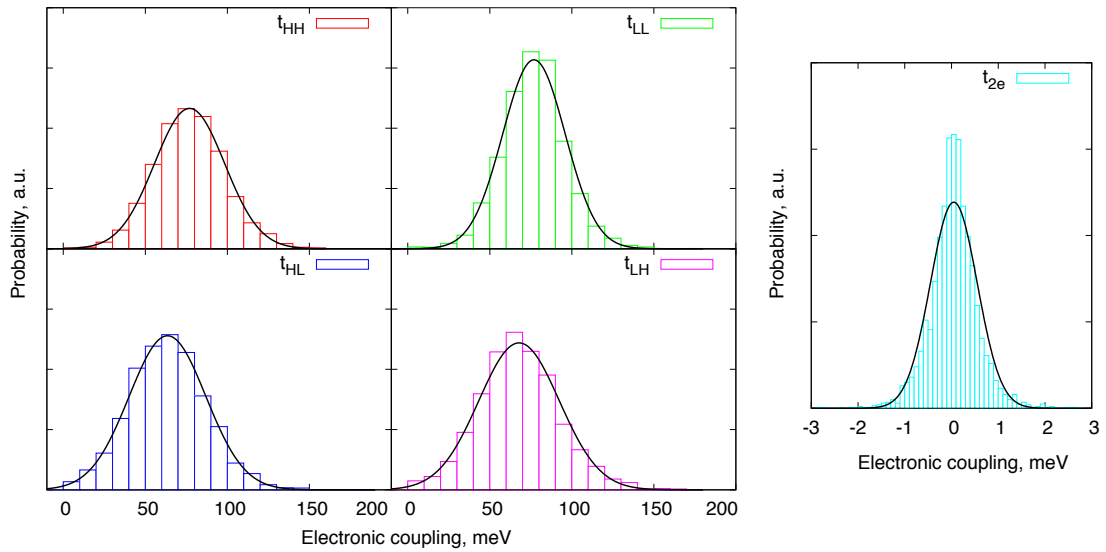
Figure 5.6 Normalized probability distributions of the couplings for pair 2.

Table 5.4 Coupling distributions and standard deviations for pair 2.

Coupling	$\langle t \rangle$, meV	σ, meV	$\sigma/\langle t \rangle$
t_{HH}	76.99	21.41	0.28
t_{LL}	76.92	19.08	0.25
t_{HL}	63.52	23.40	0.34
t_{LH}	67.82	24.53	0.36
t_{2e}	0.050	0.502	10.04

5.4 Conclusions

We first employed a Coupled Perturbed Hartree-Fock approach to simulate the IR and Raman spectra of the tetracene crystal in the low-frequency region. Good agreement between the calculated and experimental spectra allowed us to assign the calculated normal modes to peaks in the experimental spectra for both Raman and IR. We depicted several lattice vibrations that strongly modulate the state couplings related to singlet fission. Our results are in agreement with the experimental conclusions; in particular, we showed that Raman active modes at 74 cm^{-1} and 123 cm^{-1} facilitate singlet fission. These modes are described by an increased π-stack overlap between herringbone molecules. We also found two IR-active modes at 112 cm^{-1} and 117 cm^{-1} that strongly modulate both the CT and direct two-electron couplings. These correspond to a decrease in the distance between the centers of masses of two herringbone molecules, in agreement with literature results. In order to understand the impact of the lattice vibrations on the state couplings at a finite temperature, we also evaluated the variation of the state couplings using molecular dynamics simulations. Our results suggest that the CT coupling is much less modulated compared to the direct two-electron coupling.

5.5 References:

[1]   Smith, M. B.; Michl, J. *Annual Review of Physical Chemistry* **2013**, *64*, 361.

[2]   Smith, M. B.; Michl, J. *Chemical Reviews* **2010**, *110*, 6891.

[3]   Hanna, M. C.; Nozik, A. J. *Journal of Applied Physics* **2006**, *100*.

[4]   Geacintov, N.; Pope, M.; Vogel, F. *Physical Review Letters* **1969**, *22*, 593.

[5]   Paci, I.; Johnson, J. C.; Chen, X.; Rana, G.; Popović, D.; David, D. E.; Nozik, A. J.; Ratner, M. A.; Michl, J. *Journal of the American Chemical Society* **2006**, *128*, 16546.

[6]   Jundt, C.; Klein, G.; Sipp, B.; Le Moigne, J.; Joucla, M.; Villaeys, A. A. *Chemical Physics Letters* **1995**, *241*, 84.

[7]   Thorsmølle, V. K.; Averitt, R. D.; Demsar, J.; Smith, D. L.; Tretiak, S.; Martin, R. L.; Chi, X.; Crone, B. K.; Ramirez, A. P.; Taylor, A. J. *Physical Review Letters* **2009**, *102*, 017401.

[8]   Chan, W.-L.; Ligges, M.; Jailaubekov, A.; Kaake, L.; Miaja-Avila, L.; Zhu, X.-Y. *Science* **2011**, *334*, 1541.

[9]   Wilson, M. W. B.; Rao, A.; Clark, J.; Kumar, R. S. S.; Brida, D.; Cerullo, G.; Friend, R. H. *Journal of the American Chemical Society* **2011**, *133*, 11830.

[10]   Marciniak, H.; Fiebig, M.; Huth, M.; Schiefer, S.; Nickel, B.; Selmaier, F.; Lochbrunner, S. *Physical Review Letters* **2007**, *99*, 176402.

[11]   Marciniak, H.; Pugliesi, I.; Nickel, B.; Lochbrunner, S. *Physical Review B* **2009**, *79*, 235318.

[12]   Johnson, J. C.; Nozik, A. J.; Michl, J. *Journal of the American Chemical Society* **2010**, *132*, 16302.

[13]   Burdett, J. J.; Müller, A. M.; Gosztola, D.; Bardeen, C. J. *The Journal of Chemical Physics* **2010**, *133*.

[14]   Wilson, M. W. B.; Rao, A.; Johnson, K.; Gélinas, S.; di Pietro, R.; Clark, J.; Friend, R. H. *Journal of the American Chemical Society* **2013**, *135*, 16680.

[15]   Greyson, E. C.; Vura-Weis, J.; Michl, J.; Ratner, M. A. *The Journal of Physical Chemistry B* **2010**, *114*, 14168.

[16]   Yost, S. R.; Lee, J.; WilsonMark, W. B.; Wu, T.; McMahon, D. P.; Parkhurst, R. R.; Thompson, N. J.; Congreve, D. N.; Rao, A.; Johnson, K.; Sfeir, M. Y.; Bawendi, M. G.; Swager, T. M.; Friend, R. H.; Baldo, M. A.; Van Voorhis, T. *Nature Chemistry* **2014**, *6*, 492.

[17]   Haas, S.; Matsui, H.; Hasegawa, T. *Physical Review B* **2010**, *82*, 161301.

[18]   Tiago, M. L.; Northrup, J. E.; Louie, S. G. *Physical Review B* **2003**, *67*, 115212.

[19]   Sebastian, L.; Weiser, G.; Bässler, H. *Chemical Physics* **1981**, *61*, 125.

[20]   Schuster, R.; Knupfer, M.; Berger, H. *Physical Review Letters* **2007**, *98*, 037402.

[21]   Pac, B.; Petelenz, P. *ChemPhysChem* **2014**, *15*, 2801.

[22]   Zimmerman, P. M.; Bell, F.; Casanova, D.; Head-Gordon, M. *Journal of the American Chemical Society* **2011**, *133*, 19944.

[23]   Beljonne, D.; Yamagata, H.; Brédas, J. L.; Spano, F. C.; Olivier, Y. *Physical Review Letters* **2013**, *110*, 226402.

[24]   Zimmerman, P. M.; Zhang, Z.; Musgrave, C. B. *Nature Chemistry* **2010**, *2*, 648.

[25]   Casanova, D. *Journal of Chemical Theory and Computation* **2013**, *10*, 324.

[26]   Jortner, J.; Rice, S. A.; Katz, J. L.; Choi, S. I. *The Journal of Chemical Physics* **1965**, *42*, 309.

[27]   Valeev, E. F.; Coropceanu, V.; da Silva Filho, D. A.; Salman, S.; Bredas, J. L. *Journal of the American Chemical Society* **2006**, *128*, 9882.

[28]   Renaud, N.; Sherratt, P. A.; Ratner, M. A. *The Journal of Physical Chemistry Letters* **2013**, *4*, 1065.

[29]   Smith, M. B.; Michl, J. *Annual Review of Physical Chemistry* **2013**, *64*, 361.

[30]   Havenith, R. W. A.; de Gier, H. D.; Broer, R. *Molecular Physics* **2012**, *110*, 2445.

[31]   Marcus, R. A. *Reviews of Modern Physics* **1993**, *65*, 599.

[32]   Jortner, J.; Bixon, M. *The Journal of Chemical Physics* **1988**, *88*, 167.

[33]   Yost, S. R.; Hontz, E.; Yeganeh, S.; Van Voorhis, T. *The Journal of Physical Chemistry C* **2012**, *116*, 17369.

[34]   Zeng, T.; Hoffmann, R.; Ananth, N. *Journal of the American Chemical Society* **2014**, *136*, 5755.

[35]   Grumstrup, E. M.; Johnson, J. C.; Damrauer, N. H. *Physical Review Letters* **2010**, *105*, 257403.

[36]   Holmes, D.; Kumaraswamy, S.; Matzger, A. J.; Vollhardt, K. P. C. *Chemistry- A European Journal* **1999**, *5*, 3399.

[37]   Dovesi, R.; Orlando, R.; Erba, A.; Zicovich-Wilson, C. M.; Civalleri, B.; Casassa, S.; Maschio, L.; Ferrabone, M.; De La Pierre, M.; D'Arco, P.; Noël, Y.; Causà, M.; Rérat, M.; Kirtman, B. *International Journal of Quantum Chemistry* **2014**, *114*, 1287.

[38]   Maschio, L.; Kirtman, B.; Rerat, M.; Orlando, R.; Dovesi, R. *Journal of Chemical Physics* **2013**, *139*.

[39]   Maschio, L.; Kirtman, B.; Orlando, R.; Rèrat, M. *The Journal of Chemical Physics* **2012**, *137*.

[40]   Valiev, M.; Bylaska, E. J.; Govind, N.; Kowalski, K.; Straatsma, T. P.; Van Dam, H. J. J.; Wang, D.; Nieplocha, J.; Apra, E.; Windus, T. L.; de Jong, W. A. *Computer Physics Communications* **2010**, *181*, 1477.

[41]   Hess, B.; Kutzner, C.; van der Spoel, D.; Lindahl, E. *Journal of Chemical Theory and Computation* **2008**, *4*, 435.

[42]   Berendsen, H. J. C.; Vanderspoel, D.; Vandrunen, R. *Computer Physics Communications* **1995**, *91*, 43.

[43]   McDonald, N. A.; Jorgensen, W. L. *The Journal of Physical Chemistry B* **1998**, *102*, 8049.

[44]   Coropceanu, V.; Cornil, J.; da Silva Filho, D. A.; Olivier, Y.; Silbey, R.; Bredas, J. L. *Chemical Reviews* **2007**, *107*, 926.

[45]   Sánchez-Carrera, R. S.; Paramonov, P.; Day, G. M.; Coropceanu, V.; Bredas, J. L. *Journal of the American Chemical Society* **2010**, *132*, 14437.

[46]   Bredas, J. L.; Calbert, J. P.; da Silva Filho, D. A.; Cornil, J. *Proceedings of the National Academy of Sciences* **2002**, *99*, 5804.

[47]   Feng, X.; Luzanov, A. V.; Krylov, A. I. *The Journal of Physical Chemistry Letters* **2013**, *4*, 3845.

[48]   Weinberg-Wolf, J. R.; McNeil, L. E.; Shubin, L.; Christian, K. *Journal of Physics: Condensed Matter* **2007**, *19*, 276204.

[49]   Tomoaki, Y.; Youichi, I.; Hiromasa, I.; Hiromasa, T.; Eunsang, K.; Kenkichi, S.; Ken, S.; Minro, W.; Jun-ichi, N. *Japanese Journal of Applied Physics* **2005**, *44*, 4145.

[50]   Coropceanu, V.; Sánchez-Carrera, R. S.; Paramonov, P.; Day, G. M.; Brédas, J.-L. *Journal of Physical Chemistry C* **2009**, *113*, 4679.

[51]   Roberts, S. T.; McAnally, R. E.; Mastron, J. N.; Webber, D. H.; Whited, M. T.; Brutchey, R. L.; Thompson, M. E.; Bradforth, S. E. *Journal of the American Chemical Society* **2012**, *134*, 6388.

[52]   Girlando, A.; Grisanti, L.; Masino, M.; Brillante, A.; Della Valle, R. G.; Venuti, E. *The Journal of Chemical Physics* **2011**, *135*.

[53]   Fratini, S.; Ciuchi, S. *Physical Review Letters* **2009**, *103*, 266601.

CHAPTER 6

CHARGE-TRANSPORT CHARACTERISTICS AND ELECTRONIC COUPLING MECHANISM IN ORGANIC BIMOLECULAR CHARGE-TRANSFER CRYSTALS

6.1 Introduction

Organic semiconductors based on bimolecular donor-acceptor (DA) charge-transfer complexes recently received much attention due to promising ambipolar characteristics of these materials [1]. There is expectedly a strong relationship between the electrical properties and the packing motifs of these DA crystals. Semiconducting properties are usually displayed by mixed-stack systems in which the donor and acceptor molecules alternate along the stacking (...-D-A-D-A-...) directions. A recent Density Functional Theory (DFT) study of the DBTTF-TCNQ, DMQtT-F_4TCNQ (DMQtT = dimethylquaterthiophene, F_4TCNQ = 2,3,5,6-tetrafluoro-7,7,8,8-tetracyanoquino-dimethane), and STB-F_4TCNQ (STB = stilbene) crystals indicated that such DA crystals can exhibit very small effective masses (large electronic couplings) for both holes and electrons, which suggests that these materials can display excellent ambipolar charge-transport properties [2].

In the first part of this Chapter, we evaluate the electronic band structures and related charge-transport characteristics of a series of mixed-stacked donor-acceptor crystals (Figure 4.1). We show that these donor-acceptor crystals exhibit larger valence and

conduction bandwidths compared to prototypical one-component systems, such as pentacene, suggesting promising applications in semiconductor-based devices.
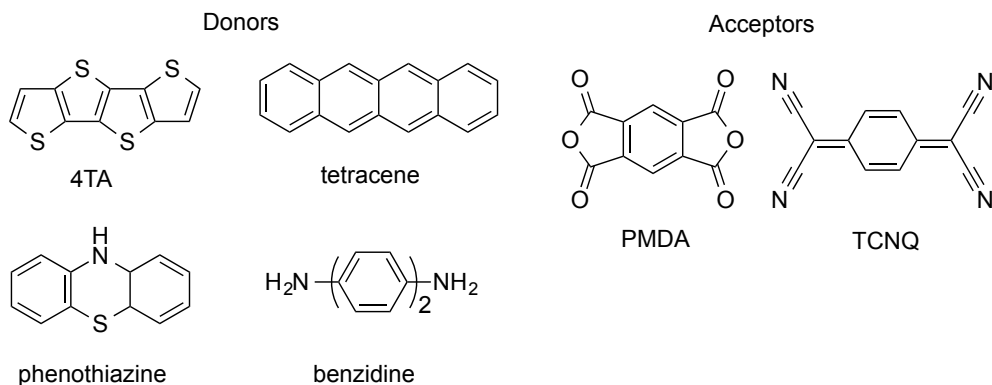
Figure 6.1 Chemical structures of the donor and acceptor molecules: tetracene, benzidine (BZ), thieno[2″,3″:4′,5′]thieno[2′,3′-*d*]thieno[3,2-b]thiophene (4TA), phenothiazine (PTZ), 7,7,8,8-tetracyanoquinodimethane (TCNQ), and pyromellitic dianhydride (PMDA).

It was also pointed out that the electronic couplings along the stacking directions in these DA crystals are superexchange in nature, *i.e.*, the electronic coupling for holes results from the mixing of the frontier orbitals of two closest donor molecules with the orbitals of the "bridging" acceptor molecule and vice versa for electrons. These superexchange couplings, in general, depend on the electronic interactions between the donor and acceptor frontier orbitals and on the related energy gaps.

In the second part of this Chapter, we turn to a more technical issue and compare how the electronic couplings, band gaps, bandwidths, and effective masses depend on the amount of nonlocal Hartree-Fock exchange in the case of pentacene and DBTTF-TCNQ, which are taken as representative examples of single-component and donor-acceptor crystals (Figure 6.2). We show that the unusual dependences of electronic couplings, bandwidths,

and effective masses found in DBTTF-TCNQ can be attributed to the superexchange nature of the electronic couplings in this class of materials. This chapter is based on results published in *Physical Review B* [3] and *The Journal of Physical Chemistry C* [4].
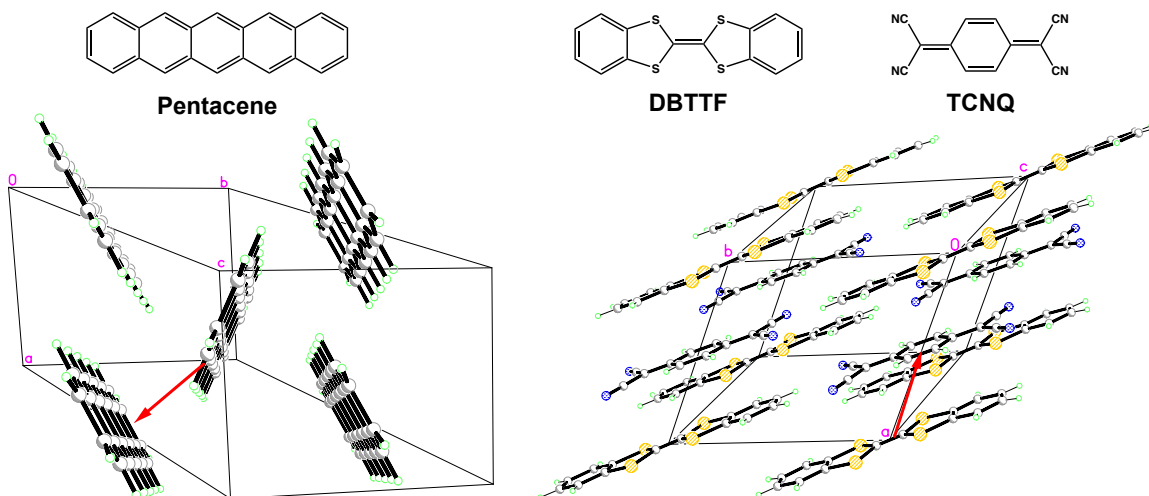
Figure 6.2 Chemical and crystal structures of the investigated systems: Pentacene [5] (left) and DBTTF-TCNQ [6] (right). Red arrows indicate the directions of the largest transfer integrals as well as of the smallest effective masses for both holes and electrons.

6.2 Computational methodology

For BZ-TCNQ, PTZ-TCNQ, 4TA-TCNQ and tetracene-PMDA crystals (see abbreviations in the caption of Figure 6.1), the electronic band structures and density of states (DOS) were calculated using the optimized crystal structures at the B3LYP/6-31G level. Effective masses were computed as described below. Electronic-structure calculations on both pentacene (*V* polymorph with inter-layer spacing of 14.1 Å) [5] and DBTTF-TCNQ [6] have been performed on the basis of their experimental crystal structures. The impact of the %HF exchange has been investigated by using the αPBE

functional, based on the original PBE functional [7,8], following the simple hybrid scheme proposed by Adamo and Barone [9]:

$$E_{\alpha PBE} = \alpha E_X^{HF} + (1 - \alpha)E_X^{PBE} + E_C^{PBE}, \qquad (6.1)$$

where α = 0.25 corresponds to the PBE0 functional.

Direct electronic couplings were evaluated by using the fragment orbital approach [10] implemented in the developmental version of the NWChem package [11] in conjunction with the 6-31G* basis set. For the "two-component" system, effective hole [electron] electronic couplings were evaluated using donor-acceptor-donor [acceptor-donor-acceptor] triads, as was done in previous work of our research group [2]. CRYSTAL09 [12] was used to perform all calculations using the αPBE functional combined with the 6-31G basis set. The Brillouin zone was sampled using a Γ-centered uniform k-point 6x6x6 grid for the pentacene crystal and a 6x6x8 grid for the DBTTF-TCNQ crystal. The effective masses and their orientations were calculated by diagonalizing the inverse of the effective mass tensor (m_{ij}^{-1}). The latter was obtained from the valence band maximum or conduction band minimum using a finite-difference method on a five-point stencil with a 0.01 Bohr^{-1} step (1 Bohr = 0.529 Å). G_0W_0 calculations for the pentacene and DBTTF-TCNQ crystals were performed using the BerkeleyGW code [13], starting from the PBE-derived wavefunctions and energies obtained from Quantum Espresso [14] with norm-conserving Troullier-Martins pseudopotentials [15]. The static dielectric matrix cutoff was set to 15 Ry (204.1 eV). For the static dielectric matrix calculations (required for the evaluation of the screened Coulomb interaction, W, within GW), the generalized plasmon model was used [16], with 464 unoccupied bands for both pentacene and DBTTF-TCNQ.

Γ-centered uniform meshes of 4x4x2 and 4x4x4 k-points were employed for pentacene and DBTTF-TCNQ, respectively. For the sake of comparison, in addition to the calculations that rely on an atomic orbital basis set (performed in CRYSTAL09), VASP [17-20] calculations with standard and range-separated hybrid functionals using a plane-wave basis set (PAW method) were also performed [21,22]. For both pentacene and DBTTF-TCNQ crystals, a plane wave energy cutoff of 800 eV and a 2x2x2 k-point mesh were employed.

6.3 Results and discussion

6.3.1 Electronic structure and transport properties of promising donor-acceptor crystals

The electronic band structures of BZ-TCNQ, PTZ-TCNQ, 4TA-TCNQ, and tetracene-PMDA crystals are displayed in Figure 6.3. These crystals possess large bandwidths, about 400–860 meV, for both valence and conduction bands. These bandwidths are comparable to those of the DBTTF-TCNQ, DMQtT-F_4TCNQ and stilbene-F_4TCNQ crystals our group investigated earlier [2]. For the sake of comparison, we note that the VB and CB bandwidths in the pentacene crystal are 610 and 590 meV, respectively, at the same level of theory [23]. Among all investigated donor-acceptor systems, BZ-TCNQ displays the largest width for both VB and CB, *i.e.*, 690 and 860 meV, respectively. For the systems considered here, the largest VB and CB dispersions occur along the stacking directions.
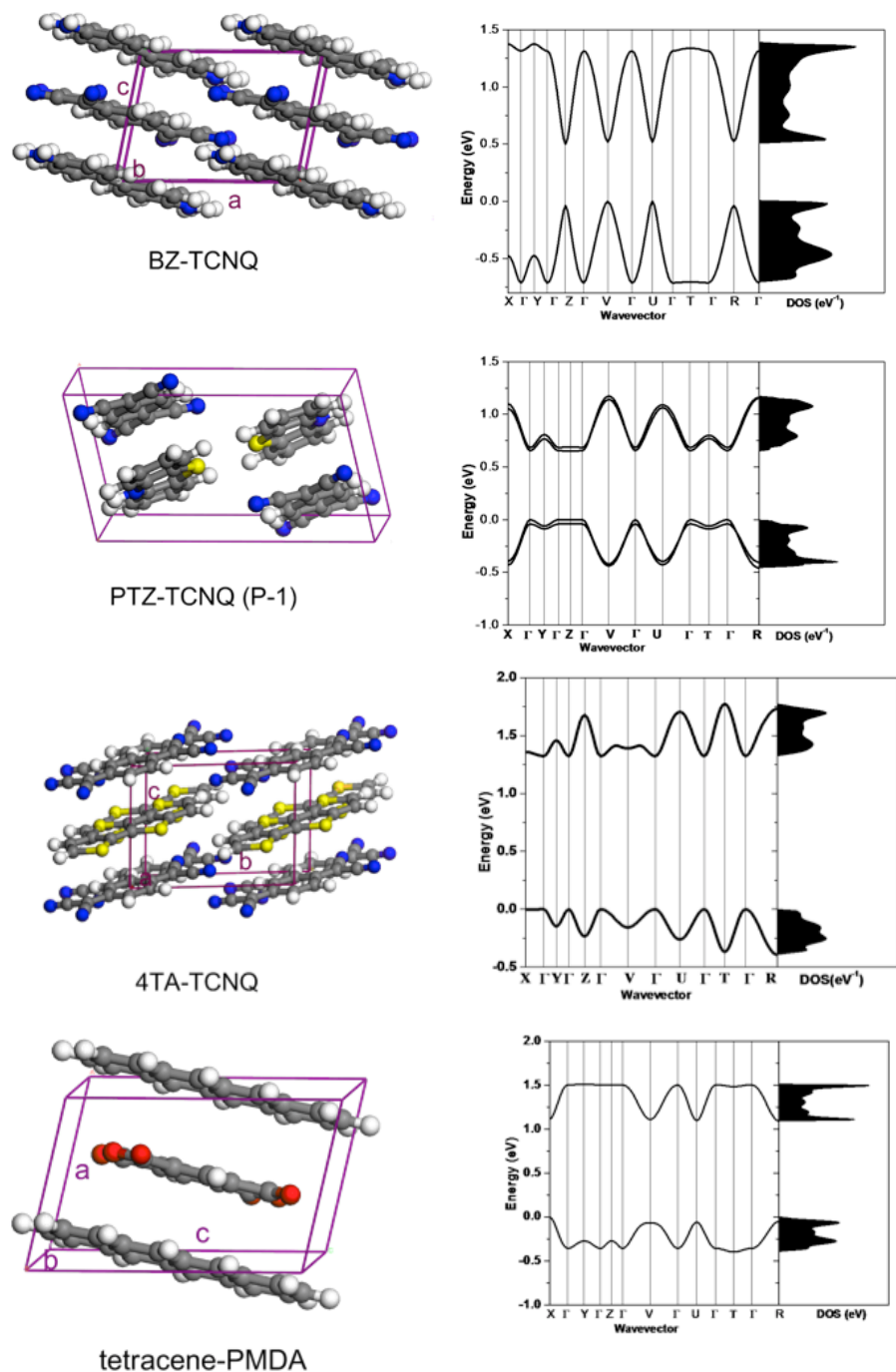
Figure 6.3 Electronic band structures and densities of states (DOS) of the investigated systems. The points of high symmetry in the first Brillouin zone are labeled as follows: Γ = (0, 0, 0), X = (0.5, 0, 0), Y = (0, 0.5, 0), Z = (0, 0, 0.5), U,C = (0, 0.5, 0.5), V,D = (0.5, 0, 0.5), T, A = (0.5, 0.5, 0) and R,E = (0.5, 0.5, 0.5), except for anthracene-TCNQ, Γ = (0, 0, 0), A = (0.5, 0, 0), V = (0, 0, 0.5), Z = (0, 0.5, 0.5), M = (0.5, 0.5, 0.5) and L = (0.5, 0, 0.5), all in crystallographic coordinates. Taken from Ref. [4].

We also computed the effective masses of these systems. Both holes and electrons effective masses are very small, in the range of 0.24–0.86 m_0 for holes and 0.22–0.82 m_0 for electrons, which is consistent with the large bandwidths. Remarkably small effective masses for holes, 0.24 m_0, and electrons, 0.22 m_0, are found in BZ-TCNQ. These masses are comparable to those estimated recently for the DMQtT-F$_4$TCNQ crystal (0.20 m_0 and 0.26 m_0, for holes and electrons) [2]. For the sake of comparison, we recall that the effective masses estimated at the same level of theory for holes in pentacene [24] and rubrene [25] are about 1.6 m_0 and 0.94 m_0, respectively. Our results thus indicate that all the donor-acceptor systems discussed above have small effective masses for both holes and electrons, which underlines that these systems could exhibit ambipolar charge-transport properties. We note that, BZ-TCNQ, PTZ-TCNQ, and tetracene-PMDA have just one small effective mass component; therefore, they are expected to exhibit mainly one-dimensional (1D) charge-transport characteristics. In contrast, 4TA-TCNQ has two small effective mass components for both holes and electrons; thus, these systems could display not only ambipolar characteristics but also two-dimensional (2D) charge-transport features. The nature of the electronic couplings in the donor-acceptor systems is discussed next.

6.3.2 Impact of exact exchange in the description of the electronic structure of organic molecular crystals

6.3.2.1 Electronic structure and charge-transport properties of pentacene

We first discuss the impact that the %HF exchange in the αPBE functional has on the band structure and effective masses of pentacene (Figures 6.4, 6.5). For the range between 0 to 50 %HF exchange, the valence [conduction] bandwidth increases by 0.207 [0.275] eV, *i.e.*, by about 40%. This result is consistent with the increase in electronic coupling evaluated from a dimer calculation, which was previously attributed to the fact that (semi)local functionals have an exchange-correlation potential that decays too quickly [26]. The effective masses for holes [electrons] were calculated at the valence band maximum (0.375, 0.5, 0.075) [conduction band minimum (0.39, 0.5, 0.5)] in reciprocal space; the smallest effective mass both for holes and electrons are estimated to be approximately along the herringbone direction (Figure 6.2). The effective masses for holes [electrons] decrease almost linearly ($R^2 = 0.977$ [0.974]) from 2.011 to 1.406 [1.952 to 1.363] m_0 with increasing %HF exchange, thus with an increasing transfer integral. This trend can be explained in the framework of the tight-binding model, where, in the simple one-dimensional case, $m_{1D} = \hbar^2/2td^2$, where d represents the intermolecular distance. The band gap also shows a linear increase ($R^2 = 0.999$), by a factor of 3 from 0.83 to 3.08 eV (Figure 6.4), in agreement with previous findings [27]. These results underline that depending on the %HF exchange used in a given functional, the DFT estimates for the band gap, bandwidth, and effective mass can span a wide range.

More accurate results can be obtained by employing higher-level, first-principles electronic-structure methods. For instance, it has been shown that calculations performed within the *GW* approximation [16,28] can reproduce the experimental fundamental gaps and valence and conduction bandwidths for both inorganic and organic semiconductors with a high accuracy, though at a much higher computational cost [16,29]. Here, we have used the G_0W_0 results to calibrate the amount of HF exchange in the αPBE functional for the present systems. The G_0W_0 results are in very good agreement (see Table 6.1) with those derived previously [30]. Tuning the %HF exchange in αPBE to recover the fundamental gap obtained from G_0W_0 calculations (at the *E* point in the Brillouin zone) results in a value of 32% HF exchange. Importantly, the valence and conduction bandwidths derived by this tuned functional at the *E* point and other *k*-points (Table 6.1, Figure 6.5) are also in excellent agreement with the G_0W_0 calculations.
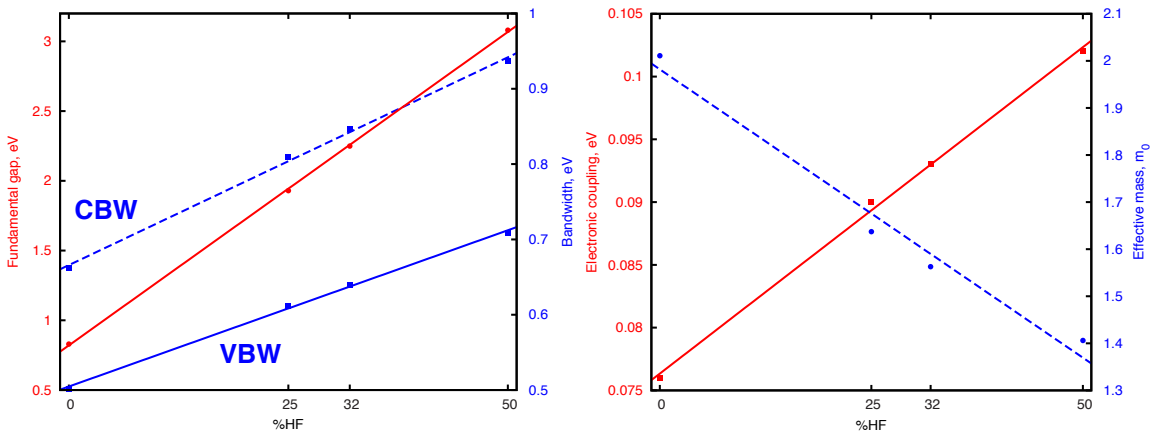
Figure 6.4 Left: Dependence of the fundamental gap and valence and conduction bandwidths on the %HF exchange. Right: dependence of the largest hole electronic coupling and smallest hole effective mass on %HF exchange in the crystalline *V* polymorph of pentacene.

Table 6.1 Fundamental gap (Eg, eV) at the *E* point, smallest hole and electron effective masses (m$^{Hole}_{eff}$ and m$^{El}_{eff}$ in the units of mass of the electron at rest, m$_0$), valence (VBW) and conduction (CBW) bandwidths (eV) at the *E* point.

%HF	E$_g$	m$^{Hole}_{eff}$	m$^{El}_{eff}$	VBW	CBW	t^{Hole}	t^{El}
0	0.83	2.011	1.952	0.502	0.662	0.076	0.080
25	1.93	1.637	1.581	0.612	0.809	0.090	0.094
32	2.25	1.563	1.511	0.640	0.846	0.093	0.098
50	3.08	1.406	1.363	0.709	0.937	0.102	0.107
G$_0$W$_0$	2.22	-	-	0.648	0.859	-	-
G$_0$W$_0$ [30]	1.9	-	-	0.54	0.67	-	-
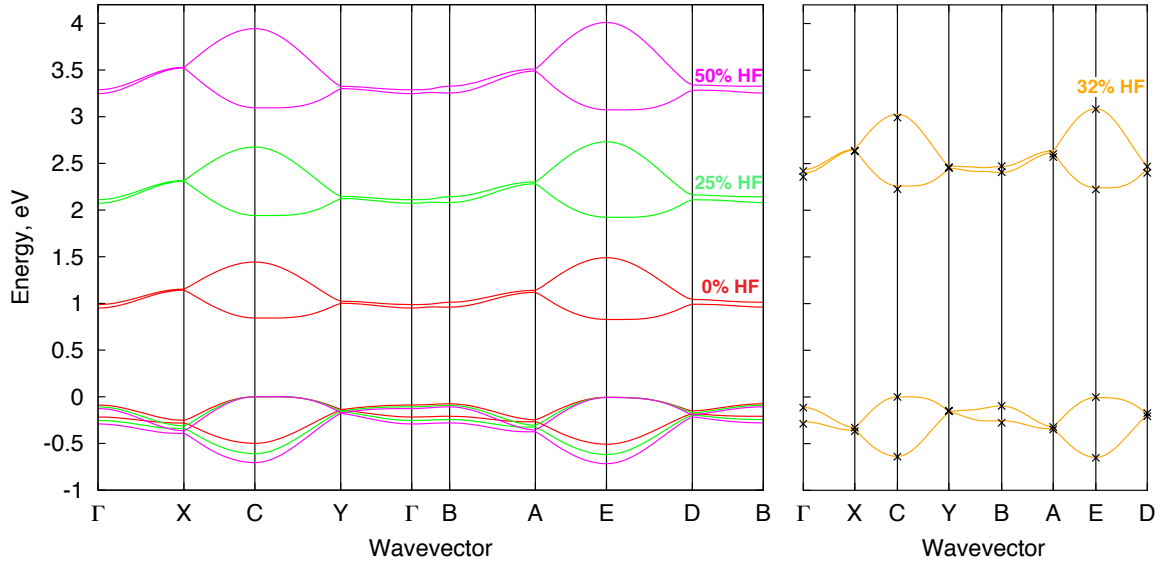
Figure 6.5 Left: Valence and conduction bands of pentacene obtained using the αPBE functional with different %HF. Right: Comparison of αPBE (solid lines) and G$_0$W$_0$ (crosses) results. The points of high symmetry in the first Brillouin zone are labeled as follows: Γ = (0,0,0), X = (0.5,0,0), Y = (0,0.5,0), B = (0,0,0.5), C = (0.5,0.5,0), A = (0.5,0,0.5), E = (0.5,0.5,0.5) and D = (0, 0.5, 0.5), all in crystallographic coordinates. The zero of energy corresponds to the top of the valence band, at the *C* point.

6.3.2.2 Electronic structure and charge-transport properties of DBTTF-TCNQ

We turn now to the "two-component" donor-acceptor systems that are expected to exhibit lower band gaps than the crystals of the individual components. In fact, when a pure functional or a functional with a low amount of the HF exchange (<10%) is employed, the gap in DBTTF-TCNQ goes to zero (*i.e.*, the system shows a metallic behavior) or demonstrates an unusual evolution that is no longer linear. Similar behavior was reported for another mixed-stack ferroelectric donor-acceptor system, tetrathiafulvalene-*p*-chloranil (TTF-CA) [31]. This behavior can be attributed to the well-known underestimation of the computed band gaps with (semi)local DFT functionals [32]. We also note that the calculations using a large %HF display convergence difficulties. Therefore, we only discuss below the results obtained within a range of 10–40 %HF exchange.

The valence [conduction] band structure as a function of %HF exchange is shown in Figure 6.6. The effective masses for holes [electrons] were evaluated at the (0.0, 0.5, 0.5) [(0.0, 0.0, 0.0)] point in reciprocal space, with the smallest effective mass both for holes and electrons found along the stacking direction (*a*-axis) (Figure 6.2). The striking difference compared to the one-component systems is the very weak evolution of the valence [conduction] bandwidths: 0.029 [0.033] eV within the range of 10–40 %HF exchange. As a consequence, there occurs only a very slight *increase* in the effective masses (as opposed to the significant decrease in effective mass with %HF observed in pentacene) for both holes [0.299 to 0.407 m_0] and electrons [0.315 to 0.461 m_0] (Table 6.2). We note that very similar values for bandwidths are found as well when using the

PAW basis set, which confirms that the evolution is not related to the choice of basis set.

In contrast to the very slight evolution of the bandwidths, an increase in %HF leads, as in

the case of pentacene, to a linear increase of the fundamental gap (by a factor of ~3, from

0.50 to 1.67 eV, over the 10–40 %HF range) (Figure 6.6).
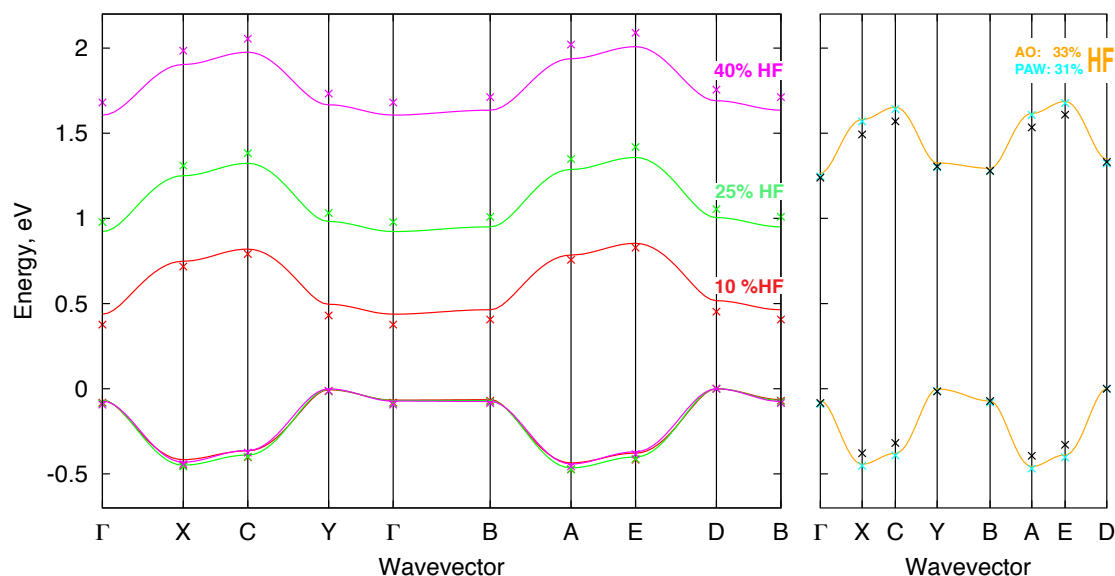
Figure 6.6 Left: Valence and conduction bands of DBTTF-TCNQ obtained using the αPBE functional with different amount of %HF and different basis sets: atomic orbitals (solid) and PAWs (colored crosses). Right: Comparison of αPBE and G_0W_0 (black crosses). The rest of notation similar to Figure 6.5.

Table 6.2 Fundamental gap (E_g, eV) at the Γ point; the smallest hole and electron effective mass (m^{Hole}_{eff} and m^{El}_{eff} in units of the mass of the electron at rest, m_0); valence bandwidth (VBW, eV) at the *A* point and conduction bandwidth (CBW, eV) at the *E* point for the DBTTF-TCNQ crystal.

%HF	E_g		m^{Hole}_{eff}	m^{El}_{eff}	VBW		CBW	
Basis set	AO	PAW	AO	AO	AO	PAW	AO	PAW
10	0.50	0.44	0.299	0.315	0.436	0.473	0.416	0.451
25	0.98	1.06	0.338	0.368	0.465	0.474	0.435	0.441
33[1]/31[2]	1.33	1.34	0.372	0.413	0.457	0.469	0.421	0.430
40	1.67	1.75	0.407	0.461	0.442	0.456	0.402	0.410
G_0W_0	1.32		-	-	0.364		0.344	

[1] AO (atomic orbitals); [2] PAW (plane augmented waves)

The significant difference in the manifestation of the %HF exchange on the band structures of pentacene and DBTTF-TCNQ can be attributed to the difference in the nature of electronic couplings in one- and two-component systems. In pentacene, the electronic couplings depend on the direct, through-space wavefunction overlap; in contrast, in DBTTF-TCNQ, the electronic couplings have a superexchange nature, *i.e.*, the electronic coupling for holes [electrons] results from the mixing of the frontier orbitals of two closest donor [acceptor] molecules with the frontier orbitals of the "bridging" acceptor [donor] molecule [2]. In the context of such a superexchange mechanism, both the electronic coupling and the energy difference between the relevant frontier molecular orbitals on adjacent donor and acceptor molecules have to be taken into account.

Using perturbation theory and assuming that only the pathway described above contributes to the superexchange mechanism, the effective transfer integrals for holes and electrons along the stacking directions are equal and are given by [2]:

$$t^{eff}_{H_D-H_D} = t^{eff}_{L_A-L_A} = \frac{t^2_{H_D-L_A}}{\Delta E}. \tag{6.2}$$

Here, $t_{H_D-L_A}$ is the electronic coupling between the HOMO of a donor and the LUMO of the adjacent acceptor; ΔE represents the energy of the charge-transfer state of the donor-acceptor dyad, which can be approximated by the energy of the fundamental gap. Thus, since both the band gap and the donor-acceptor electronic coupling concomitantly increase with the increase in %HF, the effective transfer integrals ($t^{eff}_{H_D-H_D}, t^{eff}_{L_A-L_A}$) are less sensitive to the choice of %HF (Figure 6.7) than $t_{H_D-L_A}$ and ΔE individually. We note that Equation 6.2 applies only in the perturbation limit, that is, when $t \ll \Delta E$. In the

case where $t_{H_D-L_A}$ and ΔE are comparable, which is the situation in DBTTF-TCNQ (Figure 6.7), the effective transfer integrals are expected to exhibit a more complex dependence on $t_{H_D-L_A}$ and ΔE. Indeed, the values of $t^{eff}_{H_D-H_D}$ derived by means of the non-perturbative energy splitting approach [2] show a much weaker dependence on %HF than those derived via Equation 6.1 (Figure 6.7).
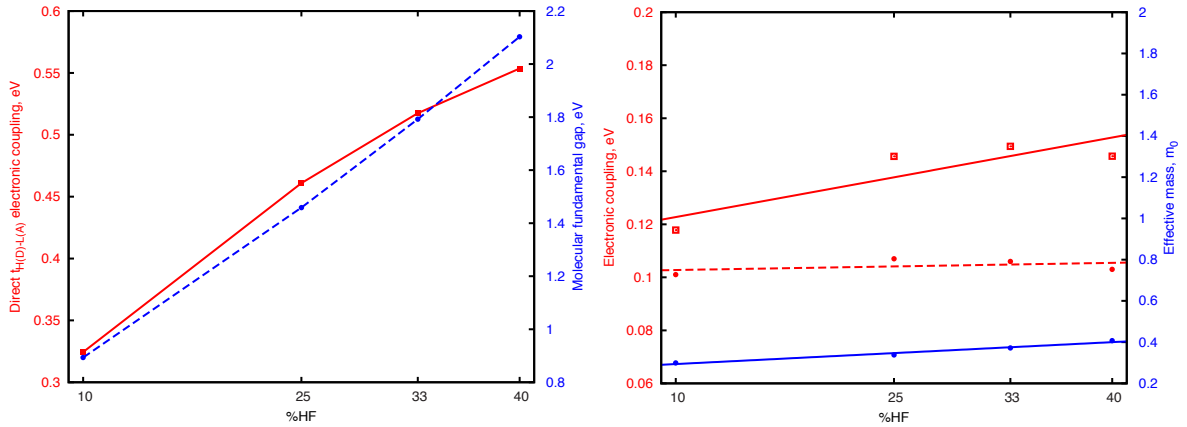
Figure 6.7 Left: Dependence of the donor-acceptor electronic coupling and molecular fundamental gap on the %HF exchange. Right: dependence of the largest effective hole electronic coupling based on the energy splitting approach (dashed line) and using Equation 6.2 (solid line) and the smallest hole effective mass, on the %HF exchange in the DBTTF-TCNQ crystal.

Using G_0W_0, the fundamental gap for DBTTF-TCNQ is calculated to be 1.32 eV. When tuning the amount of %HF exchange in αPBE to recover the G_0W_0 result, a band gap of 1.33 eV is obtained with 33% HF exchange using an atomic orbital basis set and of 1.34 eV with 33% HF exchange using PAW. Irrespective of the basis set, the functional tuned against the G_0W_0 band gap slightly overestimates the bandwidths along the charge-transfer stacking direction (mainly Γ-X) in comparison to the G_0W_0 results. In order to overcome this deficiency, we also turned to a range-separated functional:

$$E_{\alpha\mu DFT} = E_X^{HF,SR}(\mu) + \alpha E_X^{HF,LR}(\mu) + (1-\alpha)E_X^{PBE,LR}(\mu) + E_C^{PBE}, \qquad (6.3)$$

where the decomposition of the Coulomb operator is obtained using the error function:

$$\frac{1}{r} = \frac{\text{erfc}(\mu r)}{r} + \frac{\text{erf}(\mu r)}{r}. \tag{6.4}$$

In the case of $\mu = 0.0$ Å^{-1}, the Coulomb operator is equal to only the Hartree-Fock exchange short-range term. In the case of $\mu \to \infty$, the Coulomb operator encompasses both long-range exchange terms: PBE and HF. Similar schemes [33] for long-range separated functionals were shown to describe well valence orbitals in finite molecular systems [34,35]. In the case of non-empirical tuning for a system-dependent μ [36], evaluation of the charged system (*i.e.*, cation or anion) is also required; this has been readily demonstrated for single-molecule systems [34] that allow for comparison to G_0W_0 results. However, charged-cell calculations are problematic for periodic systems (see the discussion about the evaluation of the ionization potential in the benzene crystal in Ref. [37]). Eigenvalues for valence and conduction bands for several α values with the fixed separation parameter ($\mu = 0.7$ Å^{-1}) are plotted in Figure 6.8. Similar to what was computed using a tuned global-hybrid functional, a linear increase in band gap is observed. With the variation of μ, two effects are observed (see Figure 6.8): (i) the band gap increases with the decrease of μ, since more %HF exchange is included in the functional; (ii) bandwidths are mostly altered along the charge transfer directions. In the case of $\mu \to \infty$, the αPBE bandwidths are recovered. The best agreement between G_0W_0 and $\alpha\mu$DFT is obtained for α equal to 20 %HF exchange and $\mu = 0.7$ Å^{-1}. This suggests that splitting the exchange term into short- and long-range components, in a density functional, allows the correct description of the extent of charge transfer in the ground state [38,39].
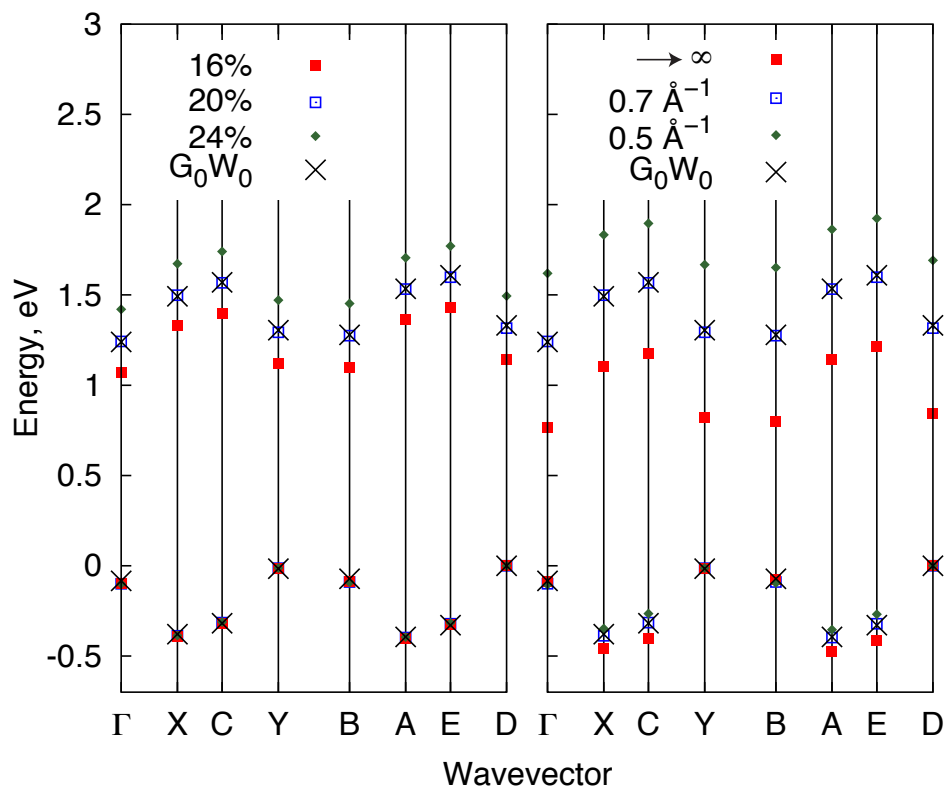
Figure 6.8 Valence and conduction bands of DBTTF-TCNQ obtained using the αμDFT functional. G_0W_0 values are shown for comparison. Left: Different %HF exchange values in the long range, separation parameter (μ) fixed to 0.7 Å^{-1}. Right: Different values of μ, for fixed %HF exchange (α) at 20. The points of high symmetry in the first Brillouin zone are labeled similarly to Figure 6.6.

6.4 Conclusions

In the first part of this Chapter, we have investigated the electronic structures of a series of donor-acceptor mixed-stacked crystals by means of DFT calculations. The band-structure calculations indicate large valence-band and conduction-band widths for BZ-TCNQ, PTZ-TCNQ, 4TA-TCNQ, and tetracene-PMDA. The calculations also predict very small effective masses for these systems; they are in the range of 0.2–0.8 m_0 for holes and 0.2–0.7 m_0 for electrons. These values are smaller than the effective mass for holes in pentacene and rubrene and comparable with recently published results for the

DMQtT-F$_4$TCNQ, DBTTF-TCNQ, and STB-F$_4$TCNQ crystals. Overall, among the series investigated in this work, the BZ-TCNQ and PTZ-TCNQ crystals appear as the most promising materials with regard to charge-transport properties. They present large valence and conduction bandwidths and small hole and electron effective masses. Two small components of the effective masses are found for several crystals, suggesting that charge transport for both holes and electrons has a two-dimensional character.

In the second part of this Chapter, we have evaluated the dependence on the amount of HF exchange included in the density functional of the charge-transport parameters in two organic semiconductor crystals, pentacene and DBTTF-TCNQ. We have found that in one-component systems such as pentacene, the fundamental gap, bandwidths, and effective masses vary significantly and in a linear fashion as a function of %HF exchange. We have confirmed the superexchange mechanism of the electronic coupling in mixed-stack, donor-acceptor systems such as DBTTF-TCNQ. The superexchange nature of the electronic coupling affects the dependence of the electronic properties on %HF exchange; in particular, with an increase in the %HF exchange included in the functional, the bandwidths and effective masses remain nearly constant, in marked contrast to the evolution observed in one-component systems. We have also found that in both types of systems, the band gaps show a similar evolution, increasing by a factor of at least 3 when increasing the percentage of HF exchange from ~0 to ~50%. This is particularly important to realize when considering two-component systems, such as DBTTF-TCNQ, which is calculated to be metallic when small (or no) amount of HF exchange is included in the functional. We have also shown that, by changing the amount

of the HF exchange in the αPBE functional, the αPBE band gap can be tuned to match the G_0W_0 band gap, with the resulting bandwidths also in good agreement with those obtained from G_0W_0. Interestingly, the optimum %HF exchange found here (in the range 31–33%) is very similar to the recently developed PBE0-1/3 functional, which is parameterized with 33%HF exchange and outperforms the original PBE0 functional with 25%HF exchange for a variety of molecular electronic properties [40].

6.5 References

[1]   Goetz, K. P.; Vermeulen, D.; Payne, M. E.; Kloc, C.; McNeil, L. E.; Jurchescu, O. D. *Journal of Materials Chemistry C* **2014**, *2*, 3065.

[2]   Zhu, L.; Yi, Y.; Li, Y.; Kim, E.-G.; Coropceanu, V.; Bredas, J. L. *Journal of the American Chemical Society* **2012**, *134*, 2340.

[3]   Fonari, A.; Sutton, C.; Brédas, J.-L.; Coropceanu, V. *Physical Review B* **2014**, *90*, 165205.

[4]   Zhu, L.; Yi, Y.; Fonari, A.; Corbin, N. S.; Coropceanu, V.; Brédas, J.-L. *Journal of Physical Chemistry C* **2014**, *118*, 14150.

[5]   Siegrist, T.; Besnard, C.; Haas, S.; Schiltz, M.; Pattison, P.; Chernyshov, D.; Batlogg, B.; Kloc, C. *Advanced Materials* **2007**, *19*, 2079.

[6]   Emge, T. J.; Wiygul, F. M.; Chappell, J. S.; Bloch, A. N.; Ferraris, J. P.; Cowan, D. O.; Kistenmacher, T. J. *Molecular Crystals and Liquid Crystals* **1982**, *87*, 137.

[7]   Perdew, J. P.; Burke, K.; Ernzerhof, M. *Physical Review Letters* **1996**, *77*, 3865.

[8]   Perdew, J. P.; Burke, K.; Ernzerhof, M. *Physical Review Letters* **1997**, *78*, 1396.

[9]   Adamo, C.; Barone, V. *The Journal of Chemical Physics* **1999**, *110*, 6158.

[10]   Valeev, E. F.; Coropceanu, V.; da Silva Filho, D. A.; Salman, S.; Bredas, J. L. *Journal of the American Chemical Society* **2006**, *128*, 9882.

[11]   Valiev, M.; Bylaska, E. J.; Govind, N.; Kowalski, K.; Straatsma, T. P.; Van Dam, H. J. J.; Wang, D.; Nieplocha, J.; Apra, E.; Windus, T. L.; de Jong, W. A. *Computer Physics Communications* **2010**, *181*, 1477.

[12]   Dovesi, R.; Orlando, R.; Civalleri, B.; Roetti, C.; Saunders, V. R.; Zicovich-Wilson, C. M. *Zeitschrift für Kristallographie - Crystalline Materials* **2005**, *220*, 571.

[13]   Deslippe, J.; Samsonidze, G.; Strubbe, D. A.; Jain, M.; Cohen, M. L.; Louie, S. G. *Computer Physics Communications* **2012**, *183*, 1269.

[14]   Giannozzi, P.; Baroni, S.; Bonini, N.; Calandra, M.; Car, R.; Cavazzoni, C.; Ceresoli, D.; Chiarotti, G. L.; Cococcioni, M.; Dabo, I.; Corso, A. D.; Gironcoli, S. d.; Fabris, S.; Fratesi, G.; Gebauer, R.; Gerstmann, U.; Gougoussis, C.; Kokalj, A.; Lazzeri, M.; Martin-Samos, L.; Marzari, N.; Mauri, F.; Mazzarello, R.; Paolini, S.; Pasquarello, A.; Paulatto, L.; Sbraccia, C.; Scandolo, S.; Sclauzero, G.; Seitsonen, A. P.; Smogunov, A.; Umari, P.; Wentzcovitch, R. M. *Journal of Physics: Condensed Matter* **2009**, *21*, 395502.

[15]   Troullier, N.; Martins, J. L. *Physical Review B* **1991**, *43*, 1993.

[16]   Hybertsen, M. S.; Louie, S. G. *Physical Review B* **1986**, *34*, 5390.

[17]   Kresse, G.; Furthmüller, J. *Computational Materials Science* **1996**, *6*, 15.

[18]   Kresse, G.; Furthmüller, J. *Physical Review B* **1996**, *54*, 11169.

[19]   Kresse, G.; Hafner, J. *Physical Review B* **1993**, *47*, 558.

[20]   Kresse, G.; Hafner, J. *Physical Review B* **1994**, *49*, 14251.

[21]   Blöchl, P. E. *Physical Review B* **1994**, *50*, 17953.

[22]   Kresse, G.; Joubert, D. *Physical Review B* **1999**, *59*, 1758.

[23]   de Wijs, G. A.; Mattheus, C. C.; de Groot, R. A.; Palstra, T. T. M. *Synthetic Metals* **2003**, *139*, 109.

[24]   Coropceanu, V.; Li, Y.; Yi, Y.; Zhu, L.; Brédas, J.-L. *MRS Bulletin* **2013**, *38*, 57.

[25]   Li, Z. Q.; Podzorov, V.; Sai, N.; Martin, M. C.; Gershenson, M. E.; Di Ventra, M.; Basov, D. N. *Physical Review Letters* **2007**, *99*, 016403.

[26]   Sutton, C.; Sears, J. S.; Coropceanu, V.; Bredas, J. L. *The Journal of Physical Chemistry Letters* **2013**, 919.

[27]   Refaely-Abramson, S.; Sharifzadeh, S.; Jain, M.; Baer, R.; Neaton, J. B.; Kronik, L. *Physical Review B* **2013**, *88*, 081204.

[28]   Hedin, L. *Physical Review* **1965**, *139*, A796.

[29]   Sharifzadeh, S.; Biller, A.; Kronik, L.; Neaton, J. B. *Physical Review B* **2012**, *85*, 125307.

[30]   Tiago, M. L.; Northrup, J. E.; Louie, S. G. *Physical Review B* **2003**, *67*, 115212.

[31]   Giovannetti, G.; Kumar, S.; Stroppa, A.; van den Brink, J.; Picozzi, S. *Physical Review Letters* **2009**, *103*, 266401.

[32]   Burke, K. *The Journal of Chemical Physics* **2012**, *136*.

[33]   Yanai, T.; Tew, D. P.; Handy, N. C. *Chemical Physics Letters* **2004**, *393*, 51.

[34]   Refaely-Abramson, S.; Sharifzadeh, S.; Govind, N.; Autschbach, J.; Neaton, J. B.; Baer, R.; Kronik, L. *Physical Review Letters* **2012**, *109*, 226405.

[35]   Lüftner, D.; Refaely-Abramson, S.; Pachler, M.; Resel, R.; Ramsey, M. G.; Kronik, L.; Puschnig, P. *Physical Review B* **2014**, *90*, 075204.

[36]   Stein, T.; Eisenberg, H.; Kronik, L.; Baer, R. *Physical Review Letters* **2010**, *105*, 266802.

[37]   Sai, N.; Barbara, P. F.; Leung, K. *Physical Review Letters* **2011**, *106*, 226403.

[38]   Sini, G.; Sears, J. S.; Brédas, J.-L. *Journal of Chemical Theory and Computation* **2011**, *7*, 602.

[39]   Atalla, V.; Yoon, M.; Caruso, F.; Rinke, P.; Scheffler, M. *Physical Review B* **2013**, *88*, 165122.

[40]   Guido, C. A.; Brémond, E.; Adamo, C.; Cortona, P. *The Journal of Chemical Physics* **2013**, *138*, 021104.

CHAPTER 7

IMPACT OF LATTICE VIBRATIONS ON THE CHARGE-TRANSPORT CHARACTERISTICS OF ORGANIC BIMOLECULAR CHARGE-TRANSFER SEMICONDUCTORS

7.1 Introduction

Bimolecular charge-transfer (CT) organic molecular semiconductors are systems in which one type of molecules act as electron donors (D) and the other as acceptors (A). There is currently an increasing interest in these systems due to their potential applications in opto-electronic devices [1-11]. For example, several research groups have recently fabricated ambipolar field-effect transistors using CT compounds as active elements [3,8-10]. However, in order to design new CT systems of high performance, a deeper understanding of the microscopic parameters that define the electric and electronic properties of these systems is still needed. From a theoretical standpoint, the availability of reliable quantum-mechanical approaches to evaluate the electronic and electron-vibration (phonon) couplings is of critical importance.

Over recent years, density functional theory (DFT) has been extensively used for the evaluation of the charge-transport microscopic parameters in organic semiconductors [12]. However, it was demonstrated that in one-component crystals, such as pentacene, the transfer integrals [13] and electron-vibration couplings [14] are very much sensitive to the choice of DFT functional, in particular to the amount of non-local Hartree-Fock

(HF) exchange included in a hybrid density functional. In Chapter 6, we have studied the dependence of the transfer integrals, bandgaps, bandwidths, and effective masses on the amount of HF exchange in high-mobility CT systems such as mixed-stack dibenzotetrathiafulvalene-7,7,8,8-tetracyanoquinodimethane (DBTTF-TCNQ). In the first part of the present Chapter, we discuss the effect of HF exchange on the vibrational modes, electron-vibration couplings, infra-red (IR) and Raman spectra in CT crystals. As a representative system, we consider anthracene-PMDA (PMDA= pyromellitic dianhydride) where anthracene acts as an electron donor (D) and PMDA as an electron acceptor (A), see Figure 7.1. Our choice is based on the fact that the lowest CT band in the anthracene-PMDA crystal is located at 1.8 eV; thus, this system is well suited for the measurement of non-resonance Raman spectra.
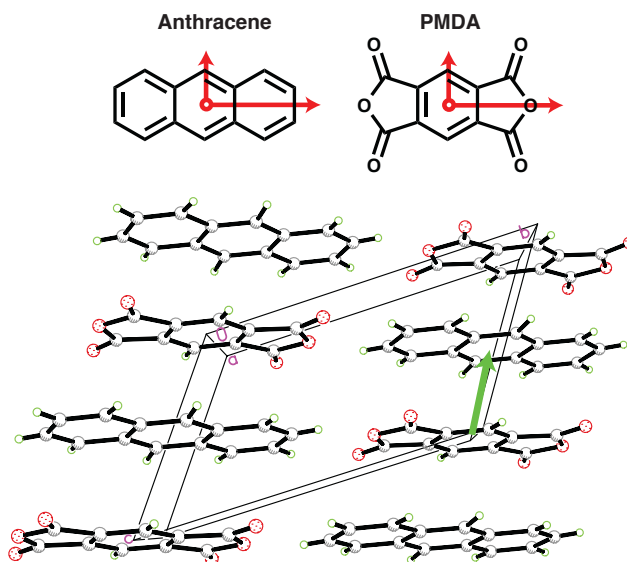
Figure 7.1 Chemical and crystal structures of anthracene-PMDA. The long, short, and z (perpendicular to the plane) molecular axes are shown in red, with the origin defined as the center of the mass. The green arrow indicates the donor-acceptor pair with the largest direct electronic coupling (t_{DA}).

It has been reported that selective IR or Raman excitation can lead to strong modulation of the electronic properties by inducing a lattice phase transition in inorganic perovskite materials [15] and molecular Mott insulators [16]. Charge-transfer (CT) systems (introduced in Chapters 1 and 6) are also often subject to phase transitions as a function of temperature and pressure, resulting in changes in the electrical properties at a critical temperature or pressure. Examples include metal-insulator transitions, neutral-ionic transitions, Peierls transitions, and transitions to a ferroelectric state [17,18]. Historically, these complexes were of interest due to the prediction of room-temperature superconductivity or metallic conductivity [19]; more recently, they have proven to be an excellent medium for the study of novel applications-oriented properties such as photoconductivity, tunable semiconductivity, ferroelectricity, magnetoresistance, and field emission [7,11,20,21].

In the second part of this Chapter, we provide a theoretical description of the transition in the charge carrier mobility observed in an organic field-effect transistor based on the STB-F_4TCNQ (STB = stilbene, F_4TCNQ = 2,3,5,6-tetrafluoro-7,7,8,8-tetracyanoquinodimethane) DA complex (Figure 7.2). We discuss several lattice vibrations that can be relevant to the transition. Several possible mechanisms of the phase transition are also discussed. These results were published in *Nature Communications* [22].
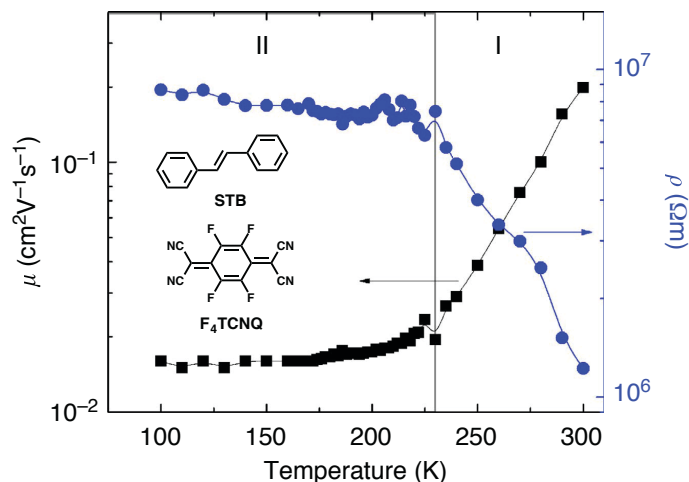
Figure 7.2 Temperature dependence of the mobility (μ) and resistivity (ρ) in an STB-F₄TCNQ transistor. Region I marks an activated transport regime, whereas region II marks a temperature-independent transport regime [22].

7.2 Computational methodology

Electronic-structure calculations on anthracene-PMDA [23] have been performed on the basis of both experimental and optimized crystal structures. During the optimization, the positions of the atoms in the unit cell were relaxed, while the cell parameters were kept fixed at the experimental values. Similarly to our previous study [24], the impact of the HF exchange has been investigated by using the αPBE functional, based on the original PBE functional [25,26], following a simple hybrid scheme proposed by Adamo and Barone [27]:

$$E_{\alpha PBE} = \alpha E_X^{HF} + (1 - \alpha)E_X^{PBE} + E_C^{PBE} \tag{7.1}$$

where α = 0.25 corresponds to the PBE0 functional.

For periodic electronic-structure calculations, the Brillouin zone was sampled using a Γ-centered uniform *k*-point 8x6x8 grid. The Γ-point phonons (lattice vibrations),

macroscopic dielectric tensors, and IR and Raman intensities were obtained via a coupled perturbed Hartree-Fock (CPHF) approach [28,29]. All these calculations were performed using the αPBE functional and 6-31G basis set in the CRYSTAL14 package [30]. The effective masses and their orientations were calculated by diagonalizing the inverse of the effective mass tensor ($1/m_{ij}$). The latter was obtained from the valence band maximum or conduction band minimum using a finite-difference method on a five-point stencil with a 0.01 1/Bohr step. G_0W_0 calculations were performed using the BerkeleyGW code [31], starting from the PBE-derived wavefunctions and energies obtained from Quantum-ESPRESSO [32] with norm-conserving Troullier-Martins pseudopotentials [33]. Direct electronic couplings (t_{DA}) between anthracene and PMDA molecules along the stacking direction are obtained using the fragment orbital approach [34]. The effective electron [hole] electronic couplings (t_{eff}) were evaluated using the energy-splitting approach by considering the frontier levels of an A-D-A [D-A-D] triad (see Chapter 6) [35]. All electronic couplings were calculated at the αPBE/6-31G level using the Gaussian package [36]. All lattice vibrations can be visualized on the Internet [http://afonari.com/ant-pmda-vibrations/index-ir.html and http://afonari.com/ant-pmda-vibrations/index-raman.html].

Geometry optimizations of the crystal structures of STB-F_4TCNQ at different temperatures were performed at the B3LYP/6-31G level of theory. During the optimizations, the unit-cell parameters were kept fixed at the experimental values. A uniform 6x8x4 Monkhorst-Pack k-point grid was employed. Effective masses were obtained by diagonalizing the inverse effective mass tensor. Energy derivatives with respect to the k-point, that form a tensor, were evaluated using the finite-difference

method with 0.01 Bohr^{-1} steps. The Γ-point phonon modes were obtained using the finite-difference method with a 0.003 Å atomic displacement step. These calculations were carried out using the CRYSTAL09 package [37]. Transfer integrals (electronic couplings) between the HOMO of stilbene and the LUMO of F$_4$TCNQ were calculated at the B3LYP/6-31G(d,p) level using a fragment orbital approach in combination with a basis set orthogonalization procedure [34] as implemented in the development version of the NWChem package [38].

7.3 Results and discussion

7.3.1 Impact of exact exchange in the description of the vibrational properties of anthracene-PMDA

7.3.1.1 Electronic structure

We first discuss the impact that the HF exchange has on the band structure in the anthracene-PMDA crystal based on the experimental geometry. The calculations using an amount of the HF exchange larger than 35% face convergence difficulties; therefore, we only discuss here the results obtained within the 0–35% range of HF exchange. We note that (semi)local DFT functionals underestimate the band gaps [39]; as a result, the calculations based on functionals with a low amount of HF exchange predict a vanishing band gap for many CT crystals, as was shown, for instance, in the case of DBTTF-TCNQ [24] and TTF-CA [40]. For anthracene-PMDA, a nonzero gap is obtained even using the pure PBE (α=0) functional. For the investigated HF exchange range, in agreement with previous findings for other crystals [24,41], the band gap shows a linear increase (R^2=0.999) by a factor of almost 3 from 0.94 eV to 2.68 eV. In contrast, only a very

slight increase of about 0.044 eV and 0.031 eV is obtained for the valence and conduction bandwidths, respectively. As a result, the decrease in the smallest component of the hole [electron] effective mass calculated at Γ [Y] point is also very small and varies from 1.156 m_0 to 1.093 m_0 [from 1.123 to 1.084 m_0] (Table 7.1) with the increase in HF exchange from 0 to 35%. We recall that such slight evolutions of the bandwidths and effective masses with respect to the degree of HF exchange are the result of the superexchange nature of the effective electronic couplings for holes and electrons in CT crystals [24,35]. Indeed while direct donor-acceptor couplings within the investigated HF exchange range show a 50% increase from 0.300 to 0.452 eV, both effective hole and electron transfer integrals increase only slightly from 0.048 to 0.053 eV and 0.046 to 0.053 eV, respectively.

Similarly to our previous work, we employed the calculations within the G_0W_0 approach [42,43] in order to calibrate the amount of HF exchange needed for reliable estimation of the band gap and bandwidths in anthracene-PMDA. A linear extrapolation of the αPBE results suggests that approximately 45% of the amount of HF exchange would be needed to reproduce the G_0W_0 band gap. This value is much larger than the values of 32% and 33% we have previously found for the pentacene and DBTTF-TCNQ crystals. However, as a result of the weak dependence of the bandwidths on HF exchange, a good agreement with the G_0W_0 results for the valence and conduction bandwidths is obtained even when using a pure functional (with 0% amount of HF exchange).

Table 7.1 Fundamental gap, valence and conduction bandwidths (VBW, CBW), effective electronic couplings, and smallest hole and electron effective masses (m_{Hole}, m_{El}) for the anthracene-PMDA crystal at the experimental geometry.

	0% HFE	25% HFE	35% HFE	G_0W_0
E_{gap}, eV	0.941	2.143	2.682	3.326
VBW, eV	0.328	0.365	0.372	0.351
CBW, eV	0.209	0.233	0.240	0.212
t_{hole}^{eff}, eV	0.048	0.052	0.053	-
t_{el}^{eff}, eV	0.046	0.051	0.053	-
t_{DA}, eV	0.300	0.445	0.452	-
m_{Hole}, m_0	1.156	1.110	1.093	-
m_{El}, m_0	1.123	1.097	1.084	-
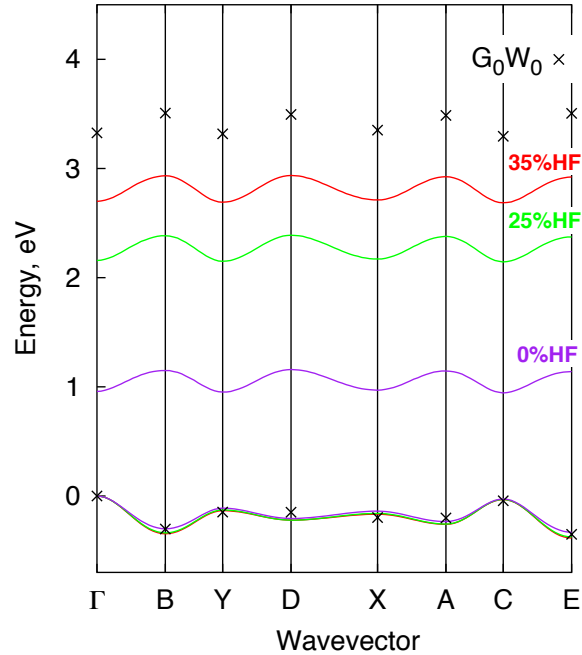
Figure 7.3 Valence and conduction bands of anthracene-PMDA obtained using the αPBE functional with different amounts of HF exchange (solid lines), and G_0W_0 (crosses). The points of high symmetry in the first Brillouin zone are labeled as follows: Γ = (0,0,0), X = (0.5,0,0), Y = (0,0.5,0), B = (0,0,0.5), C = (0.5,0.5,0), A = (0.5,0,0.5), E = (0.5,0.5,0.5), and D = (0,0.5,0.5), all in crystallographic coordinates.

7.3.1.2 Crystal structure

We now turn our attention to the comparison of the optimized geometries obtained using different amounts of HF exchange in the αPBE functional. Table 7.2 lists the deviations of the individual atoms in an optimized structure from the experimental geometry, as well as the weighted root-mean-square deviations for all atoms in the unit cell. The largest deviation is obtained for C=O groups although it does not exceed 0.1 Å (Figure 7.4). The remainder of the molecular complex is less floppy due to aromaticity. The weighted root-mean-square deviations obtained for the calculations using different amounts of HF exchange do not exceed 0.04 Å, which suggests that any αPBE functional captures well both intra- and inter-molecular interactions for this crystal. In order to understand the effect that geometry has on the electronic and charge-transport properties, we computed the electronic couplings, band gaps, and bandwidths using αPBE with 25% HF exchange for all optimized geometries. The average value and standard deviation of the effective hole [electron] coupling is 0.057±0.005 eV [0.056±0.004 eV]. As a result, the average value and standard deviation of valence [conduction] bandwidth are 0.393±0.029 eV [0.271±0.021 eV]. These values are larger compared to the values obtained using the experimental geometry. The opposite trend is observed for the band gap for which the average value and standard deviation are 1.862±0.139 eV. Standard deviation in all cases is one order of magnitude smaller than the average value, which points to the fact that optimized geometries obtained using different amounts of HF exchange have similar electronic properties. Since the residual factor (R-factor) for the crystal structure is 4.6% [44], indicating a good agreement between the crystallographic model and experimental electron density, we use the experimental unit-cell parameters in this study.
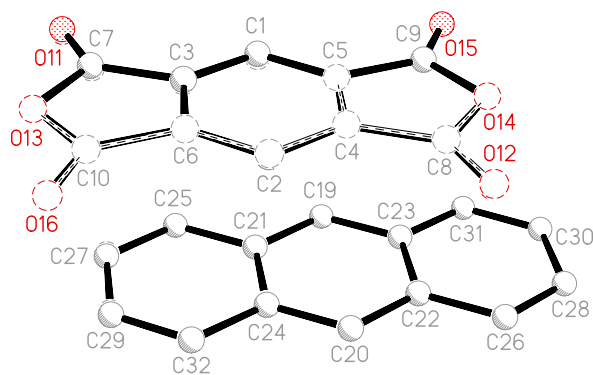
Figure 7.4 Calculated geometry of anthracene-PMDA obtained using pure PBE functional (dashed lines) overlapped on experimental geometry (solid lines). Hydrogen atoms are omitted for clarity.

Table 7.2 Deviations of individual heavy atoms (Å) and root-mean-square deviations (RMSD, Å) of optimized crystal geometries fitted to experimental geometry. For atomic labels, refer to Figure 7.4.

Atoms	0 %HF	25 %HF	35 %HF
C1	0.032	0.046	0.050
C2	0.032	0.039	0.040
C3	0.029	0.031	0.033
C4	0.038	0.031	0.028
C5	0.021	0.013	0.015
C6	0.024	0.021	0.022
C7	0.050	0.044	0.046
C8	0.062	0.050	0.046
C9	0.016	0.018	0.026
C10	0.033	0.039	0.043
O11	0.074	0.058	0.059
O12	0.090	0.072	0.066
O13	0.040	0.025	0.032
O14	0.046	0.018	0.017
O15	0.073	0.046	0.048
O16	0.073	0.066	0.066
C19	0.019	0.015	0.014
C20	0.009	0.023	0.028
C21	0.024	0.026	0.028
C22	0.014	0.010	0.013
C23	0.020	0.012	0.008
C24	0.011	0.024	0.029
C25	0.028	0.031	0.036
C26	0.024	0.019	0.023
C27	0.036	0.039	0.048
C28	0.035	0.017	0.022
C29	0.030	0.041	0.050
C30	0.029	0.010	0.015
C31	0.022	0.006	0.007
C32	0.013	0.033	0.042
RMSD	0.0397	0.0350	0.0371

Table 7.3 Fundamental gap, valence and conduction bandwidths (VBW, CBW), direct and effective electronic couplings calculated based on the optimized anthracene-PMDA geometry obtained using different amounts of HF exchange (HFE). Single-point calculations on optimized geometries are performed using αPBE with 25% HFE. All values are in eV.

% HFE	E_{gap}	VBW	CBW	t_{hole}^{eff}	t_{el}^{eff}	t_{DA}
0	1.705	0.426	0.294	0.062	0.061	0.471
25	1.909	0.382	0.268	0.055	0.055	0.455
35	1.971	0.372	0.252	0.053	0.053	0.450

7.3.1.3 Γ-point vibrational modes

The DFT estimates for the low-energy (0–300 cm^{-1}) Raman active and IR active modes of the anthracene-PMDA crystal are given in Tables 7.4 and 7.5, respectively. It is a common practice to scale calculated frequencies in order to better match the experimental values. It was also previously shown that the scaling factor depends on the amount of HF exchange included in the functional [45-48]. Here, we calculated the optimal scaling factors (λ^{α}) using the least-square method [48]:

$$\lambda^{\alpha} = \sum_i^{all} \omega_{i,calc}^{\alpha}\omega_{exp} / \sum_i^{all}(\omega_{i,calc}^{\alpha})^2, \qquad (7.2)$$

where $\omega_{i,calc}^{\alpha}$ and ω_{exp} denote calculated and experimental frequencies, respectively. Frequencies obtained using αPBE functionals with 0, 25, and 35 % HF exchange, were scaled by the derived scaling factors: 1.0056, 0.9602, and 0.9449. An inverse relation between the amount of HF exchange and the scaling factor values has been reported in several studies [45-48]. In what follows, we discuss only the scaled frequencies. The experimental Raman data (Figure 7.5, Table 7.4) agree very well with a previously reported spectrum measured at 2K (Table 7.4) [23]. Comparing the performance of the αPBE functionals within this frequency region, we note that both hybrid functionals with

α equal to 25 and 35 only slightly outperform the pure functional (0% HF exchange) in terms of matching the computed and experimental frequencies (Table 7.4). Root-mean-square deviations for this frequency region do not exceed 6 wavenumbers for any α value. This is to be expected, since the frequencies (besides the linear scaling factor) are obtained from forces based on the ground-state density, which is not strongly affected by the inclusion of the HF exchange. However, in the case of off-resonance Raman spectra, when we consider the peak intensities, the hybrid functionals clearly outperform the PBE functional; indeed intensities are related to the variation of the macroscopic dielectric tensor [49], which strongly depends on the amount of HF exchange included in the functional.

We turn now to the assignment of the vibration modes. According to the computed normal-mode patterns (Figure 7.6), the first six Raman-active phonons in the 0–130 cm^{-1} region can be assigned as pure librations (rigid-body rotations) [23]. In particular, the two lowest librations (43 and 47 cm^{-1}) correspond to in-phase and out-of-phase in-plane rotations around the axis perpendicular to the molecular plane. The next two librations (57 and 87 cm^{-1}) correspond to PMDA rotations around the short and long molecular axes. We attribute the two highest-energy librations to the rotations of anthracene around the long molecular axis. Our assignments are in agreement with previous suggestions [23], based on the molecular moments of inertia. Higher-frequency vibrations in the 140–300 cm^{-1} region are mostly related to intra-molecular motions. In particular, the experimental peaks at 178, 208, 253, 273 cm^{-1} are related to bending of C=O/C-O-C groups and central ring of PMDA; the measured peak at 254 cm^{-1} is related to the skeletal

bend of anthracene; the experimental peaks at 279 and 280 cm^{-1} are related to a combination of skeletal bends of anthracene and PMDA.
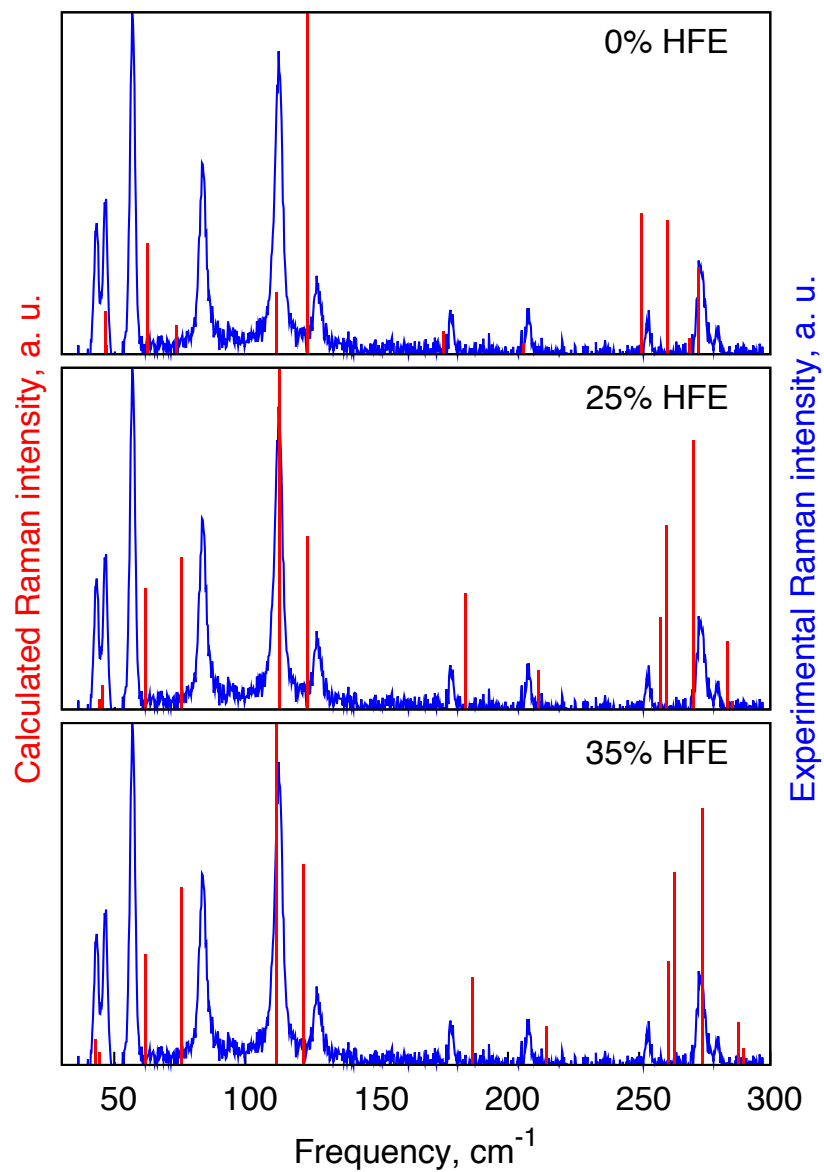
Figure 7.5 Low-frequency simulated (red bars) and experimental (blue lines) Raman spectra.
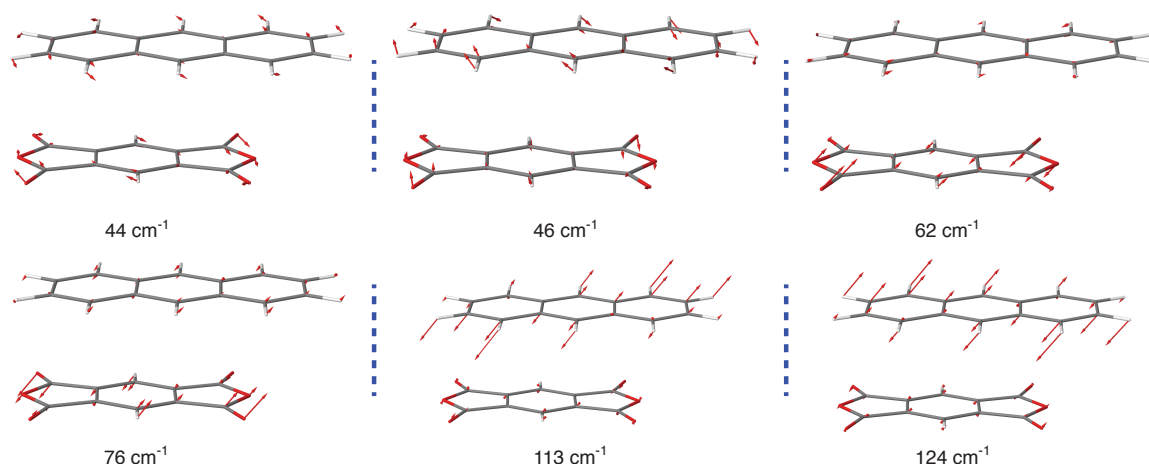
Figure 7.6 Eigenvectors of the inter-molecular lattice vibrations in the anthracene-PMDA crystal. Only one donor-acceptor complex is shown for clarity.

Table 7.4 Calculated and experimental low-frequency Raman-active phonons (cm^{-1}) in the anthracene-PMDA crystal. L denotes libration, A – anthracene, P – PMDA.

Exp.	Exp. [a]	0% HFE	25% HFE	35% HFE	Assignment
43	45	49	44	42	(L) A/P: Out-of-phase in-plane rotation around the z-axis
47	49	49	46	43	(L) A/P: In-phase in-plane rotation around the z-axis
57	58	65	62	61	(L) P: Rotation around short axis
83	86	77	76	74	(L) P: Rotation around long axis
113	115	117	113	110	(L) A: Rotation around long axis
127	130	130	124	120	(L) A: Rotation around long axis
178	-	184	184	184	P: C=O/C-O-C out-of-plane bend
208	-	216	212	211	P: ring stretch/C=O out-of-plane bend
253	-	263	258	257	P: ring stretch/C=O out-of-plane bend
254	-	263	260	259	A: out-of-plane skeletal bend
273	-	273	271	270	P: ring breath/C=O out-of-plane bend
279	-	282	284	283	A/P: skeletal bend
280	-	285	286	285	A/P: skeletal bend
RMSD		6	5	5	

[a] Experimental Raman spectra of the anthracene-PMDA crystal below 140 cm^{-1} measured with 630 nm excitation wavelength at 2 K [23].

The DFT results for the IR-active modes in the 0–300 cm^{-1} region are listed in Table 7.5. Since the displacement patterns of the modes obtained with 0, 25, and 35 percent of the HF exchange are similar, below we only discuss modes obtained using 25 %HF exchange (Figure 7.7). In the case of IR-active low-frequency modes, the lowest two modes can be described as mixture of librations and translations. These modes correspond to out-of-phase translation of anthracene and PMDA along the short molecular axis (54 cm^{-1}) and out-of-phase translation along the stacking direction (74 cm^{-1}). The latter results in a decrease in intra-stack π-stacking distance. The next two modes are described by a translation of anthracene along the stacking direction (89 cm^{-1}) and bending of the C=O group in the PMDA molecule (103 cm^{-1}). The following modes completely lack any librational character. In particular, the next two modes are described by in-phase (125 cm^{-1}) and out-of-phase (145 cm^{-1}) skeletal bending of both anthracene and PMDA, which facilitates intra-stack π-stacking. Similarly, the next two modes are associated with in-phase (164 cm^{-1}) and out-of-phase (172 cm^{-1}) skeletal twists of the donor-acceptor complex.

Table 7.5 Calculated low-frequency IR-active phonons (cm^{-1}) of the anthracene-PMDA crystal.

0 %HF	25 %HF	35 %HF	Assignment
60	54	51	(L) A/P: Out-of-phase translation along short axis
82	74	70	(L) A/P: Out-of-phase translation along z-axis
92	89	88	A: Out-of-phase translation along z-axis / P: C=O out-of-plane bend
107	103	101	A: In-phase translation along z-axis / P: C=O out-of-plane bend
124	125	124	A/P: In-phase out-of-plane skeletal bend
146	145	144	A/P: Out-of-phase out-of-plane skeletal bend
166	164	162	A/P: In-phase out-of-plane skeletal twist
175	172	170	A/P: Out-of-phase out-of-plane skeletal twist
184	184	184	P: C=O/C-O-C out-of-plane bend
239	235	233	A: In-plane ring bend
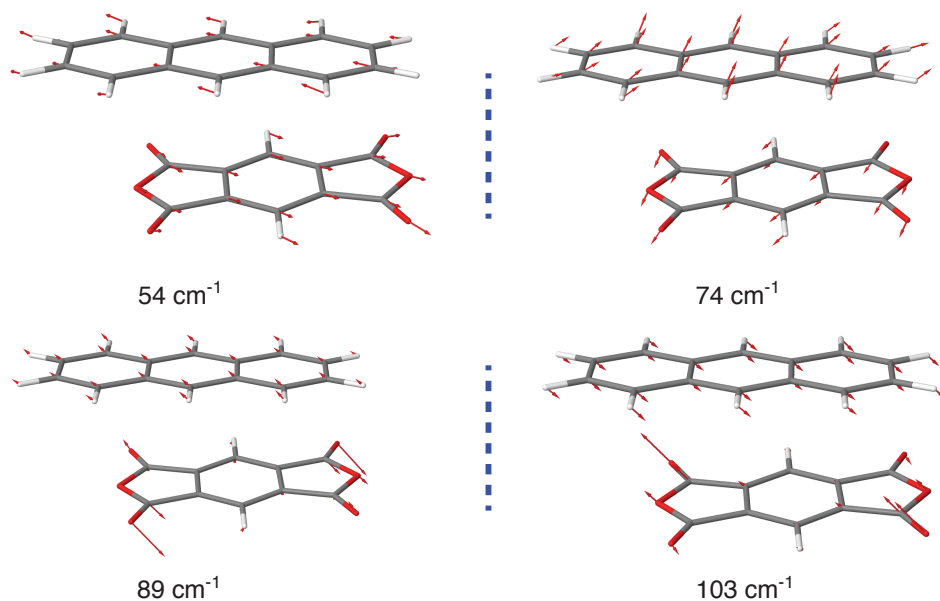
Figure 7.7 Eigenvectors of the IR-active low-frequency vibrations in the anthracene-PMDA crystal as obtained using 25% HF exchange. Only one donor-acceptor complex is shown for clarity.

In the high-frequency region (300–2000 cm^{-1}), the crystal vibrations possess an intra-molecular character. Comparing the performance of the functionals with different amounts of HF exchange, similarly to the low-frequency region, both hybrid functionals (α=25, α=35) only slightly outperform the pure PBE functional. The root-mean-square deviations for this frequency region do not exceed 60 wavenumbers for different α values.

7.3.1.2 Electron-phonon coupling

In order to quantify the effect of lattice vibrations on the electronic couplings between donor and acceptor molecules along the molecular stacks (t_{DA}, see Figure 7.1), we evaluated the nonlocal electron-phonon (e-ph) coupling constants (v) and related nonlocal e-ph relaxation energies (L) defined as [50]:

$$v_i = \frac{dt_{DA}}{dQ_i} \tag{7.3}$$

$$L = \sum_i \frac{v_i^2}{2\hbar\omega_i}. \tag{7.4}$$

Here, Q_i is the normal-mode coordinate of mode i with frequency ω_i. The nonlocal coupling constants resulting from the low-frequency vibrations (0–300 cm^{-1}) obtained with various amounts of HF exchange using the optimized geometry, and the normal modes obtained with 25% HF exchange are listed in Table 7.6. The modes in this region contribute to the relaxation energy by 92%, 90%, and 85% when α is equal to 0, 25, and 35, respectively. This is in agreement with previous studies on both single-component (oligoacenes [51], rubrene [52]) and binary CT crystals [4]. Both IR and Raman-active modes contribute to the electron-vibration interactions. The IR-active lattice vibrations with frequencies of 74 and 125 cm^{-1} have the largest coupling constants. Both modes are described by a decrease in π-stacking distance either due to translation along the z-axis or in-phase out-of-plane skeletal bend, respectively (Table 7.6). The Raman-active librations at 46 and 62 cm^{-1}, described by anthracene/PMDA in-phase in-plane rotation around the z-axis and PMDA rotation around the short axis, also contribute significantly to the nonlocal coupling. For the majority of the modes, the coupling constants show a close-to-linear dependence on the amount HF exchange. However, a few modes, in particular the 76, 164, 184, and 260 cm^{-1} modes, exhibit a more complicated dependence. Overall, both t_{DA} and L are increasing with the increase in the amount of HF exchange. However, L increases at a higher pace; as a result, the L/t_{DA} ratio changes from 0.16 to 0.25 within the 0–35% HF exchange range. Similar ratios were reported for previously investigated mixed-stack CT crystals [4].

Table 7.6. Nonlocal coupling constants (v, meV), relaxation energies (L, meV), and transfer integrals (t_{DA}, meV) calculated as a function of the amount of HFE, based on the normal modes obtained using 25% HF exchange (HFE).

Active	Freq., cm^{-1}	v		
		0% HFE	25% HFE	35% HFE
R	44	0.21	1.00	1.21
R	46	-4.00	-8.79	-10.93
IR	54	3.29	5.50	6.36
R	62	-9.50	-10.43	-13.79
IR	74	-17.43	-27.36	-29.14
R	76	6.21	9.64	8.21
IR	89	-6.07	-8.86	-10.00
IR	103	7.71	12.57	14.07
R	113	6.50	10.57	12.50
R	124	-1.29	-1.57	-2.64
IR	125	-13.57	-20.29	-20.64
IR	145	1.79	1.64	0.21
IR	164	-1.93	-3.21	-3.21
IR	172	2.14	4.64	6.14
R	184	1.71	8.07	13.43
IR	184	-4.21	-5.71	-5.29
R	212	2.36	4.36	5.36
IR	235	-2.57	-4.14	-4.36
R	258	-1.43	2.43	6.86
R	260	0.29	0.29	-0.36
R	271	-1.07	-0.79	-0.50
R	284	1.57	-1.36	-4.14
R	286	-0.36	-2.07	-3.36

	0% HFE	25% HFE	35% HFE
L	41 / 92%	100 / 90%	117 / 85%
t_{DA}	258	455	477
L/t_{DA}	0.16	0.22	0.25

Interestingly, when the electron-vibration couplings and transfer integrals are computed with the same αPBE functional as that used to obtain the optimized geometry and normal modes, then, as seen from Table 7.7, L/t_{DA} is about 0.2 and is basically independent of the amount of HF exchange.

Table 7.7 Nonlocal relaxation energies, L (meV), and transfer integrals, t_{DA} (meV) calculated as a function of the amount of HF exchange (HFE), based on the normal modes derived with the corresponding amount of HF exchange.

	0% HFE	25% HFE	35% HFE
L_{total}	51	100	103
t_{DA}	259	455	468
L_{total}/t_{DA}	0.20	0.22	0.22

7.3.2 Crossover from thermally-activated to temperature-independent transport in stilbene-F$_4$TCNQ charge-transfer semiconductor

7.3.2.1 Structure and thermodynamics

Stilbene and related compounds have been the subject of intense research scrutiny for a number of years. In particular, static and dynamical disorders are known to play a significant role in the structure and properties of stilbene-containing compounds. Single-crystal XRD measurements of neat STB and the CT complex STB-TCNQ show that the STB molecule can adopt two orientations that are related to one another by a twofold rotation about the longest molecular axis [53-55]. The librational motion responsible for the interconversion between these two conformers can be viewed as a rotation of the central C=C stilbene moiety at fixed orientation of the benzene rings relative to the crystal lattice and is referred to as a pedal-like (crankshaft) motion. In the neat STB crystal, this motion results in an orientational disorder [56,57]. Variable-temperature

structural studies indicate that this disorder is dynamic, *i.e.*, the conformational interconversion is temperature dependent (and as a result the conformer populations are as well), with the occupancy factor of the minor, energetically unfavorable conformer decreasing as the temperature is lowered [57,58]. Below 170 K, the pedal motion becomes inactive and thus the conformational disorder does not undergo any significant changes. The population of the minor conformer present at low temperatures can be increased by increasing the cooling rate, but always remains very low (<10% for flash-cooled crystals and <5% for slow-cooled crystals). Freezing of the conformational changes generates thermodynamic non-equilibrium states that persist below the transition temperature and represents the signature of a glass-like transition. The anomaly observed in calorimetric measurements at 170 K in STB was therefore attributed to this glass-like transition due to the freezing of the crankshaft motion [59]. It is important to note that the potential energy along the torsional coordinate connecting the two conformers of the stilbene molecules can be described by a double-well potential. The ensembles of systems described by such energy potentials are well-known models for glasses [60,61].

In addition to these observations in neat STB, thermodynamic transitions are also found in calorimetry measurements of CT complexes of STB, near 250 K in STB-TCNQ and near 240 K in STB-F4TCNQ (Figure 7.8) [62]. The transitions are similar in shape to that seen in neat stilbene and have therefore been interpreted as caused by the freezing of the crankshaft motion; however, these materials have not been reported to exhibit temperature-dependent changes in conformer populations as stilbene does. In the CT complexes, while the C=C bond undergoes a similar librational motion, a quantitative

analysis of the conformational interconversion was not possible under regular laboratory conditions. Indeed, the temperature-dependent STB-F$_4$TCNQ structure determination indicates that the disorder is low and the population of the minor conformer is below 5% at all temperatures [22]. These results are in agreement with those of Saito *et al.* [62] who concluded based on heat capacity measurements that while there is disorder present in STB-F$_4$TCNQ, the population of the misoriented STB molecules is <10%, even at room temperature. The lack of significant changes in the crystal structure as the system passes through the transition temperature coupled with the stepped-like feature in the heat capacity measurements are clear signatures of a glass-type transition [63]. As a result, the mechanism for the observed transition in the transport properties of the STB-F$_4$TCNQ crystal seems to be related to the transition into a glassy crystal, where the constituent STB molecules exhibit freezing of the orientational disorder and the thermal equilibrium is no longer attained.

7.3.2.2 Temperature dependence of effective masses and electronic couplings

To determine the nature of the transition, the crystal structure of the CT complex as a function of temperature was evaluated using XRD by our collaborators from Wake Forest University. The temperature dependence of the STB-F$_4$TCNQ lattice parameters is plotted in Figure 7.9. At all investigated temperatures, the system crystallizes in the monoclinic space group *P2$_1$/n* with two STB molecules and two F$_4$TCNQ molecules per unit cell, each located at an inversion center. Molecules pack in a mixed-stack fashion, in which donor and acceptor molecules alternate along a stack (Figure 7.8).
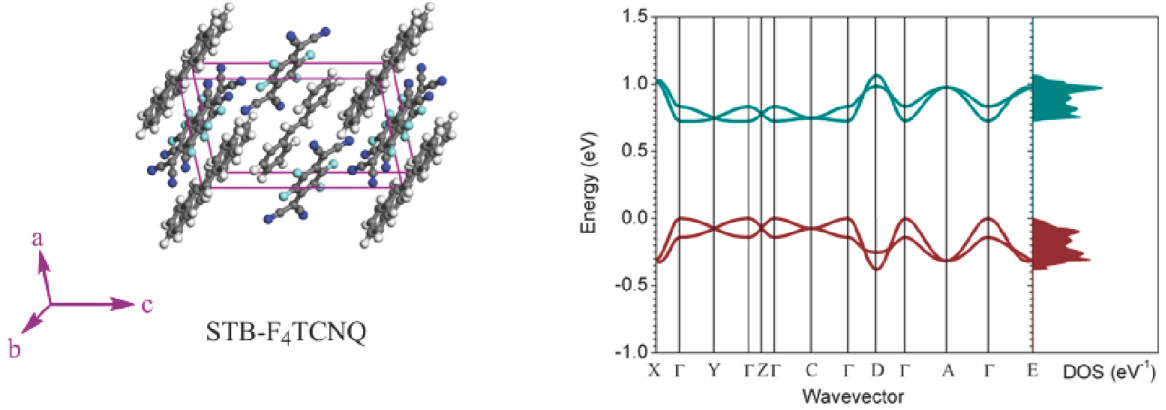
Figure 7.8 Crystal packing and band structure of the STB-F$_4$TCNQ crystal [4]. The points of high symmetry in the first Brillouin zone are labeled as follows: Γ = (0, 0, 0); X = (0.5, 0, 0); Y = (0, 0.5, 0); Z = (0, 0, 0.5); V, A = (0.5, 0.5, 0); U, D = (0.5, 0, 0.5); T, C = (0, 0.5, 0.5), and R, E = (0.5, 0.5, 0.5), all in crystallographic coordinates. The zero of energy is given at the top of the valence band. Taken from Ref. [4].

The unit cell varies by the expected linear thermal expansion: 1.1% along all three unit-cell axes and 3.1% for the total unit cell volume, with no evidence of the presence of a structural phase transition. Subsequently, based on the temperature-dependent structures, we have performed band-structure calculations and evaluated the effective masses for both holes and electrons. The results are shown in Figure 7.8. Effective masses, evaluated al low temperature, are in good agreement with those previously reported by our research group [4]. Our calculations indicate that charge carriers have small effective masses only along the stacking directions, and that both hole and electron effective masses increase systematically with the temperature increase. This dependence is consistent with the linear thermal expansion of the crystal. As the cell parameters increase, the distance between the STB and F$_4$TCNQ molecules also increases. Consequently, the calculations suggest that the transfer integral (t_{HL}) from the HOMO (highest occupied molecular orbital) of STB to the LUMO (lowest unoccupied molecular orbital) of the neighboring F$_4$TCNQ molecule decreases, resulting in an increase in the effective mass of both holes

and electrons. Thus, the temperature dependence of the transfer integrals and effective masses derived from the static structure are not able to provide an explanation for the features observed at T=235 K in the electrical measurements.
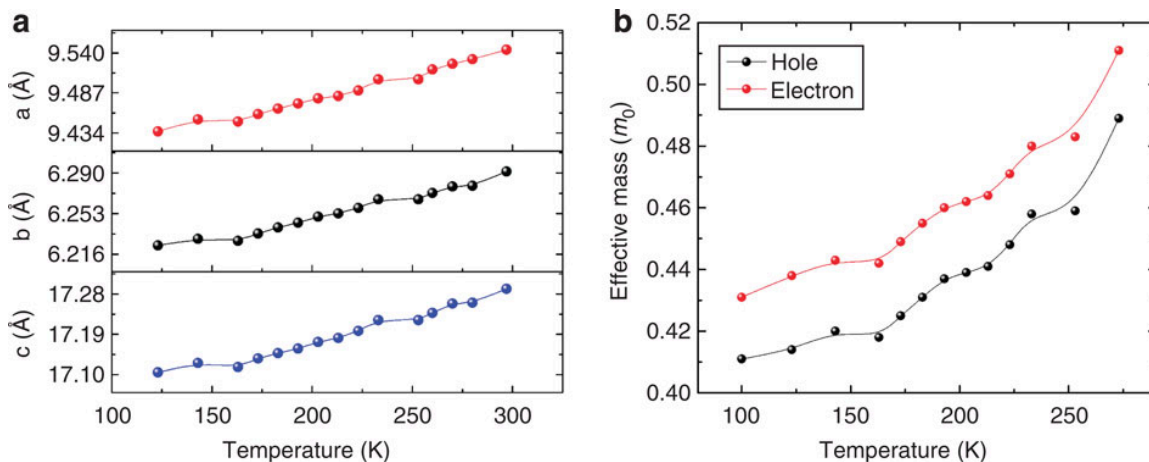
Figure 7.9 The temperature dependence of properties of the charge-transfer complex: (a) Temperature dependence of the lattice parameters of STB-F$_4$TCNQ; the lattice expansion is approximately linear with temperature. (b) Temperature dependence of the smallest component of the effective masses of holes and electrons as derived from band-structure calculations using the lattice parameters. Obtained at B3LYP/6-31G level of theory. Taken from Ref. [22].

7.3.2.3 Impact of the libration modes on the charge transport characteristics

The calculations of the Γ-point phonons indicate that there are two vibrational modes with frequencies of 279 cm^{-1} and 285 cm^{-1} (Figure 7.10) related to the libration of the STB bridge. As seen from the eigenvectors, the benzene rings are not involved in these modes, that is, these *librations* occur along the crankshaft trajectory.
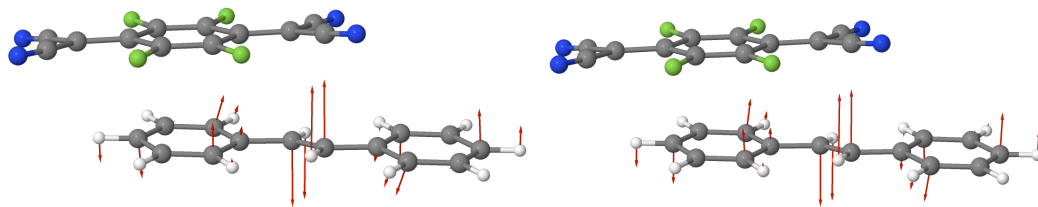
Figure 7.10 Phonon eigendisplacements of the 279 (left) and 285 (right) cm^{-1} modes. Obtained at B3LYP/6-31G level of theory. Only one donor-acceptor complex from the unit cell is shown. Taken from Ref. [22].

The observed transition between temperature-independent and activated transport can be related to these normal modes, in particular, in terms of the non-local (Peierls) electron–phonon coupling (*i.e.*, the dependence of the transfer integrals on the displacements of the phonon modes) [12]. The transfer integral t_{HL} computed as a function of the phonon displacements of the librational modes discussed above is shown in Figure 7.11.
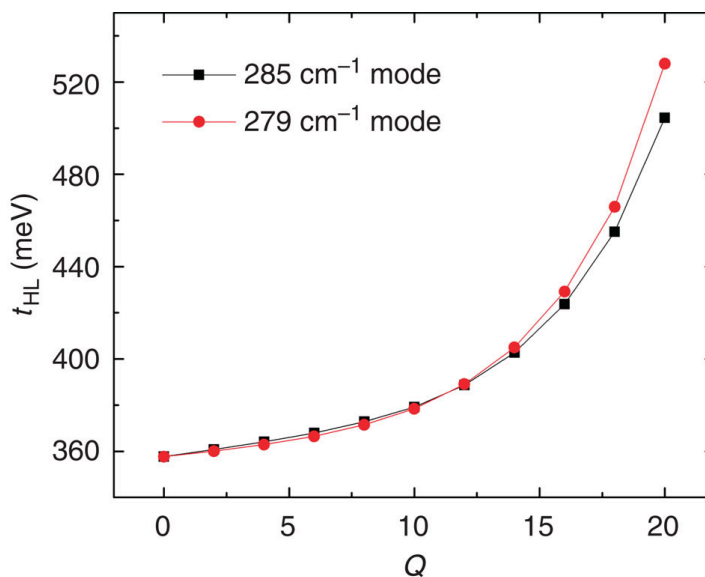
Figure 7.11 Transfer integral dependence on the phonon displacements. The phonon displacements, Q, are given in dimensionless units. Obtained at B3LYP/6-31G level of theory. Taken from Ref. [22].

For small phonon displacements, t_{HL} shows the expected linear behavior [50]. However, for larger displacements, such as those expected above the transition temperature, t_{HL} exhibits a significant non-linear increase. Therefore, the increase in transfer integrals due to these librations surpasses the decrease related to thermal expansion, leading to an overall increase of t_{HL} with the temperature increase. Our model is thus fully consistent with the experimental observations.

7.3.2.4 Nature of the activation behavior of mobility

With a better understanding of the dynamics of the librational motion as a function of temperature, we can now try to describe the mechanism that can explain the evolution of the electrical properties of the STB-F_4TCNQ crystals. One possible explanation for the crossover from tunnelling (and therefore temperature independence) at low temperatures to activated charge transport at higher temperatures invokes the interaction with local electron–phonon coupling (modulation of the site energies by vibrations, also known as the Holstein small polaron model) [12,64]. The Holstein polaron binding energy (E_{pol}) of 0.14 eV previously reported for STB-F_4TCNQ [4], however, results in an activation energy (E_a) of 0.07 eV ($E_a = E_{pol}/2$), which is significantly smaller than the observed activation energy of 0.17 eV [4]. We note that the above estimation of the E_{pol} and E_a is based on the coupling with intramolecular vibrations only; thus, the contribution due to the electron-phonon interactions with intermolecular vibrations (lattice phonons) is neglected. Although the latter contribution to Holstein polaron binding energy is believed to be small in single-component systems, it may be different in the case of CT complexes. Therefore, while we cannot rule it out, we do not have at this point a clear

evidence that would support the implication of the Holstein-type electron–phonon coupling in the explanation of the observed crossover from temperature-independent to activated transport.

A second possible explanation for the crossover could be related to the nonlocal electron-phonon coupling. This interaction can lead to an increase in transfer integrals and subsequently to an enhancement of the transport properties (phonon assisted) [65]. At the same time, the Peierls-type coupling is a source of dynamical disorder and thus of charge localization [66]. If the former effect, which increases mobility, were to dominate at high temperatures, and the latter effect, which decreases mobility, were to dominate at low temperatures, a crossover in the temperature dependence of transport could result. Our previous results [4] indicate that the Peierls-type polaron binding energy in STB-F_4TCNQ is smaller by an order of magnitude than the electronic coupling; also, it is much smaller than the experimental activation energy observed for the mobility. Therefore, we believe that the Peierls electron-phonon interaction is not the cause of the observed temperature dependence of the transport.

We suggest that the observed transport behavior is due to the double-well potential related to the librational motion of the central STB vinylene bond, which is also responsible for the glass-like transition in STB-F_4TCNQ. At temperatures below the transition, the temperature-independent structural disorder is frozen-in; transport can then take place only via tunnelling within this manifold and is therefore beng temperature independent. At higher temperatures, when the interconversion motion is fast, a transition

to a temperature-activated hopping transport occurs. This model is also supported by measurements performed on analog compounds, which exhibit orientational disorder at low temperatures: for both STB and STB-TCNQ, we observe a clear transition from temperature-independent to activated transport at the same temperature as the glass transition.

7.4 Conclusions

In the first part of this Chapter, we examined the amount of exact Hartree-Fock (HF) exchange to be included in the functional, in order to closely match the G_0W_0 quasi-particle band structure. We showed that, with regard to intensities, the calculated Raman spectrum is significantly improved when using a functional that closely matches the G_0W_0 results for the quasi-particle band structure. Using such a 'tuned' functional, we simulated the IR and Raman spectra of the anthracene-PMDA crystal in the low- and high-frequency regions. The good agreement between the calculated and experimental spectra allowed us to assign the calculated normal modes to peaks in the experimental spectra for both Raman and IR. Finally, we evaluated the dependence of the dynamic transport properties with the amount of HF exchange included in the functional. The nonlocal electron-phonon couplings increase with an increasing amount of HF exchange, as does the lattice relaxation energy, L. However, we found that the ratio t/L remains basically constant in the 0–35 % HF exchange range.

In the second part of this Chapter, we provided a microscopic understanding of the evolution of the charge carrier mobility, which undergoes a crossover from thermally

activated at high temperatures to temperature independent below T=235 K. First, we showed that the transition cannot be understood just on the basis of the static transport properties (effective masses). We identified two lattice vibrations related to the librations of the stilbene molecules; in particular, a non-linear increase in electronic coupling with the increase of the displacement along these two modes were obtained. These modes were also previously suggested to play an important role in the glass-like transition observed in crystals of stilbene complexes. When the libration is large, the structural disorder it leads to, yields a thermally-activated charge transport. At low temperatures, the transport is temperature independent and proceeds via tunneling among the states created by the available conformers that generate the static orientational disorder.

7.5 References

[1]   Sagade, A. A.; Venkata Rao, K.; George, S. J.; Datta, A.; Kulkarni, G. U. *Chemical Communications* **2013**, *49*, 5847.

[2]   Yu, W.; Wang, X.-Y.; Li, J.; Li, Z.-T.; Yan, Y.-K.; Wang, W.; Pei, J. *Chemical Communications* **2013**, *49*, 54.

[3]   Wu, H.-D.; Wang, F.-X.; Xiao, Y.; Pan, G.-B. *Journal of Materials Chemistry C* **2013**, *1*, 2286.

[4]   Zhu, L.; Yi, Y.; Li, Y.; Kim, E.-G.; Coropceanu, V.; Bredas, J. L. *Journal of the American Chemical Society* **2012**, *134*, 2340.

[5]   Zhu, L.; Yi, Y.; Fonari, A.; Corbin, N. S.; Coropceanu, V.; Brédas, J.-L. *Journal of Physical Chemistry C* **2014**, *118*, 14150.

[6]   Horiuchi, S.; Hasegawa, T.; Tokura, Y. *Journal of the Physical Society of Japan* **2006**, *75*, 051016.

[7]   Tatsuo, H.; Jun, T. *Science and Technology of Advanced Materials* **2009**, *10*, 024314.

[8]   Zhang, J.; Geng, H.; Virk, T. S.; Zhao, Y.; Tan, J.; Di, C.-a.; Xu, W.; Singh, K.; Hu, W.; Shuai, Z.; Liu, Y.; Zhu, D. *Advanced Materials* **2012**, *24*, 2603.

[9]   Hasegawa, T.; Mattenberger, K.; Takeya, J.; Batlogg, B. *Physical Review B* **2004**, *69*, 245115.

[10]   Park, S. K.; Varghese, S.; Kim, J. H.; Yoon, S.-J.; Kwon, O. K.; An, B.-K.; Gierschner, J.; Park, S. Y. *Journal of the American Chemical Society* **2013**, *135*, 4757.

[11]   Goetz, K. P.; Vermeulen, D.; Payne, M. E.; Kloc, C.; McNeil, L. E.; Jurchescu, O. D. *Journal of Materials Chemistry C* **2014**, *2*, 3065.

[12]   Coropceanu, V.; Cornil, J.; da Silva Filho, D. A.; Olivier, Y.; Silbey, R.; Bredas, J. L. *Chemical Reviews* **2007**, *107*, 926.

[13]   Sutton, C.; Sears, J. S.; Coropceanu, V.; Bredas, J. L. *The Journal of Physical Chemistry Letters* **2013**, 919.

[14]   Sánchez-Carrera, R. S.; Coropceanu, V.; da Silva Filho, D. A.; Friedlein, R.; Osikowicz, W.; Murdey, R.; Suess, C.; Salaneck, W. R.; Brédas, J.-L. *Journal of Physical Chemistry B* **2006**, *110*, 18904.

[15]   Rini, M.; Tobey, R. a.; Dean, N.; Itatani, J.; Tomioka, Y.; Tokura, Y.; Schoenlein, R. W.; Cavalleri, A. *Nature* **2007**, *449*, 72.

[16]   Kaiser, S.; Clark, S. R.; Nicoletti, D.; Cotugno, G.; Tobey, R. I.; Dean, N.; Lupi, S.; Okamoto, H.; Hasegawa, T.; Jaksch, D.; Cavalleri, A. *Scientific Reports* **2014**, *4*.

[17]   Torrance, J. B. *Molecular Crystals and Liquid Crystals* **1985**, *126*, 55.

[18]   Horiuchi, S.; Tokura, Y. *Nature Materials* **2008**, *7*, 357.

[19]   Little, W. *Physical Review* **1964**, *134*, A1416.

[20]   Kobayashi, K.; Horiuchi, S.; Kumai, R.; Kagawa, F.; Murakami, Y.; Tokura, Y. *Physical Review Letters* **2012**, *108*, 237601.

[21]   Alves, H.; Molinari, A. S.; Xie, H.; Morpurgo, A. F. *Nature Materials* **2008**, *7*, 574.

[22]   Goetz, K. P.; Fonari, A.; Vermeulen, D.; Hu, P.; Jiang, H.; Diemer, P. J.; Ward, J. W.; Payne, M. E.; Day, C. S.; Kloc, C.; Coropceanu, V.; McNeil, L. E.; Jurchescu, O. D. *Nature Communications* **2014**, *5*, 5642.

[23]   Syme, R. W.; Morawitz, H.; Macfarlane, R. M. *Solid State Communications* **1979**, *32*, 1059.

[24]   Fonari, A.; Sutton, C.; Brédas, J.-L.; Coropceanu, V. *Physical Review B* **2014**, *90*, 165205.

[25]   Perdew, J. P.; Burke, K.; Ernzerhof, M. *Physical Review Letters* **1996**, *77*, 3865.

[26]   Perdew, J. P.; Burke, K.; Ernzerhof, M. *Physical Review Letters* **1997**, *78*, 1396.

[27]   Adamo, C.; Barone, V. *The Journal of Chemical Physics* **1999**, *110*, 6158.

[28]   Maschio, L.; Kirtman, B.; Orlando, R.; Rèrat, M. *The Journal of Chemical Physics* **2012**, *137*.

[29]   Maschio, L.; Kirtman, B.; Rerat, M.; Orlando, R.; Dovesi, R. *Journal of Chemical Physics* **2013**, *139*.

[30]   Dovesi, R.; Orlando, R.; Erba, A.; Zicovich-Wilson, C. M.; Civalleri, B.; Casassa, S.; Maschio, L.; Ferrabone, M.; De La Pierre, M.; D'Arco, P.; Noël, Y.; Causà, M.; Rérat, M.; Kirtman, B. *International Journal of Quantum Chemistry* **2014**, *114*, 1287.

[31]   Deslippe, J.; Samsonidze, G.; Strubbe, D. A.; Jain, M.; Cohen, M. L.; Louie, S. G. *Computer Physics Communications* **2012**, *183*, 1269.

[32]   Giannozzi, P.; Baroni, S.; Bonini, N.; Calandra, M.; Car, R.; Cavazzoni, C.; Ceresoli, D.; Chiarotti, G. L.; Cococcioni, M.; Dabo, I.; Corso, A. D.; Gironcoli, S. d.; Fabris, S.; Fratesi, G.; Gebauer, R.; Gerstmann, U.; Gougoussis, C.; Kokalj, A.; Lazzeri, M.; Martin-Samos, L.; Marzari, N.; Mauri, F.; Mazzarello, R.; Paolini, S.; Pasquarello, A.; Paulatto, L.; Sbraccia, C.; Scandolo, S.; Sclauzero, G.; Seitsonen, A. P.; Smogunov, A.; Umari, P.; Wentzcovitch, R. M. *Journal of Physics: Condensed Matter* **2009**, *21*, 395502.

[33]   Troullier, N.; Martins, J. L. *Physical Review B* **1991**, *43*, 1993.

[34]   Valeev, E. F.; Coropceanu, V.; da Silva Filho, D. A.; Salman, S.; Bredas, J. L. *Journal of the American Chemical Society* **2006**, *128*, 9882.

[35]   Zhu, L. Y.; Yi, Y. P.; Li, Y.; Kim, E. G.; Coropceanu, V.; Bredas, J. L. *Journal of the American Chemical Society* **2012**, *134*, 2340.

[36]   Frisch, M. J.; Trucks, G. W.; Schlegel, H. B.; Scuseria, G. E.; Robb, M. A.; Cheeseman, J. R.; Scalmani, G.; Barone, V.; Mennucci, B.; Petersson, G. A.; Nakatsuji, H.; Caricato, M.; Li, X.; Hratchian, H. P.; Izmaylov, A. F.; Bloino, J.; Zheng, G.;

Sonnenberg, J. L.; Hada, M.; Ehara, M.; Toyota, K.; Fukuda, R.; Hasegawa, J.; Ishida, M.; Nakajima, T.; Honda, Y.; Kitao, O.; Nakai, H.; Vreven, T.; Montgomery, J. A.; Peralta, J. E.; Ogliaro, F.; Bearpark, M.; Heyd, J. J.; Brothers, E.; Kudin, K. N.; Staroverov, V. N.; Kobayashi, R.; Normand, J.; Raghavachari, K.; Rendell, A.; Burant, J. C.; Iyengar, S. S.; Tomasi, J.; Cossi, M.; Rega, N.; Millam, J. M.; Klene, M.; Knox, J. E.; Cross, J. B.; Bakken, V.; Adamo, C.; Jaramillo, J.; Gomperts, R.; Stratmann, R. E.; Yazyev, O.; Austin, A. J.; Cammi, R.; Pomelli, C.; Ochterski, J. W.; Martin, R. L.; Morokuma, K.; Zakrzewski, V. G.; Voth, G. A.; Salvador, P.; Dannenberg, J. J.; Dapprich, S.; Daniels, A. D.; Farkas; Foresman, J. B.; Ortiz, J. V.; Cioslowski, J.; Fox, D. J. Wallingford CT, 2009.

[37]   Dovesi, R.; Orlando, R.; Civalleri, B.; Roetti, C.; Saunders, V. R.; Zicovich-Wilson, C. M. *Zeitschrift für Kristallographie - Crystalline Materials* **2005**, *220*, 571.

[38]   Valiev, M.; Bylaska, E. J.; Govind, N.; Kowalski, K.; Straatsma, T. P.; Van Dam, H. J. J.; Wang, D.; Nieplocha, J.; Apra, E.; Windus, T. L.; de Jong, W. A. *Computer Physics Communications* **2010**, *181*, 1477.

[39]   Burke, K. *The Journal of Chemical Physics* **2012**, *136*.

[40]   Giovannetti, G.; Kumar, S.; Stroppa, A.; van den Brink, J.; Picozzi, S. *Physical Review Letters* **2009**, *103*, 266401.

[41]   Refaely-Abramson, S.; Sharifzadeh, S.; Jain, M.; Baer, R.; Neaton, J. B.; Kronik, L. *Physical Review B* **2013**, *88*, 081204.

[42]   Hedin, L. *Physical Review* **1965**, *139*, A796.

[43]   Hybertsen, M. S.; Louie, S. G. *Physical Review B* **1986**, *34*, 5390.

[44]   Boeyens, J. C. A.; Herbstein, F. H. *The Journal of Physical Chemistry* **1965**, *69*, 2160.

[45]   Laury, M. L.; Carlson, M. J.; Wilson, A. K. *Journal of Computational Chemistry* **2012**, *33*, 2380.

[46]   Alecu, I. M.; Zheng, J.; Zhao, Y.; Truhlar, D. G. *Journal of Chemical Theory and Computation* **2010**, *6*, 2872.

[47]   Merrick, J. P.; Moran, D.; Radom, L. *The Journal of Physical Chemistry A* **2007**, *111*, 11683.

[48]   Scott, A. P.; Radom, L. *The Journal of Physical Chemistry* **1996**, *100*, 16502.

[49]   Porezag, D.; Pederson, M. R. *Physical Review B* **1996**, *54*, 7830.

[50]   Coropceanu, V.; Sánchez-Carrera, R. S.; Paramonov, P.; Day, G. M.; Brédas, J.-L. *Journal of Physical Chemistry C* **2009**, *113*, 4679.

[51]   Sánchez-Carrera, R. S.; Paramonov, P.; Day, G. M.; Coropceanu, V.; Bredas, J. L. *Journal of the American Chemical Society* **2010**, *132*, 14437.

[52]   Girlando, A.; Grisanti, L.; Masino, M.; Bilotti, I.; Brillante, A.; Della Valle, R. G.; Venuti, E. *Physical Review B* **2010**, *82*, 035208.

[53]   Bouwstra, J. A.; Schouten, A.; Kroon, J. *Acta Crystallographica Section C* **1984**, *40*, 428.

[54]   Bernstein, J.; Mirsky, K. *Acta Crystallographica Section A* **1978**, *34*, 161.

[55]   Zobel, D.; Ruban, G. *Acta Crystallographica Section B* **1983**, *39*, 638.

[56]   Harada, J.; Ogawa, K. *Journal of the American Chemical Society* **2001**, *123*, 10884.

[57]   Harada, J.; Ogawa, K. *Chemical Society Reviews* **2009**, *38*, 2244.

[58]   Ogawa, K.; Sano, T.; Yoshimura, S.; Takeuchi, Y.; Toriumi, K. *Journal of the American Chemical Society* **1992**, *114*, 1041.

[59]   Saito, K.; Yamamura, Y.; Kikuchi, K.; Ikemoto, I. *Journal of Physics and Chemistry of Solids* **1995**, *56*, 849.

[60]   Anderson, P. W.; Halperin, B. I.; Varma, C. M. *Philosophical Magazine* **1972**, *25*, 1.

[61]   Phillips, W. A. *Journal of Low Temperature Physics* **1973**, *11*, 757.

[62]   Saito, K.; Okada, M.; Akutsu, H.; Sato, A.; Sorai, M. *The Journal of Physical Chemistry B* **2004**, *108*, 1314.

[63]   Suga, H. *Annals of the New York Academy of Sciences* **1986**, *484*, 248.

[64]   Holstein, T. *Annals of Physics* **1959**, *8*, 325.

[65]   Gosar, P.; Choi, S.-i. *Physical Review* **1966**, *150*, 529.

[66]   Troisi, A.; Orlandi, G. *Physical Review Letters* **2006**, *96*, 086601.

CHAPTER 8

CONCLUSIONS

8.1 Synopsis

In this dissertation, we have investigated key static and dynamic transport properties that govern charge transport and charge generation in organic semiconductors. We also assessed the limitations of widely used Density Functional Theory in the description of these parameters. Finally, we provided means to relate these microscopic parameters to spectroscopic observables and other experimentally measurable quantities, such as Raman/IR spectra, transient absorption spectra, electric photoconductivity and charge mobility.

In Chapters 3 and 4, we evaluated microscopic charge-transport parameters in a series of nonlinear acenes. First, it was found that by merging several linear acenes, following Clar's sextet rule, it is possible to design stable nonlinear acenes with an extended π-conjugated core. Extended π-conjugated core improves chances of getting large electronic couplings in condensed phase, provided a favorable stacking arrangement. Second, a combined DFT and MD study of polaron binding energies (E_{pol}) and lattice relaxation energies (L) in these crystals revealed that the formation of self-localized polarons due to local and nonlocal couplings is unlikely. This fact in conjunction with the favorable π-stacking in crystal suggests, that these materials can exhibit band-like transport and are promising organic semiconductors. Hole mobility of one of these

nonlinear acenes was experimentally measured at around 6 cm^2/(Vs) at room temperature in a single-crystal field-effect transistor.

In Chapter 4, we also employed Miller-Abrahams theory of charge hopping due to lattice vibrations in order to describe the variations of experimentally measured electric conductivity due to pulse excitations in the IR region for a photoresistor based on pentacene/C60 thin film. Since an accurate description of the electron-phonon coupling constants requires a precise calculation of lattice vibrations in crystal, we first validated calculated lattice vibrations against experimental IR spectra. This allowed us to depict exact atomic motions (based on the lattice vibration patterns) that strongly modulate photocurrent and thus provide understanding of the phenomena on the microscopic level. This is one of the few examples in the literature where dynamic charge-transport characteristics (nonlocal electron-phonon coupling constants) have been *directly* related to the experimental observables (variations in photoconductivity).

In terms of charge photogeneration from an excited manifold, in Chapter 5, we computed couplings between singlet and triplet excited states and their modulations, due to crystal vibrations, to describe the effect of lattice vibrations on singlet fission in tetracene crystal. We showed that several displacement patterns strongly affect the modulation of the state couplings: displacements that result in the decrease in the distance between herringbone-arranged molecules; and displacements that result into slipped-stack conformations of herringbone-arranged molecules. We also found that the state coupling between localized singlet and correlated triplet states is much stronger affected by the

dynamical disorder due to lattice vibrations, in contrast to the coupling between charge-transfer singlet and triplet state. We validated our methodology against the results from pulse-shaping measurements of the triplet formation in a crystalline thin-film of tetracene.

In Chapter 6, we investigated the impact of Hartree-Fock exchange (HFE) in the description of static (electronic couplings, band gaps, bandwidths, effective masses) transport properties of organic semiconductors. We found that all static transport properties significantly increase in a linear fashion as a function of the amount of the HFE in single-component systems (*i.e.*, pentacene). Whereas in bimolecular donor-acceptor systems, only band gap increases, while bandwidths and effective masses vary only slightly, due to the superexchange nature of the electronic coupling. This underlines the fact that, absolute values of static transport properties are strongly related to the chosen amount of the HFE and only values obtained using the same amount can be compared. We also showed, that it is possible to find a certain amount of the HFE included in the functional, to recover quasi-particle band structure obtained from highly accurate G_0W_0 approach. Although at first sight this seems useless, since the scaling of G_0W_0 is $n^4 \log n$ and the scaling of a hybrid functional is just n^4, in Chapter 7 we found that intensity-wise, calculated Raman spectrum is significantly improved when using functional that closely matches G_0W_0 results for quasi-particle band structure.

In Chapter 7, we also investigated the impact of HFE in the description of dynamic (electron-phonon couplings) transport properties of organic semiconductors. Similarly to

static properties, we found that nonlocal electron-phonon couplings increase with the increasing of the amount of HFE, as does the lattice relaxation energy (L). However, the ratio t/L was found to be independent on the amount of the HFE. This ratio can be used to compare strength of nonlocal coupling between different density and it is also a good candidate for incorporation into tight-binding transport models. In this Chapter, we also provided a microscopic understanding of a phase transition in charge-carrier mobility from temperature independent to thermally activated in stilbene-tetrafluoro-tetracyanoquinodimethane crystal. The transition is associated with two lattice vibrations for which electronic coupling showed nonlinear increase. These findings provide important insight into the effects that lattice vibration in molecular solids have on charge transport.

8.2 Further considerations

The results presented in this dissertation have pushed the understanding of the importance of static and dynamic electronic and transport properties toward a comprehensive understanding of charge generation and charge transport in organic single-component and bimolecular charge-transfer crystals. Below we list several aspects that could be worthy investigating in order to get a better understanding of the electronic properties in these systems.

In Chapter 6 we showed that values of the *static* transport properties of periodic systems may vary significantly depending on the amount of the HFE included in the density functional, and thus, we benchmarked DFT values against G_0W_0 results. It would be of

interest to extend this study in several ways. First, to evaluate static transport properties (electronic couplings) of isolated molecules using G_0W_0, since the nature of the molecular orbitals and thus, values of the electronic couplings could change drastically taking into account many-body effects. Second, is to evaluate quasi-particle energies from a self-consistent GW calculation. In this case, there is no dependence on the initial wavefunction for the resulting quasi-particle energies. Third, similarly to the ground-state properties, excited-state energies (both singlet and triplets) are strongly affected by the amount of the HFE included in the functional, thus it is of interest to evaluate excited-state energies (both singlet and triplet) using highly accurate Bethe-Salpeter equations. This would allow a robust evaluation of the energies and wavefunctions even in cases where one-electron picture might fail (*i.e.*, diradical character in extended acenes).

In terms of the *dynamic* transport properties (electron-phonon coupling), an important issue is to simulate resonance Raman of organic single-crystals. This would allow depicting lattice vibrations that couple to excitons. Also, in conjunction with Bethe-Salpeter equations, this would allow monitoring conical intersections between singlet and triplet states. Understanding and describing these two phenomena are particularly important for singlet-fission photovoltaics.

Another direction of interest, in terms of dynamic properties, is related to gathering a throughout understanding of the importance of phonons beyond Γ-point for charge transport. It was recently shown that these phonons can play an important role in modulation of electronic couplings. Thus it is important to evaluate polaron binding

energies and lattice relaxation energies of organic semiconductors for the phonons beyond Γ-point at a reasonable level of theory, given the conclusions of this work. It is also important to find spectroscopic and electric techniques that would allow validation of the computational results.

APPENDIX A

LIST OF PUBLICATIONS

[1]   Bakulin, A. A.; Lovrinčić, R.; Xi, Y.; Selig, O.; Bakker, H. J.; Rezus, Y. L. A.; Nayak, P. K.; Fonari, A.; Coropceanu, V.; Bredas, J.-L.; Cahen, D. *Nature Communications (DOI: 10.1038/ncomms8880)* **2015**.

[2]   Stevens, L. A.; Goetz, K. P.; Fonari, A.; Shu, Y.; Williamson, R. M.; Brédas, J.-L.; Coropceanu, V.; Jurchescu, O. D.; Collis, G. E. *Chemistry of Materials* **2015**, *27*, 112.

 [3]   Zhu, L.; Yi, Y.; Fonari, A.; Corbin, N. S.; Coropceanu, V.; Brédas, J.-L. *Journal of Physical Chemistry C* **2014**, *118*, 14150.

[4]   Zhang, L.; Fonari, A.; Liu, Y.; Hoyt, A.-L. M.; Lee, H.; Granger, D.; Parkin, S.; Russell, T. P.; Anthony, J. E.; Brédas, J.-L.; Coropceanu, V.; Briseno, A. L. *Journal of the American Chemical Society* **2014**, *136*, 9248.

[5]   Goetz, K. P.; Fonari, A.; Vermeulen, D.; Hu, P.; Jiang, H.; Diemer, P. J.; Ward, J. W.; Payne, M. E.; Day, C. S.; Kloc, C.; Coropceanu, V.; McNeil, L. E.; Jurchescu, O. D. *Nature Communications* **2014**, *5*, 5642.

[6]   Fonari, A.; Sutton, C.; Brédas, J.-L.; Coropceanu, V. *Physical Review B* **2014**, *90*, 165205.

[7]   Zhang, L.; Fonari, A.; Zhang, Y.; Zhao, G.; Coropceanu, V.; Hu, W.; Parkin, S.; Brédas, J.-L.; Briseno, A. L. *Chemistry – A European Journal* **2013**, *19*, 17907.